1992

A prototype instrumentation device for monitoring forces on transmission lines

Ifan
Iowa State University

A prototype instrumentation device for monitoring forces on transmission lines

by

Ifan

A Thesis Submitted to the
Graduate Faculty in Partial Fulfillment of the
Requirements for the Degree of
MASTER OF SCIENCE

Department: Civil and Construction Engineering
Major: Structural Engineering

Approved:

Signatures redacted for privacy.

Iowa State University
Ames, Iowa

1992

TABLE OF CONTENTS

LIST OF FIGURES

LIST OF TABLES

NOMENCLATURE

A	cross sectional area (in^2)
[A]	calibration matrix that relates applied loads {P} to {U}
$[A]^T$	transpose of matrix [A]
$[A]^{-1}$	inverse of matrix [A]
[A1], [A2], [A3]	the slope of the linear regression line
A_p	the projected area of the conductor on a plane normal to the wind direction (in^2)
a_o	galloping amplitude (ft)
B_w	dimensionless response term corresponding to the quasi-static background wind loading on the conductor
[B]	intercept matrix
[B1], [B2], [B3]	the intercept of the linear regression line C_c column slenderness ratio separating elastic and inelastic buckling
C_f	the force coefficient (= 1.0 for conductor)
d	the distance between strain gage no. 1 and no. 5 (in.)
E	modulus of elasticity (ksi)
F	axial force in the rod (lb)
F_{cr}	critical stress (ksi)
F_X	force in the X-axis direction (lb)

F_Y	force in the Y-axis direction (lb)
F_y	yield strength (ksi)
F_w	the wind force in the direction of wind (lb)
F_Z	force in the Y-axis direction (lb)
G	the gust response factor for conductors
H	horizontal component of static tension in the conductor (lb)
I	moment of inertia (in^4)
K	effective length factor
k_c	stiffness of conductor (lb/ft)
k_e	equivalent stiffness of the system (lb/ft)
k_i	stiffness of insulator in the longitudinal direction of the conductor (lb/ft)
L	span length (ft)
L_s	transverse integral scale of turbulance (ft)
l	the distance from the end of the insulator where the conductor is attached to the base of the cylinder (in)
M_X	moments in the Y-Z plane
M_Y	moments in the Y-Z planes
M_1, M_2	components of the bending moment
m	number of internal force readings
n	number of loops

{P}	matrix of applied loads
P_x	applied load in the X-axis direction
P_y	applied load in the Y-axis direction
P_z	applied load in the Z-axis direction
P1, P2, P3	the applied load
Q	the air density factor (= 0.00289)
R	resistance of the wire (ohm)
R_x	forces acting on a supporting structure in the longitudinal direction
R_y	forces acting on a supporting structure in the transverse direction
R_z	forces acting on a supporting structure in the vertical direction
R_1	resistance of the arms 1 of a Wheatstone bridge
R_2	resistance of the arms 1 of a Wheatstone bridge
R_3	resistance of the arms 1 of a Wheatstone bridge
R_4	resistance of the arms 1 of a Wheatstone bridge
ΔR	resistance change of the wire (ohm)
ΔR_1	resistance change of the arms 1 of a Wheatstone bridge

ΔR_2	resistance change of the arms 2 of a Wheatstone bridge
ΔR_3	resistance change of the arms 3 of a Wheatstone bridge
ΔR_4	resistance change of the arms 3 of a Wheatstone bridge
r	radius of gyration (in)
S	shear force (lb)
S_g	gage factor
S_x	the section modulus (in^3)
s_o	line static sag (ft)
T	unbalance voltage signal
ΔT	difference of unbalance voltage signal
t	time (sec)
U	exposure factor evaluated at the effective height of the conductor
{U}	matrix of internal force readings
{U1}, {U2}, {U3}	the internal forces readings
V	excitation voltage of Wheatstone bridge
V_c	vertical component of static tension in the conductor (lb)
V_{AB}	voltage between point A and B
V_{AD}	voltage between point A and D
v	vertical component of additional tension in the conductor (lb)

W	wind speed (mph)
w	conductor weight per unit length (lb/ft)
Z_o	effective height aboveground of the wire (ft)
Z_v	the terrain factor (= 1.048; for flat open land)
α	power-law coefficient for terrain factor equation
β	an angle between the misalignment and designated positions of strain gage
γ	the angle between the Y-Z plane and the plain where strain gages A and C are located
ϵ_A	strain at gage A (in./in.)
ϵ_B	strain at gage B (in./in.)
ϵ_{M1}	strain induced by M_1 (in./in.)
ϵ_{M1}	strain induced by M_2 (in./in.)
ϵ_p	axial strain (in./in.)
ϵ_T	strain induced by temperature change (in./in.)
ϵ_x	strain in the wire (in./in.)
ϵ_θ	strain in the inclined gage (in./in.)
θ	inclined angle of a misoriented strain gage
κ	surface drag coefficient

σ	stress (ksi)
υ	Poisson ratio
ω_n	eigenvalue

1. INTRODUCTION

1.1 Background and Purpose for The Research

Galloping is a self-excited, low-frequency, and high-amplitude vibration of a conductor. Besides ice and wind, there are other factors that affect galloping [1]. Electrical load being transmitted by a line may affect galloping, since a small temperature rise of a conductor can postpone the initiation of ice deposition, and a large enough temperature rise may prevent icing altogether. Torsional stiffness of the conductors also has an influence on galloping of the conductors. A low torsional-stiffness span, due to a large span length or a small conductor diameter, tends to experience large rotation at the midspan resulting in a shape of ice having aerodynamics characteristics suited for galloping.

Transmission line damage caused by galloping is not an unusual occurrence in some regions of the United States and Canada. The degree of damage can range from a broken insulator to the failure of tower structures that can cause the loss of power distribution for several months. In order to reduce the extent of transmission line damage, one can either attempt to prevent the occurrence of galloping of transmission line conductors or design the structures to withstand the forces due to galloping. Eliminating galloping, by using devices that interfere with the galloping mechanisms, has been studied for several years by the Central Electricity

Research Laboratories in the United Kingdom and by Ontario Hydro in Canada [1]. In order to design cost-efficient structures that are strong enough to resist typical galloping forces, one needs to know the magnitude of the forces involved. Very little research has been conducted in this area to date.

This study was devoted to designing an instrumentation device that would measure the forces acting on transmission line structures. Although the main purpose was to measure the forces induced by galloping, Chapter 3 will show that the concepts for the device developed in this work can be applied to measure other forces such as wind forces and the weight of ice. This study which involved the development of a prototype instrumentation device, was one phase of a larger research effort. Future research is planned to involve the monitoring of the behavior of transmission lines by mounting instrumentation devices on several supporting structures.

1.2 Scope of The Study

The following list gives the tasks which were conducted in the study reported herein:

1. Literature review,
2. Survey of damage and instrumentation of transmission lines,
3. Transducer design and development,

4. Experimental tests of the prototype instrumentation, and
5. Analytical studies of the results obtained from the experimental tests.

In the first task, the technical papers discussing instrumentation devices on the transmission lines were reviewed. The results of this study are summarized in the subsequent part of this chapter. A survey was conducted to review the most current research on the instrumentation devices and to study the severity of the galloping problem. This survey and its results are described in Chapter 2. In Chapter 3, the underlining principles, the design, and the development of the prototype device are discussed. Experimental testing of the instrumentation device involved calibrations and tests to determine the accuracy of the device. The calibrations and the tests were conducted with and without a post-type insulator attached to the device. The descriptions of the experimental tests and the discussions of the results can be found in Chapter 4. The conclusion about this research and the suggestions for future research are listed in Chapter 5.

1.3 Literature Review

1.3.1 Current research on galloping

There are two theories that have been proposed to explain the galloping phenomenon [2]. The first theory is the Den

Hartog theory [3] and the second theory is the torsional-excitation theory by Nigol and Clarke [4]. According to the Den Hartog theory, galloping is a vertical vibration and its occurrence is due to the aerodynamic instability of a non-circular cross section conductors. A non-circular cross section conductor results from the accumulation of ice on the conductors. Nigol and Clarke considered the coupling of the torsional and the vertical instability of the conductor as the cause of galloping. The eccentric torsional moment is the result of the deposition of the ice on the windward side of the conductor. This eccentric ice load also causes the aerodynamic instability of the conductor.

A recent galloping study that includes the forces induced on the supporting structure of transmission lines was conducted by Baenziger, James, Wouters and Li [5,6]. Their study was based on the following assumptions:

1. The effect of supporting structures on the dynamic response from conductor galloping is negligible,
2. Linear theory is still valid,
3. Amplitude of galloping remains constant,
4. Conductor motion starts from an initially assumed shape, and
5. Only vertical motion is considered.

The objective of their study was to obtain the solution for the forces induced by galloping. They began with the

dynamic equation of motion based on the cable theory by Irvine [7]. By applying the assumptions listed above, they derived expressions for the forces on the support structures. The vertical force as a function of time can be expressed as

$$(V_c+v)=\frac{1}{L}[4s_o + n\pi a_o\cos(\omega_n t)][\frac{2k_e a_o wL}{n\pi H}\cos(\omega_n t) + H] \quad (1-1)$$

where: V_c = vertical component of static tension in the conductor (lbs)

v = vertical component of additional tension in the conductor (lbs)

L = span length (ft)

s_o = line static sag (ft)

n = number of loops

a_o = galloping amplitude (ft)

ω_n = eigenvalue

t = time (sec)

k_e = equivalent stiffness of the system (lbs/ft)

$$k_e=\frac{1}{\frac{1}{k_c}+\frac{1}{k_i}} \quad (1-2)$$

k_c = stiffness of conductor (lbs/ft)

k_i = stiffness of insulator in the longitudinal direction of the conductor (lbs/ft)

w = conductor weight per unit length (lbs/ft)

H = horizontal component of static tension in the conductor (lbs)

According to Rawlins [8], k_1 is equal to 1500 lbs/ft for a rigid support. A post-type insulator would be of this type. The maximum vertical force is

$$(V_c+v)_{max}=\frac{1}{L}[4s_o + n\pi a_o)][\frac{2k_e a_o wL}{n\pi H} + H] \quad (1-3)$$

and the maximum horizontal component of additional tension of conductor is

$$h_{max}=\frac{2a_o k_e wL}{n\pi H} \quad (1-4)$$

The derivation of Eq. 1-3 was based on a single span conductor, therefore, the vertical force on a multi-span conductor is twice the vertical force computed by Eq. 1-3.

1.3.2 Current research on instrumentation devices

A minimum number of publications addressing the measurement of forces induced by galloping on the transmission lines have been found to date. The most comprehensive field observations have been done by Ontario Hydro Research Division [9,10]. Since 1975, they have observed the following parameters related to transmission lines with suspension insulators: wind loads, ice loads, dynamic loads due to galloping, insulator swing angles, wind speed and direction, and air temperature. Their instrumentation devices consisted of a calibrated U-spring and two displacement transducers.

The displacement transducers were mounted on the U-spring to measure the insulator swing angles in the vertical plane. The vertical, longitudinal and transverse components of conductor load can be calculated from the insulator string load and measured swing angles. Wind speed and direction were monitored with a propeller-type anemometer located at the top of the tower.

British Columbia Hydro has also conducted research [11,12] on the behavior of transmission lines with suspension insulators including measurements of forces caused by galloping, wind, and snow. Besides measuring forces in three orthogonal directions (vertical, transverse, and longitudinal) they also measured tower tilt, and snow pressure on the tower leg. They used triaxial load cells that were capable of measuring these forces. Their circular shaped transducer contains four spokes having a rectangular cross section. To detect shear strain, 45-deg strain gage rosettes were mounted in the thinnest part of the spokes.

Another study [13] on the behavior of galloping was done by Western Area Power Administration of Colorado in cooperation with Research and Laboratory Services Division. These researchers built a ground-based sensor for detecting motion of transmission line conductors in order to measure the amplitude and frequency of galloping. The sensor, installed on the ground under the line, consisted of a sensor plate,

demodulator, and motion processor. The principle of the devices is that a vibrating conductor will cause fluctuation of the electric field under the conductor. Therefore, the sensor can detect the conductor's motion by detecting the fluctuation of the electrical signal under the conductor.

The lack of published information on transmission line forces shows that more research is needed on measuring the forces induced by galloping, especially for the lines with post-type insulators. Several lines of this type in Iowa have been damaged by galloping. Therefore, the emphasis of the research reported herein was to develop a transducer that can be mounted on transmission lines with post-type insulators. Chapter 3 will show that the developed transducer can also be used on the lines with suspension-type insulators.

2. SURVEY ON TRANSMISSION LINE DAMAGE AND INSTRUMENTATION

2.1 The Survey

In 1991, a questionnaire on transmission line damage and instrumentation was sent to 58 utilities or companies located in different geographical areas representing various climatic conditions. The organizations are located in the states of California, Texas, Iowa, Wisconsin, Missuori, Michigan, Illinois, Nebraska, New York, Pensylvania, Florida, Oregon. Also, a questionnaire was sent to the power affiliates in Washington D.C. and in Ontario and Manitoba, Canada. The two-part questionnaire addressed mechanical damage and instrumentation of lines. The questionnaire requested information recorded between 1980 and 1991.

For the portion of the survey that addresed mechanical damage, the respondents were asked to indicate the causes and the frequency of occurance of damage to various structural and non-structural elements of transmission lines. The causes for damage were listed on the survey as wind, ice, galloping, thermal, and other. The frequency of occurance was classified as never, few, many, and often. For the portion of the questionnaire that addressed instrumentation of transmission lines, information regarding the measured parameters was requested. The parameters listed on the questionnaire were wind speed, temperature, ice thickness, ice-shape profile, forces on the line, amplitude and frequency of galloping

of galloping vibration, and other. The measurement of these parameters were to be indicated for line type, voltage level, structure type, insulator type, and span length. The complete questionnaire is included in Appendix A.

2.2 Results of The Survey

Out of the 58 questionnaires which were distributed, 31 respondents (53%) replied. The results of the survey are summarized in Tables 2.1 - 2.4. The numbers shown in these tables represent the number of respondents who checked the corresponding item of the table. Table 2.1 shows that the major causes of failure were wind, ice, and galloping.

The damage on the transmission lines were reported as ranging from a broken conductor connection to the failure of

Table 2.1. Causes of damage to transmission lines

Causes	Frequency		
	Few	Many	Often
Wind	5	5	8
Ice	6	4	4
Galloping	1	5	6
Thermal	5	3	1
Other	2	2	5

the supporting structure, as shown in Tables 2.2 and 2.3. Among the structural failures reported, damage to the support arm, to the wood and steel poles, and to H-frame structures were the most frequent. About ten percent of the respondents reported that galloping was the cause of the failure of wood poles and wood-H-frames. Three respondents reported that many wood poles have been damaged by galloping. Table 2.3 shows that the damage of conductors and their connections were the most frequent among the non-structural failures.

Table 2.2. Structural failures on transmission lines

Type or part of the structure	Frequency		
	Few	Many	Often
Support arm	19	12	6
Pole	20	12	10
H-Frame	22	10	1
Lattice structure	12	4	3
Multiple towers	7	2	0

As indicated on Table 2.4, only 5 respondents reported that they have instrumentation on transmission lines. For these respondents, only two have measured forces on the lines and only one of them has measured forces in three orthogonal directions. The response to the survey revealed that

Table 2.3. Non-structural failures on transmission lines

Part of the transmission line	Frequency		
	Few	Many	Often
Conductors & their connections	58	18	10
Post insulators	23	5	0
Suspension insulators	21	2	2
Insulator connections	18	3	0
Other	7	1	5

Table 2.4. Instrumentation on transmission lines

Parameters measured	Insulator type	
	Post	Suspension
Wind speed	1	5
Temperature	1	4
Ice thickness	1	3
Ice shape profile	1	2
Insulator swing angle	0	2
Vertical force	0	2
Longitudinal force	0	0
Lateral force	0	2
Galloping amplitude	1	2
Galloping frequency	1	2
Galloping duration	1	3
Aeolian vibration	1	3

transmission lines with suspension-type insulators have been monitored more often than lines with post-type insulators. The results of this survey and the lack of the published information on transmission line instrumentation indicates that more research addressing the forces acting on the transmission lines is needed.

3. THE PROTOTYPE TRANSDUCER

3.1 Forces to be Considered and Their Magnitudes

The type of forces, their anticipated maximum magnitudes, and their general direction should be established before designing a transducer. For transmission lines with post-type insulators, the insulators can be mounted horizontally, as shown in Figure 3.1a, or vertically, as shown in Figure 3.1b. Figure 3.1 also shows the generalized forces acting on a supporting structure with a post-type insulator, in which, R_x, R_y, and R_z represents forces in the longitudinal, transverse, and vertical directions, respectively. Galloping, self-weight of the conductor and ice weight are vertical forces, whereas wind is an example of a transverse force. The galloping forces considered were the forces induced by galloping on one or two adjacent spans of a transmission line. A longitudinal force is caused by the difference in the tension between two adjacent spans of a conductor. The prototype transducer must not break when the actual forces act on the monitored transmission line and must still provide sufficient sensitivity of the measured forces. The transducer was designed to be mounted on either a 350-ft-span transmission line with post insulators or a 500-ft-span transmission line with suspension insulators.

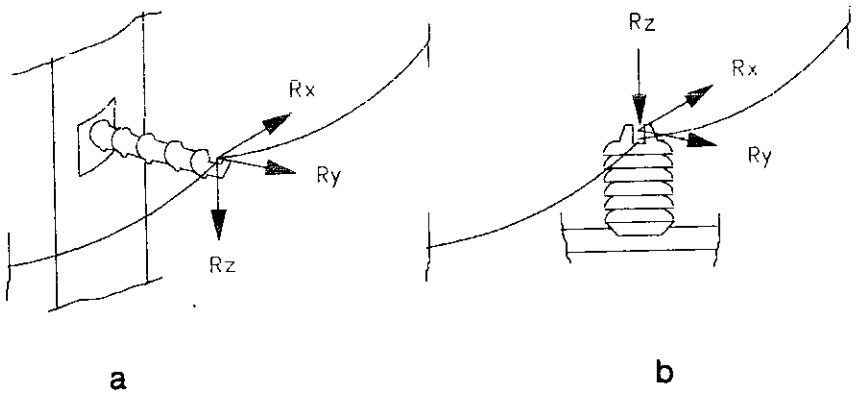

Figure 3.1. Forces and their directions on a pole with post-type insulator

The following assumptions were used to determine the magnitude of forces on a transmission line :

1. Two equal adjacent span lengths of 350 ft and 500 ft on each side of an insulator were selected.
2. The elevation of the insulators were the same for both ends of the span.
3. The type of conductor was a Grosbeak conductor with a diameter of 0.99 in. which weighs 0.875 lb/ft.
4. A 60 deg. F stringing temperature was selected.
5. The temperature for the analysis was 32 deg. F.
6. The forces induced by ice and the conductor tension were determined by a computer program (CABLE) developed by Baenziger [14].

7. The forces induced by galloping were determined by utilizing Eqs. 1-1 to 1-4 of Chapter 1.
8. The transverse forces cause by the wind were computed as static equivalent forces, in accordance with the Guidelines for Electrical Transmission Line Structural Loading [15], the speed of the wind in miles per hour can be converted to the forces by the following formulas:

$$F_w = Q(Z_v W)^2 G C_f A_p \tag{3-1}$$

$$G = 0.7 + 1.9 U \sqrt{B_w} \tag{3-2}$$

$$U = 4.9\sqrt{\kappa}\left(\frac{33}{Z_c}\right)^{1/\alpha} \tag{3-3}$$

$$B_w = \frac{1}{1 + 0.8L/L_s} \tag{3-4}$$

where: F_w = the wind force in the direction of wind (lb)

Q = the air density factor (= 0.00289)

Z_v = the terrain factor (= 1.048; for flat open land)

W = wind speed (mph)

G = the gust response factor for conductors

C_f = the force coefficient (= 1.0 for conductor)

A_p = the projected area of the conductor on a plane normal to the wind direction (ft^2)

U = exposure factor evaluated at the effective height of the conductor

B_w = dimensionless response term corresponding to the quasi-static background wind loading on the conductor

κ = surface drag coefficient

Z_o = effective height aboveground of the wire (ft)

α = power-law coefficient for terrain factor equation

L_s = transverse integral scale of turbulence (ft)

9. The initial tension used was 4000 lbs and 5000 lbs for the 350-ft-span transmission line and the 500-ft-span transmission line, respectively.
10. Two cases were studied; galloping on both adjacent spans and galloping on one span.
11. A radial ice thickness of 1 in. was selected.
12. A wind speed of 20 mph was considered.
13. The load factors were based on the National Electric Safety Code [16]. According to this code, the load factors for vertical, transverse, and longitudinal forces are 1.5, 2.5, and 1.65, respectively.

The forces resulting from the application of these assumptions are shown in Table 3.1. The forces Rx, Ry, and Rz are the forces in the longitudinal, transverse, and vertical direction, respectively. Galloping on a 350-ft span, galloping on two adjacent 350-ft spans, galloping on a 500-ft span, and galloping on two adjacent 500-ft spans are referred to as cases 1, 2, 3, and 4, respectively. For a sensitivity

Table 3.1. Forces on the supporting structure

Span(ft)	Galloping	R_x(lbs)	R_y(lbs)	R_z(lbs)	Case
350	one-span	1167	355	3012	1
350	two adjacent spans	0	355	4290	2
500	one-span	297	489	3737	3
500	two adjacent spans	0	489	4995	4

study, the forces induced by three loading conditions were considered; galloping on a line with 0.5 in. of radial ice thickness and a wind speed of 10 mph, the weight of 0.5 in. radial ice thickness, and a wind speed of 60 mph blowing across the bare conductor. The forces for the sensitivity study are shown in Tables 3.2 and 3.3 for a 350-ft-span and a 500-ft-span transmission line, respectively.

3.2 Preliminary Transducer Design

The first type of transducer studied was a hollow aluminum tube. Aluminum will last longer than steel in a severe weather environment where the transducer would be mounted. Also, aluminum will provide for a greater strain sensitivity than steel does, since aluminum has a modulus of elasticity about one-third that of steel. Therefore, for a given load magnitude, the strain in an aluminum transducer

part will be about three times that of a same size steel part.

A force in the axial direction can only be established from axial strains, whereas a transverse force in the direction perpendicular to the longitudinal axis of the

Table 3.2. Forces used in sensitivity study for 350-ft span

Causes	R_x(lbs)	R_y(lbs)	R_z(lbs)
Galloping	0	24	500
Wind	0	423	0
Ice	0	0	319

Table 3.3. Forces used in sensitivity study for 500-ft span

Causes	R_x(lbs)	R_y(lbs)	R_z(lbs)
Galloping	0	33	520
Wind	0	583	0
Ice	0	0	455

cylinder can be calculated from either shearing or bending strains. Since utilizing bending strains provides more sensitivity than utilizing shearing strains, bending strains should be selected to establish the forces perpendicular to the axis of the cylinder. Therefore, this cylindrical type

transducer would measure axial strains and bending strains, then, these strains will be calibrated to the target forces.

The design code used was the Design of Steel Transmission Pole Structures [17], a manual published by ASCE . According to this manual, the design approach is based an ultimate strength method in which the loads include the desired factors of safety. The yield strength of the material is used without any strength reduction factor. The following parameters were considered for the design of a cylindrical transducer:

1. The type of aluminum was 7075-T6 with a yield strength, F_y, equal to 70 ksi and a modulus of elasticity, E, equal to 10,400 ksi [18].
2. The length of insulator was equal to 13.5 in.
3. The height of the transducer was assumed to be equal to 5 in.
4. To obtain a strong attachment between the insulator and the cylinder, the diameter of the cylinder should not be substantially smaller than the diameter of the base of insulator, which is equal to 5 in. A cylindrical tube with a diameter of 4 in. was selected. The 4-in.-diameter aluminum cylinders available on the market are cylinders with a wall thickness of 0.25 in. or larger. Therefore, an aluminum cylindrical tube with a diameter of 4 in. and a wall thickness of 0.25 in. was selected.

The maximum stress under the specified load is given by

$$\sigma = \frac{R\ (l)}{S_x} + \frac{R_z}{A} \leq F_y \qquad (3\text{-}5)$$

where: R = the resultant force

l = the distance from the end of the insulator where the conductor is attached to the base of the cylinder (in.)

S_x = the section modulus of the cylinder ($in.^3$)

A = the cross-sectional area of the cylinder ($in.^2$)

The maximum combined stress computed by Eq. 3-5 for case 1 is

$$\sigma = \frac{1.220(13.5+5)}{2.60} + \frac{3.012}{2.95} = 9.7 ksi < F_y$$

The maximum combined stress computed by Eq. 3-5 for case 2 is

$$\sigma = \frac{0.355(13.5+5)}{2.60} + \frac{4.29}{2.95} = 4.0 ksi < F_y$$

The maximum combined stress computed by Eq. 3-5 for case 3 is

$$\sigma = \frac{0.572(13.5+5)}{2.60} + \frac{3.737}{2.95} = 5.4 ksi < F_y$$

The maximum combined stress computed by Eq. 3-5 for case 4 is

$$\sigma = \frac{0.489(13.5+5)}{2.60} + \frac{4.995}{2.95} = 5.2 ksi < F_y$$

A sensitivity study was conducted by using the loads determined in Section 3.1 that were summarized in Tables 3.2

and 3.3. The results of this study were summarized in Table 3.4.

The following conclusions were drawn from these results:

1. This transducer would be sensitive enough to measure force acting perpendicular to its axis.
2. The transducer would not be sensitive enough to measure forces in the axial direction, because strains induced by these forces are small.

Table 3.4. Strain for a sensitivity study of an aluminum cylindrical tube transducer

Case	Strain (μin./in.) for a:	
	350-ft span	500-ft span
Galloping	16	17
Wind	500	690
Ice	10	15

The lack of sensitivity is due to the large axial rigidity, EA, of the transducer. A possible solution to this sensitivity problem would involve using two cylindrical transducers. One could be mounted horizontally at one end of the conductor span and another transducer could be mounted vertically at the other end of the span. The horizontal transducer would be used to measure vertical forces , whereas

the vertical transducer would be used to measure the transverse and longitudinal forces. The main disadvantage of this measurement approach would involve the difficulty of analyzing the results obtained, since the vertical forces obtained would correspond to a different location than the transverse and longitudinal forces.

3.3 The Prototype Transducer

Applying the concepts of an instrumentation device for measuring impact loads on bridge piers that was presented in a paper by Bazergui, Eryuzlu, and Saucet [19], a prototype transducer that can be installed on transmission line structures was developed. As shown in Figure 3.2, the transducer consists of a 1 1/4-in.-thick by 12-in.-wide by 12-in.-long aluminum loading plate, a 1 1/4-in.-thick by 15-in.-wide by 15-in.-long aluminum base plate, and eight 1/2-in.-diameter by 9-in.-long aluminum rods. The diameter of the rods was selected to provide sufficient sensitivity of strain magnitudes and to maintain adequate strength. The loading plate is connected to the base plate with the eight rods. There are two rods in each horizontal direction, and four rods in the vertical direction. The horizontal rods are attached to aluminum blocks that are welded to the aluminum plates. On one face of these blocks, a washer and a nut were installed on the rods; on the other face, beside a washer and a nut, a

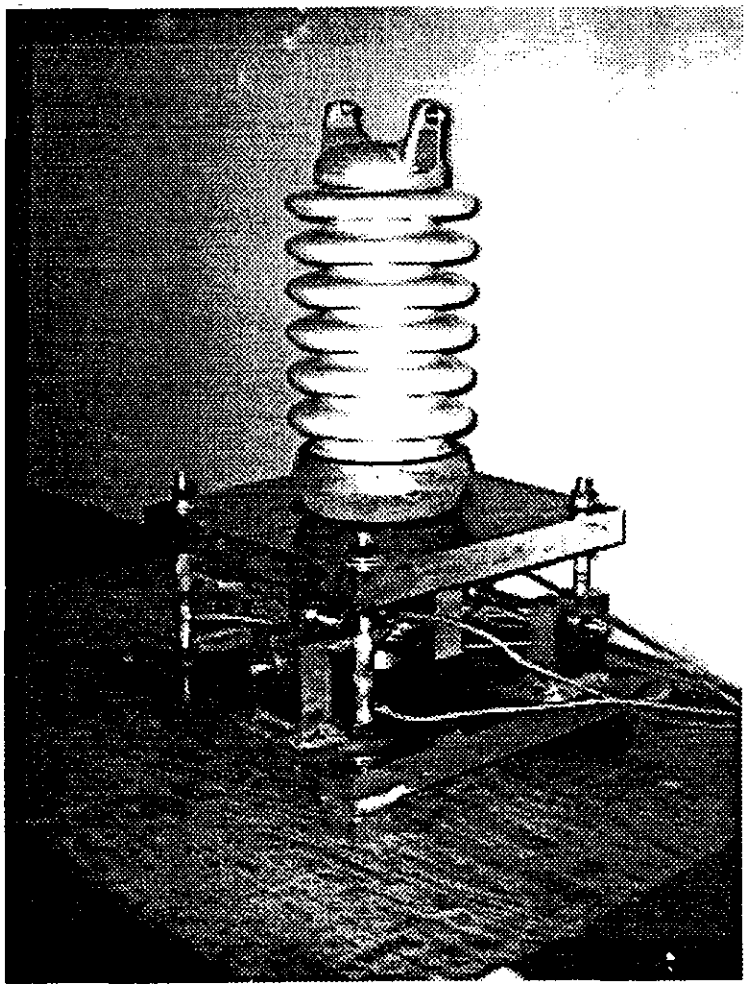

Figure 3.2. A picture of the transducer

locking washer was added. To obtain a consistent reading from the transducer, the connections for the rods were tighten using a calibrated torque wrench. The amount of torque used in tightening the nuts was 35 ft-lbs. The details of the transducer are shown in Appendix B. As shown in Figure 3.2, a post-type insulator would be attached to the top of the

loading plate, and the base plate would be connected to a pole with a bracket.

The transducer was initially designed to be mounted on transmission lines with post-type insulators. However, the transducer can be used on transmission lines with suspension-type insulators as well. For suspension insulator transmission lines, the transducer is to be mounted in the inverted position. The base plate should be connected to the cross arm of the transmission tower, and the insulator should be attached to the loading plate. The only difference in the transducer design would involve the size of the rods. The rod diameter would need to be increased due to larger loads associated with the longer span transmission lines.

3.4 Strain Gages and Wheatstone Bridge

Devices were needed to measure the axial forces and the shear forces on the rods. Electrical resistance strain gages were selected to be used in this research because strain gages are practical and economical. The principles [20] of electrical resistance strain gages are:

1. The resistance of the wire changes as a function of strain,
2. Different materials have different sensitivities,
3. The Wheatstone bridge can be used to measure these resistance changes accurately.

The relationship between the change of resistance of the wire and the strain on the wire is

$$\frac{\Delta R}{R} = S_g \varepsilon_x \qquad (3\text{-}6)$$

where: ΔR = resistance change of the wire (ohm)

R = resistance of the wire (ohm)

S_g = gage factor

ε_x = strain in the wire (in./in.)

The gage factor is a calibration constant and is provided by the manufacturer of the gage. If a strain gage is mounted properly on a specimen, then the strain in the wire must be the same as the strain on the specimen.

One can infer from Eq. 3-6 that in order to measure the strain on a specimen, the quantity $\Delta R/R$ must be measured and converted to strain. A Wheatstone bridge was used to convert the value of $\Delta R/R$ to a voltage signal ,ΔT, which was measured by a recording instrument (Hewlett-packard 3054A Data Acquisition System). In Figure 3.3; R_1, R_2, R_3, and R_4 are the resistance of the wire for each arm of the bridge; V is the excitation voltage; and T is the unbalance voltage which is the measurement target of this circuit. The voltage difference between point A and point B is given as

$$V_{AB} = \frac{R_1}{R_1 + R_2} V \qquad (3\text{-}7)$$

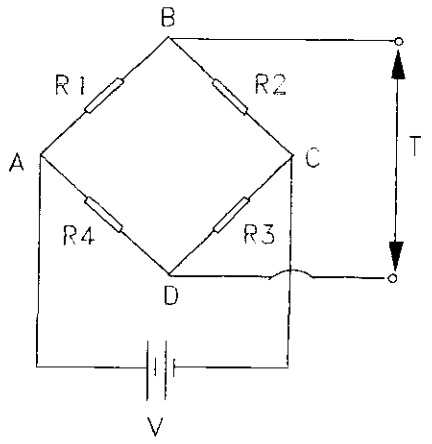

Figure 3.3. A Wheatstone bridge

Similarly, the voltage difference between point A and point D is

$$V_{AD} = \frac{R_4}{R_3+R_4} V \qquad (3\text{-}8)$$

The unbalance voltage is

$$T = V_{AB} - V_{AD} \qquad (3\text{-}9)$$

Substituting Eqs. 3-7 and 3-8 into Eq. 3-9 and simplifying gives

$$T = \frac{R_1R_3-R_2R_4}{(R_1+R_2)(R_3+R_4)} V \qquad (3\text{-}10)$$

The bridge is balanced, meaning T=0, when

$$R_1R_3 = R_2R_4 \tag{3-11}$$

Initially before the load is applied, the bridge is balanced and the voltage T is equal to zero. After the strain is applied, the resistance R_1, R_2, R_3, and R_4 are changed in the amounts of ΔR_1, ΔR_2, ΔR_3, and ΔR_4, respectively. The unbalance voltage ΔT of the bridge can be obtained from Eq. 3-12 as

$$\Delta T = V \frac{A}{B} \tag{3-12}$$

where A is the determinant in the numerator and B is determinant in the denominator, which are given by

$$A = \begin{vmatrix} R_1+\Delta R_1 & R_2+\Delta R_2 \\ R_4+\Delta R_4 & R_3+\Delta R_3 \end{vmatrix} \tag{3-13}$$

and

$$B = \begin{vmatrix} R_1+\Delta R_1+R_2+\Delta R_2 & 0 \\ 0 & R_3+\Delta R_3+R_4+\Delta R_4 \end{vmatrix} \tag{3-14}$$

Neglecting second-order term (ΔR^2), and recalling that $R_1R_3 = R_2R_4$ produces

$$A = R_1R_3\left(\frac{\Delta R_1}{R_1} - \frac{\Delta R_2}{R_2} + \frac{\Delta R_3}{R_3} - \frac{\Delta R_4}{R_4}\right) \tag{3-15}$$

and

$$B = \frac{R_1 R_3 (R_1+R_2)^2}{R_1 R_2} \tag{3-16}$$

Substituting Eq. 3-15 and 3-16 into Eq. 3-12, gives,

$$\Delta T = V \frac{R_1 R_2}{(R_1+R_2)^2}\left(\frac{\Delta R_1}{R_1} - \frac{\Delta R_2}{R_2} + \frac{\Delta R_3}{R_3} - \frac{\Delta R_4}{R_4}\right) \tag{3-17}$$

Eq. 3-17 is the basic equation which governs the behavior of the Wheatstone bridge in strain measurement. Eq. 3-17 implies that the Wheatstone bridge has 2 positive arms (arms 1 and 3) and 2 negative arms (arms 2 and 4).

The three most common Wheatstone bridge arrangements are shown in Figure 3.4: They are quarter-bridge, half-bridge, and full-bridge configurations. The half and the full-bridges provide for temperature compensation, and the full bridge is more sensitive than the other bridges [20]. Later on in this section, the temperature compensation and the sensitivity of a full-bridge configuration is discussed further.

In order to utilize strain gages for measuring the axial forces only, these strain gages should be arranged to measure the axial force independently of the bending moments, cross shears, and torsional moment. If the strain gages are put in the axial and circumferential directions of the rods, the strain gages reading are independent to the cross shears and torsional moment.

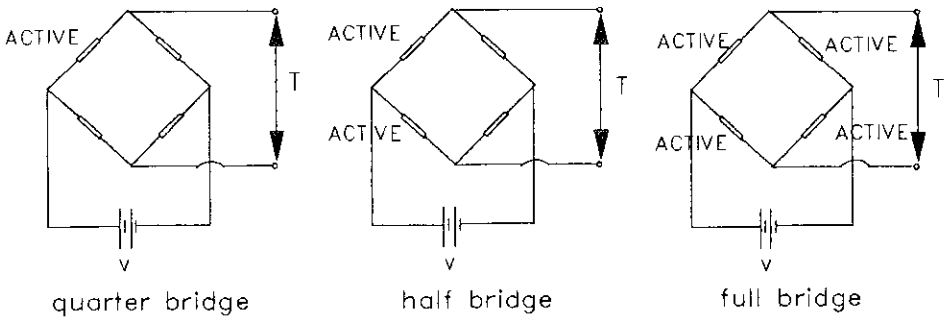

Figure 3.4. Wheatstone bridge configurations

A full-bridge circuit was used to make a strain gage circuit independent to the bending moments. To prove its independence toward bending moments, refer to Figure 3.5. The moment components M1 and M2 of bending moment M will produce resistance changes, consequently, strain changes, in the gages. These strains are listed in Table 3.5.

After accounting for appropriate sign, the total strain caused by M_1 is zero. The total strains caused by M_2 is zero also. Therefore, the total strain in the rods is the strain due to an axial force only, and this is proportional to $\Delta T/V$, which is expressed as

$$\frac{\Delta T}{V} = 2\epsilon_p(1+\nu) \qquad (3\text{-}18)$$

where: υ = Poisson ratio

So, the reading $\Delta T/V$ is more than twice the axial strain in the rod. Consequently, the sensitivity of the transducer is

increased. Another advantage of using a full-bridge is the temperature compensation effect. Referring to Table 3.5, the strain on the strain gages caused by temperature are the same for the four gages of the full-bridge, if all of the gages are the same type. Two strain gages are in positive arm and the

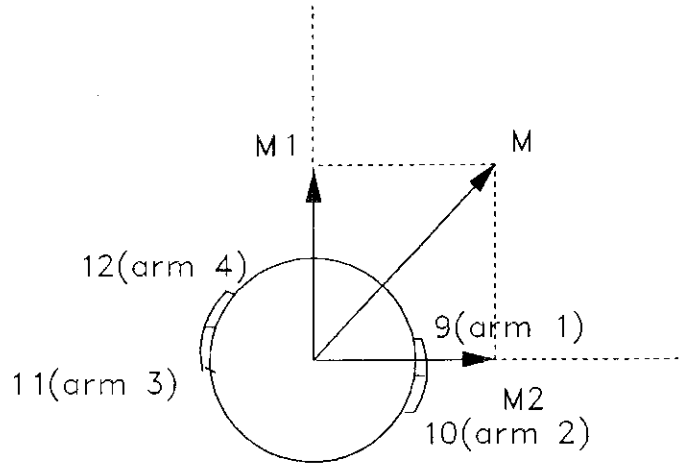

Figure 3.5. Components of a bending moment

other two are in negative arm. Thus, the total strains are zero.

A disadvantage of a full-bridge configuration relates to the difficulty in mounting the strain gages. Referring to Figure 3.5, strain gage nos. 9, and 10 should be mounted

Table 3.5. Strains in the rods

gage no.	sign	gage direction	strain caused by:			
			P	M_1	M_2	Temperature
9	+	axial	ϵ_p	$-\epsilon_{M1}$	0	ϵ_T
10	-	transverse	$-\upsilon\epsilon_p$	$\upsilon\epsilon_{M1}$	$\upsilon\epsilon_{M2}$	ϵ_T
11	+	axial	ϵ_p	ϵ_{M1}	0	ϵ_T
12	-	transverse	$-\upsilon\epsilon_p$	$-\upsilon\epsilon_{M1}$	$-\upsilon\epsilon_{M2}$	ϵ_T

opposite to strain gage nos. 11 and 12, respectively. If these strain gages are not exactly in the correct positions, the error induced will be small, because the bending moment in the middle of the rods where the strain gages are mounted would be very small (theoretically, equal to zero for a fixed-end rod having a relative displacement of its ends).

According to Eq. 3-18 $\Delta T/V$ is proportional to the axial strain, which is proportional to the axial force, so, $\Delta T/V$ is proportional to the axial force. Another point can be inferred from Eq. 3-18: Calibration of the electrical signal $\Delta T/V$ to axial force can be done by a simple tension test. This calibration procedure will be discussed further in Section 4.2.

The shear forces on the rods are measured indirectly by calculating the slope of the bending moment. Two strain gages are needed to obtain the bending moment diagram which is linearly distributed along the rod. To provide for some redundancies of strain gages, four gages at each end of the rod were used. Since there are two orthogonal cross-shears in a rod, eight strain gages were provided to monitor these shear forces. The location of these strain gages on a rod is shown on Figure 3.6. The strain gage nos. 1-8 were connected to quarter-bridge configuration circuits. In order to utilize the two orthogonal shear forces in each rod to monitor the applied loads on the transducer, these strain gages should be located in the planes parallel to the orthogonal planes of the applied loads. The strain gage nos. 1, 2, 3, and 4 should be located in the same cross-sectional plane and positioned 90 deg. apart from each other. The strain gage nos. 5, 6, 7, and 8 should be located in similar fashion. Strain gage nos. 1, 2, 3, 4 should be in line with strain gage nos. 5, 8, 7, and 6, respectively.

3.5 Transducer Design

The code used in designing the transducer was the Design of Steel Transmission Pole Structures [17]. The primary objective of this design stage was to determine the diameter and type of the rods. High strength aluminum, 7075-T6 (F_y=66

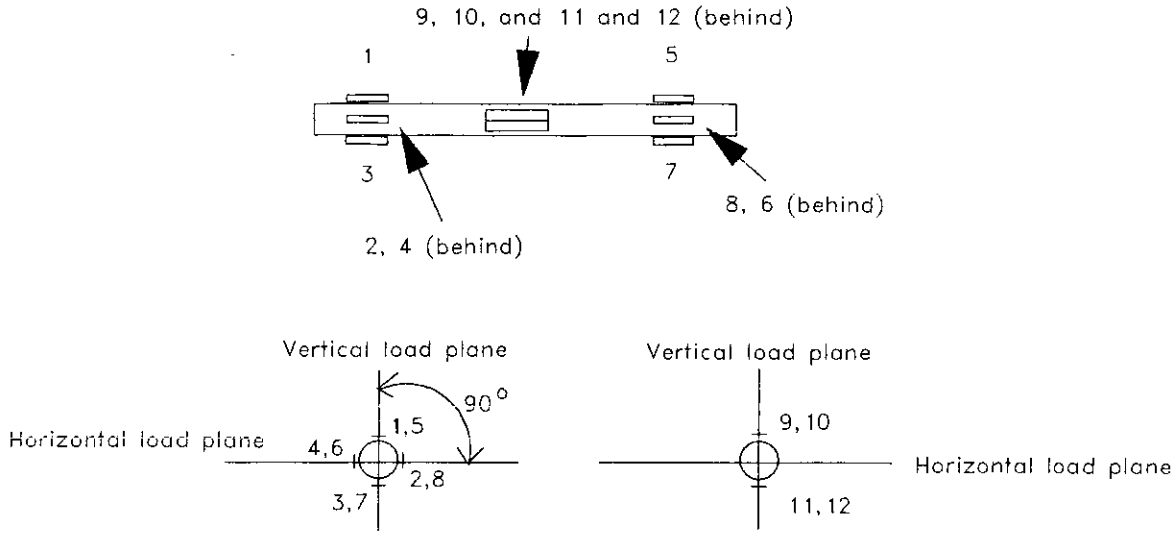

Figure 3.6. Location of strain gages

ksi), was used because the diameter needed for high strength aluminum rods would be smaller than the diameter needed for low strength aluminum rods for a given loading condition. Therefore, under the same applied loads the strain on the high strength aluminum rods would be larger than the strain on low strength aluminum rods. For consistency, the same diameter rods were used for both vertical and horizontal rods.

Figure 3.7 shows the horizontal load, R_x, and the vertical load, R_z, apply on the insulator. Rod nos. 1 and 2 are vertical rods and rod no. 5 is an horizontal rod. The forces to be resisted by the vertical rods are the forces induced by the horizontal load, R_x, with an eccentricity of 15.75 in., and the vertical load, R_z. Components of the axial

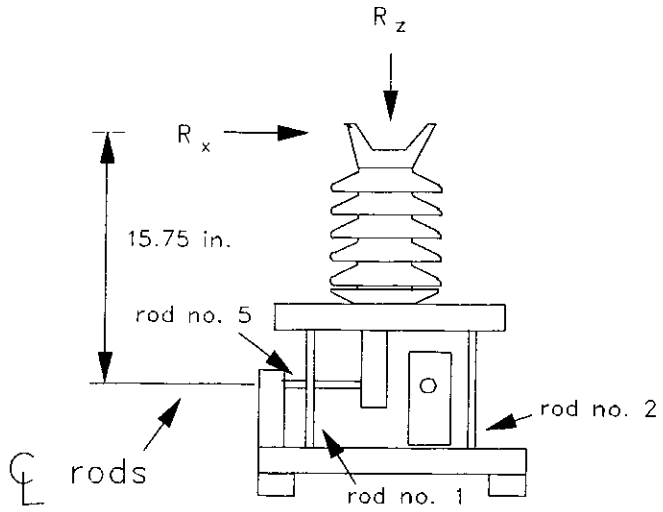

Figure 3.7. The loads apply on the transducer

forces in the vertical rods form a couple to resist the bending moment induced by the eccentric horizontal load. Theoretically, the vertical load is equally distributed to the four vertical rods. The axial forces in the vertical rods are equal to the summation of the axial forces caused by the eccentric horizontal load and the axial forces caused by vertical loads. The forces to be resisted by horizontal rod nos. 5 and 6 (not shown in Figure 3.4) are the forces induced by the horizontal load, R_x.

Table 3.6 and Table 3.7 show the maximum compressive forces induced on a vertical rod and a horizontal rod, respectively, by vertical, transverse, and longitudinal loads given in Table 3.1. Since the forces to be resisted by the horizontal rods are smaller than the forces to be resisted by the vertical rods, the vertical rod design governs.

Table 3.6. Axial forces in the vertical rods

Case	Axial forces induced by:			Maximum forces (lbs)
	R_x(lbs)	R_y(lbs)	R_z(lbs)	
1	919	280	753	1952
2	0	280	1073	1353
3	234	385	934	1553
4	0	385	1249	1634

Since the loads determined in Section 3.1 were based on theoretical calculations, a conservative approach was used in designing the transducer. For a compression axial forces a buckling criteria was applied. The critical stress is given by

$$F_{cr} = F_y\left[1-0.5\left(\frac{\frac{KL}{r}}{C_c}\right)^2\right] = 66\left[1-0.5\left(\frac{16.0}{55.8}\right)^2\right] = 63.3\ ksi \qquad (3\text{-}19)$$

where, the radius of gyration is

$$r = \sqrt{\frac{I}{A}} = \sqrt{\frac{3.1x10^{-2}}{0.196}} = 0.125\ in. \qquad (3\text{-}20)$$

the slenderness ratio is

$$\frac{KL}{r} = \frac{0.5(4)}{0.125} = 16.0 \qquad (3\text{-}21)$$

Table 3.7. Axial forces in the horizontal rods

Case	Axial forces in horizontal-X rod induced by:			Axial forces in horizontal-Y rod induced by:		
	R_x(lbs)	R_y(lbs)	R_z(lbs)	R_x(lbs)	R_y(lbs)	R_z(lbs)
1	584	0	0	0	178	0
2	0	0	0	0	178	0
3	149	0	0	0	245	0
4	0	0	0	0	245	0

and the column slenderness ratio separating elastic and inelastic buckling, C_c , is

$$C_c = \pi\sqrt{\frac{2E}{F_y}} = 3.14\sqrt{\frac{2(10.4x10^3)}{66}} = 55.8 > \frac{KL}{r} \qquad (3\text{-}22)$$

The stress in the vertical rod under load case 1 is

$$\sigma = \frac{1.952}{0.196} = 10.0\ ksi < F_{cr}$$

the stress in the vertical rod under load case 2 is

$$\sigma = \frac{1.353}{0.196} = 6.9\ ksi \ < F_{cr}$$

the stress in the vertical rod under load case 3 is

$$\sigma = \frac{1.553}{0.196} = 7.9\ ksi \ < F_{cr}$$

the stress in the vertical rod under load case 4 is

$$\sigma = \frac{1.634}{0.196} = 8.3\ ksi \ < F_{cr}$$

Tables 3.8 and 3.9 show the magnitude of the axial rod forces considered in a sensitivity study, for a 350-ft-span and 500-ft-span transmission line, respectively. These forces were obtained by the same procedures applied for the determination of the forces to be resisted by the vertical rods. However, the applied loads used were the load obtained in Section 3.1 that were summarized in Tables 3.2 and 3.3.

Table 3.8. Forces for sensitivity study of a 350-ft span

Case	Rod no.	Rod position	Axial forces (lbs)
Galloping	1	vertical	125
Wind	5	horizontal	212
Ice	1	vertical	80

Table 3.9. Forces for sensitivity study of a 500-ft span

Case	Rod no.	Rod position	Axial forces (lbs)
Galloping	1	vertical	130
Wind	5	horizontal	292
Ice	1	vertical	114

Table 3.10. Sensitivity study

Case	Strain (μin./in.) on	
	350-ft-span	500-ft-span
Galloping	61	64
Wind	104	143
Ice	39	56

The strain in a vertical and a horizontal rod induced by galloping, wind, and ice, respectively, are listed in Table 3.10.

The Hewlett-Packard 3054A data acquisition system that was used to monitor strains has an accuracy of 0.5 and 3 μin./in. for a full-bridge configuration and a quarter-bridge configuration, respectively, with an excitation voltage of 5 V. Therefore, the results of the sensitivity study showed that the transducer provided adequate sensitivity.

3.6 Finite-Element Analysis of The Transducer

A finite-element analysis was performed to model the behavior of the transducer under loads. ANSYS [21] was used to perform this analysis. The rods were modelled as three-dimensional elastic beam elements. The ANSYS code for this element is stif 4. Two models were used for the loading and base plates. The first model involved three-dimensional isoparametric solid elements (stif 45), and the second model involved quadrilateral shell elements (stif 43). Only the bending stiffness of the quadrilateral shell element was considered.

The three-dimensional beam element has six degrees of freedom per node: Translation in the X, Y, and Z-directions and rotation about X, Y, and Z-axes. The member X-axis is the axis oriented along the length of the member. The quadrilateral shell element has four nodes per element and six degree of freedom per node: Three translational degrees of freedom and three rotational degrees of freedom. The three-dimensional isoparametric solid element has three translational degrees of freedom per node. There was a special consideration for connection between isoparametric solid elements and beam elements, because the beam element has rotational degree of freedoms, whereas the solid element does not. The connection was accomplished by extending the beam

element into the solid element as suggested by S. Ridlon [22] and as shown in Figure 3.8.

The quadrilateral shell element model of the transducer is shown in Figure 3.9. Figures 3.9.a, 3.9.b, 3.9.c, and 3.9.d, show the close look to the transducer, side view, isometric view, and top view, respectively. The solid elements model is shown in Figs. 3.10. Figures 3.10.a, 3.10.b, 3.10.c, and 3.10.d, show the close look to the transducer, side view, isometric view, and top view, respectively. The boundary conditions at the points, where

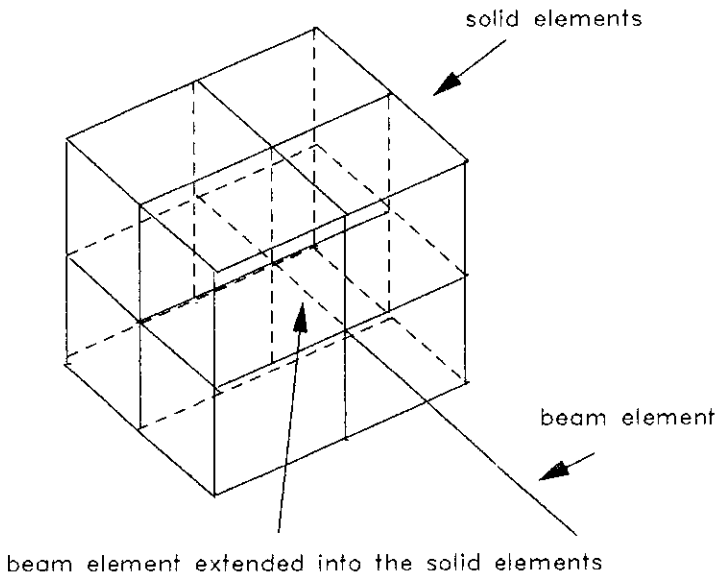

Figure 3.8. The extension of the beam element into the solid element

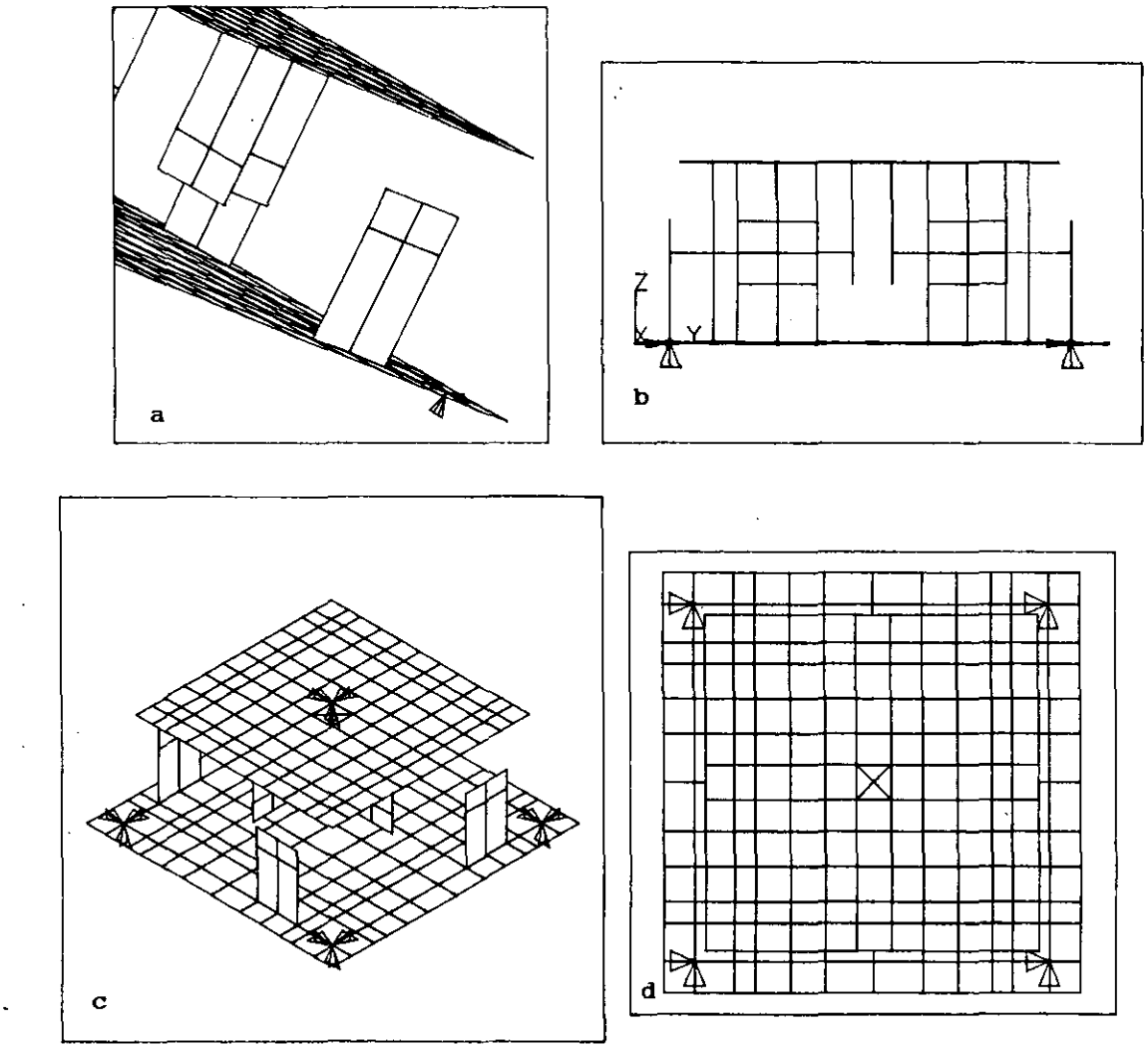

Figure 3.9. Quadrilateral shell element model

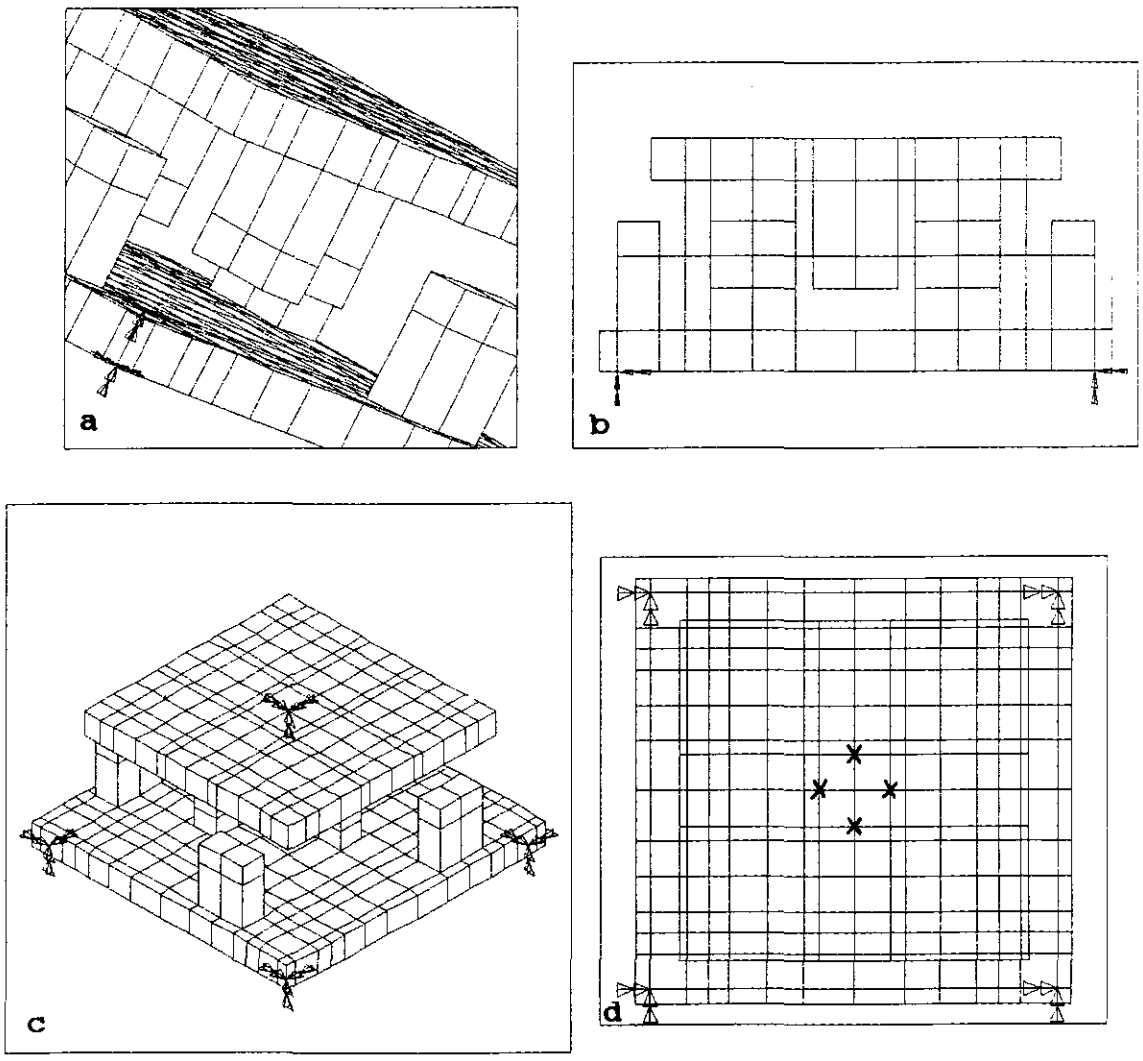

Figure 3.10. Solid element model

the base plate of the transducer is connected to the pole, are treated as translational fixed (translational displacements at this points are zero).

The applied loads used were a 1.04 kips vertical force, a 0.49 kip force in the longitudinal and transverse directions, and moments due to the eccentricity of the horizontal forces with respect to the loading plate. These forces were point forces acting on the center of the loading plate. For a three-dimensional element model, these moments were resolved into couples acting on nodes adjacent to the center of the loading plate (nodes with a label x on Figure 3.10).

The results of these analysis are tabulated in the Tables 3.11 and 3.12 for the quadrilateral shell element model and the three-dimensional solid element model, respectively. Shown in these tables are the axial forces in the rods and the difference between the summation of axial forces and the applied loads expressed as a percentage of the applied loads for the various types of loads and load combinations. The four forces listed in the F_z column are the axial forces in the vertical rods (Rod nos. 1-4) and the two forces listed in the F_x and F_y columns are the axial forces in the horizontal rods that are parallel to the X and Y-axes, respectively (Rod nos. 5 and 6; and nos. 7 and 8, respectively) for each applied loading condition. The dash symbol in the tables means that

Table 3.11. Results of the finite-element analysis with quadrilateral shell elements

Applied load	Forces in the rods (kips)			% difference		
	F_z	F_x	F_y	F_z	F_x	F_y
P_x =0.49 kips	0.0529 -0.0549 0.0549 -0.0529	-0.2406 -0.2406	-0.0005 -0.0005	-	1.8	-
Total	0	-0.4812	-0.0010			
P_z =1.04 kips	0.2564 0.2564 0.2564 0.2564	-0.0044 0.0044	-0.0044 0.0044	1.4	-	-
Total	1.0255	0	0			
M_y =6.62 in.-k	-0.1394 0.1394 0.1394 -0.1394	-0.0003 0.0003	-0.0006 0.0006	-	-	-
Total	0	0	0			
P_x =0.49 kips P_y =0.49 kips P_z =1.04 kips M_x =6.62 in.-k M_y =6.62 in.-k	-0.1302 0.2544 0.6430 0.2504	-0.2452 -0.2335	-0.2436 -0.2348	1.4	2.3	2.4
Total	1.0256	-0.4787	-0.4572			

the percentage difference calculation is not applicable for that particular load. The loads considered were the loads in the horizontal direction, P_x; in the vertical direction, P_z; moment, M_y, in the vertical X-Z plane; and a combination of these loads and a moment, M_x, in the vertical Y-Z plane. The

Table 3.12. Results of the finite-element analysis with three-dimensional solid elements

Applied load	Forces in the rods (kips)			% difference		
	F_z	F_x	F_y	F_z	F_x	F_y
P_x =0.49 kips	0.0681 -0.0701 0.0681 -0.0701	-0.2318 -0.2318	-0.0004 -0.0004	-	5.4	-
Total	0	-0.4635	-0.0008			
P_z =1.04 kips	0.2569 0.2569 0.2569 0.2569	-0.0076 0.0076	-0.0076 0.0076	1.2	-	-
Total	1.0274	0	0			
M_y= 6.62 in.-k	-0.1394 0.1394 0.1394 -0.1394	-0.0017 0.0017	-0.0011 0.0011	-	-	-
Total	0	0	0			
P_x =0.49 kips P_y =0.49 kips P_z =1.04 kips M_x =6.62 in.-k M_y =6.62 in.-k	-0.1601 0.2549 0.2589 0.6739	-0.2392 -0.2240	-0.2210 -0.2362	5.5	6.7	8.4
Total	1.0276	-0.4632	-0.4572			

results of the analyses showed that the shear forces induced by the applied loads were small. The quadrilateral shell element model produced better results, since the percentage difference between the summation of the axial forces in the rods and the applied loads were smaller than the differences for the solid element model in most of the load cases and load combination.

3.7 Natural Frequency of the Transducer

The natural frequency of the transducer was determined by a finite-element analysis. Again, ANSYS [21] was used to perform this analysis. The models of the transducer were the same as before. The lowest three natural frequencies are shown in Table 3.13 for both models. The first mode of

Table 3.13. Natural frequency of the transducer

Element type	Natural frequency (Hz)		
	1st Mode	2nd Mode	3rd Mode
3-D isoparametric solid	245	360	360
quadrilateral shell	213	312	312

vibration, which has the lowest natural frequency, corresponds to a torsional mode, whereas the second and third vibrational modes correspond to the translation mode in the X and Y-axis directions, respectively. The natural frequency of the second and the third mode are equal, because the transducer is symmetric.

According to Rocard [23], the frequency band in which the amplification due to dynamic force remains large extends from $\omega(1-\sqrt{3}\zeta)$ to $\omega(1+\sqrt{3}\zeta)$; where ω is natural frequency and

ζ is damping ratio. According to Adams [24], the damping ratio for aluminum material is 0.0165%. The frequency band for the transducer extends from 212.9 Hz to 213.1 Hz. The frequency of galloping (0.08-3 Hz) and of aeolian vibration (3-150 Hz) [1] are not in the frequency band; therefore a resonance will not occur.

3.8 Determination of Forces

Three approach in determining the magnitude of the forces, which were applied to the transducer, were investigated. These methods involved the summation of the internal forces, calibration of the transducer using the shear forces and axial forces, and calibration of the transducer using the axial forces only. The first approach was based on the static equilibrium of the transducer under loads; the applied loads are equal to the summation of the internal forces (axial forces and shear forces). When a load is applied on the transducer in a certain direction, this load will induce an axial force and two orthogonal shear forces in each rod. By statical equilibrium, the applied load is equal to the summation of the internal forces in the direction of the load and the summation of the internal forces in two mutually perpendicular directions are equal to zero. With this approach the applied loads are calculated by adding the internal rod forces.

The second approach was intended to handle any imperfect orientation and alignment of the strain gages. By calibrating the transducer, the error induced by any misalignment and misorientation of the strain gages would be minimized. The third approach is valid whenever the rod shear forces involved are small and was also considered due to its simplicity. Chapter 4 will show that even though the rod shear forces were neglected, the results obtained by this approach were basically the same as the results of the second approach. This effect is due to the small magnitude of the shear forces involved.

When the transducer was calibrated, a load was applied independently for each of the three orthogonal directions, and the relationships between the load and the strain gage readings were obtained. These relationships for an applied force in one direction, which were obtained from linear regression analyses, can be expressed as

$$\{U1\}_{mx1} = [A1]_{mx1} * P1 + [B1]_{mx1} \qquad (3\text{-}23)$$

where: {U1} = the internal force readings

[A1] = the slopes of the linear regression lines

P1 = the applied load

[B1] = the intercepts of the linear regression lines

m = number of internal force readings

The above procedure was repeated for the other two orthogonal directions, which produced the following two expressions:

$$\{U2\}_{mx1} = [A2]_{mx1} * P2 + [B2]_{mx1} \quad (3\text{-}24)$$

$$\{U3\}_{mx1} = [A3]_{mx1} * P3 + [B3]_{mx1} \quad (3\text{-}25)$$

If the loads P1, P2, and P3 were applied simultaneously, and providing that the transducer behaves elastically, the internal forces readings {U} could be obtained from Eq. 3-26

$$\{U\} = \{U1\} + \{U2\} + \{U3\} \quad (3\text{-}26)$$

Expanding Eq. 3-26

$$\{U\} = [A1]*P1+[B1] + [A2]*P2+[B2] + [A3]*P3+[B3] \quad (3\text{-}27)$$

By arranging [A1], [A2], and [A3] into one matrix [A]; P1, P2, and P3 into one matrix {P}; and [B1], [B2], and [B3] into one matrix [B]; and assuming that direction 1, 2, and 3 are the X, Y, and Z-directions, respectively, Eq. 3-28 was obtained

$$\{U\}_{mx1} = [A]_{mx3} * \{P\}_{3x1} + [B]_{3x1} \quad (3\text{-}28)$$

where: {U} = matrix of internal force readings

[A] = matrix that relates applied loads {P} to {U}

{P} = matrix of applied loads given by

$$\{P\} = \begin{Bmatrix} P_X \\ P_Y \\ P_Z \end{Bmatrix} \quad (3\text{-}29)$$

[B] = intercept matrix

In an actual application (field measurements), the matrix {U} would be obtained instead of matrix {P}. Therefore, a matrix that relates {U} to {P} would be needed. Subtracting the matrix [B] from both side of the Eq. 3-28 gives

$$\{U\} - [B] = [A] * \{P\} \tag{3-30}$$

If the matrix $[A]^{-1}$ is a generalized inverse of the matrix [A], Eq. 3-30 could be solved as

$$\{P\} = [A]^{-1} (\{U\}-[B]) \tag{3-31}$$

According to Graybill [25],

$$[A]^{-1} = [A^T A]^{-1} A^T \tag{3-32}$$

Summarizing, the calibration procedure was done by the following steps:

1. The first column of [A] was obtained by applying load in the X-direction only,
2. The second column of [A] was obtained by repeating step 1 for the Y-direction,
3. The last column of [A] was obtained by repeating step 1 for the Z-direction,
4. By knowing [A], $[A]^{-1}$ was solved by applying Eq. 3-32.
5. To obtain {P}, Eq. 3-31 was used.

Each rod has one axial force and two orthogonal shear forces. Since the transducer consists of 8 rods, the number of internal forces readings was 24. Therefore, for the calibration of the transducer involving the rod shear forces and axial forces, the value of m was equal to 24. For the

calibration of the transducer using only the rod axial forces, the value of m was equal to 8.

The axial forces were obtained from the full-bridge strain gages by the approach discussed in Section 3.4. The shear forces were obtained from the quarter-bridge readings. Figure 3.11 shows the strain gage nos. 1, 3, 5, and 7, a bending moment diagram, and a shear force diagram for a rod.

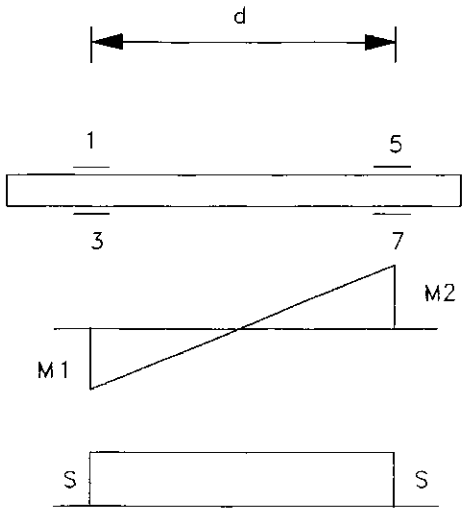

Figure 3.11. Establishing shear force from slope of the bending moment diagram

The bending moments M1 and M2 were established from the strains measured by gage nos.1 and 5, respectively. The shear force was established from the slope of the bending moment diagram. This relationship can be expressed as

$$S=\frac{M_2-M_1}{d} \tag{3-33}$$

where: S= shear force

M_1= bending moment at location of strain gage no. 1

M_2= bending moment at location of strain gage no. 5

d= the distance between strain gage no. 1 and no. 5

The relationship between the strains at gage no. 1 and gage no. 5; and the bending moments M_1 and M_2, respectively, are

$$\epsilon_1=\frac{M_1}{ES_x} \tag{3-34}$$

and

$$\epsilon_2=\frac{M_2}{ES_x} \tag{3-35}$$

where: ϵ_1= strain at gage no. 1

ϵ_2= strain at gage no. 5

By substituting Eqs. 3-34 and 3-35 into Eq. 3-33, the rod shear force is expressed by

$$S=\frac{ES_x}{d}(\epsilon_2-\epsilon_1) \tag{3-36}$$

Using this procedure, the shear force was established also from the strain readings obtained from gage nos. 3 and 7. The value of shear force used in matrix {U} was the average of these two values.

4. EXPERIMENTAL TESTS

4.1 Tension Test of the Aluminum Rod

A tension test was conducted to obtain the properties of the aluminum rods; modulus of elasticity, yield strength, and ultimate strength. The test was conducted on a Satec-400 HVL universal testing machine. The strain was measured by using an extensometer with a gage length of 2 in. Figure 4.1 shows the relationship between stress and strain up to the yield point of the material. The modulus of elasticity, yield strength, and ultimate strength of the sample aluminum rod, from which the rods for the transducer were cut, were 10,400 ksi, 77 ksi, and 87.7 ksi, respectively. The yield strength was determined as the stress at the 0.2% offset strain [26].

4.2 Calibration of The Rods

The strain gages which were arranged in a full-bridge configuration for each rod were calibrated by using a tension test. This calibration was done on a Satec-400 HVL universal testing machine. The strain gages, arranged in a full-bridge configuration, were connected to a power supply and a digital voltmeter. The power supply was used to give an excitation voltage V to the bridge and the digital voltmeter was used to measure the unbalanced voltage ΔT induced in the bridge. The unbalanced voltage readings ΔT were taken when the loads were equal to 100, 200, 300, 400, 500, 600, 700, 800, 900, 1000,

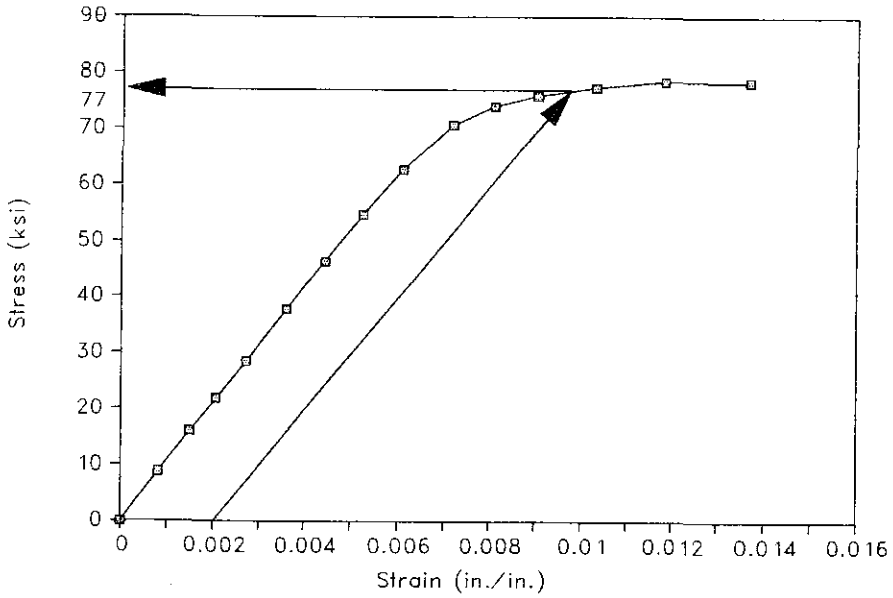

Figure 4.1. Stress-strain curve of the tension test of the aluminum rod

1200, 1600, and 2000 lbs. A linear regression analysis was conducted to obtain the relationship between ratio of the unbalanced voltage reading to the excitation voltage, $\Delta T/V$, and the applied loads, P. The results of this analysis for Rod no. 1 is shown in Figure 4.2. The results for seven other rods are given in Appendix C. The slopes of the linear regression lines ranged from 1471.93 to 1563.33 kip-volt/volt. The largest slope is 6.2% larger than smallest slope. These calibrations indicated that the full-bridge strain gages performed satisfactory and consistently. The axial forces in the rods were determined by utilizing these curves during the

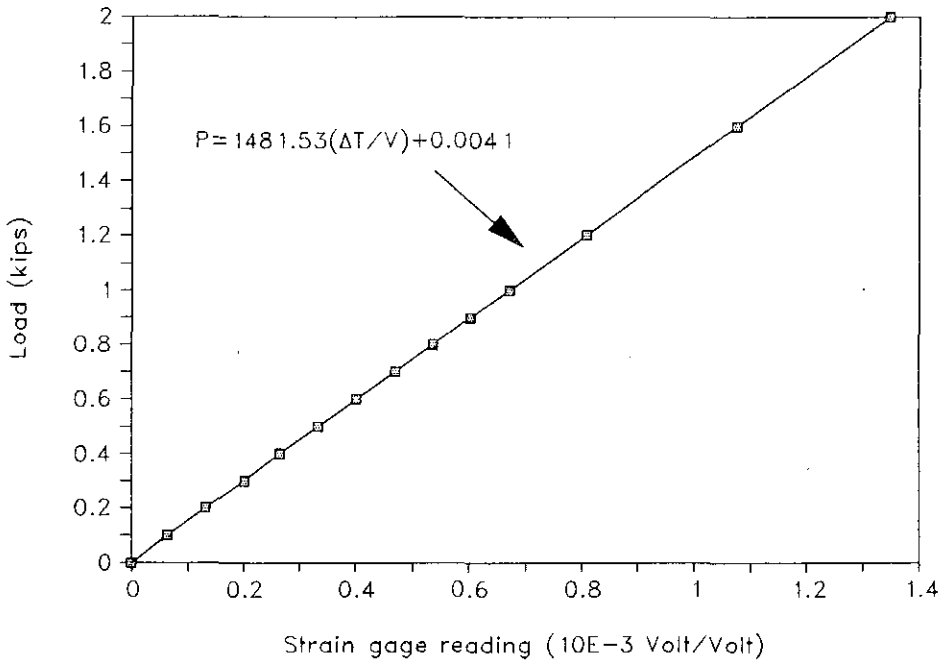

Figure 4.2. Regression line for rod no. 1

transducer calibration which is discussed in Section 4.4 of this chapter.

Since the strain gages that were arranged in a quarter-bridge configuration were bonded to the rods after the initial calibration was performed for the full-bridge gages, another tension test of each rod was conducted. The voltages monitored with the strain gages were converted to strain readings and axial forces by a software program that was written for the Data Acquisition System (DAS). By comparing the experimentally derived axial forces with the loads

applied, the performance of each strain gage was examined. The differences between the experimentally derived and applied axial forces were 5% or less. These results indicated that the quarter-bridge strain gages performed well.

As discussed in Chapter 3, the effect of bending moments on full-bridge strain gages should be eliminated by the nature of full-bridge circuit; therefore, the strain gages readings are proportional to the axial forces. The strain gages in the quarter-bridge configurations were used to calculate rod shear forces from the monitored flexural strains at two points along the length of a rod. Bending tests were conducted to prove that the full-bridge gages were not significantly affected by bending moments and to test the performance of the quarter-bridge gages in establishing the rod shear forces. In this test the strain gages were connected to the DAS. Figure 4.3 shows the arrangement of the test. In this test, one end of a rod was bolted to a column and weights were hung at the other end.

In the bending test to examine the performance of the full-bridge strain gages, the weights used were 1.6875, 3.6875, 6.6875, and 9.6875 lbs. The results of the tests showed that when a 9.6875 lb weight was hung at the free end of the rod, the largest full-bridge strain gage reading was 7 μ in./in., which is small compare to the theoretical strain equal to 342 μ in./in. In the bending test to examine the

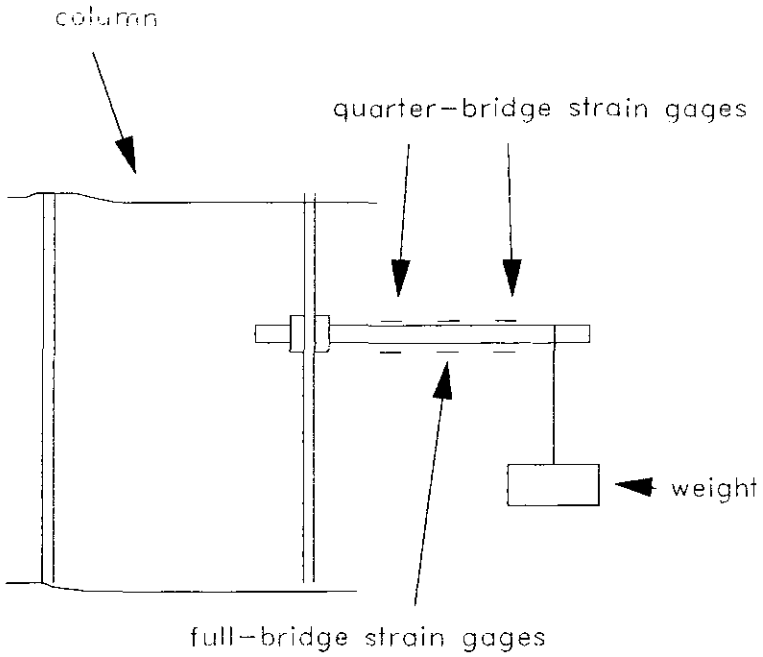

Figure 4.3. Bending test of a rod

performance of the quarter-bridge strain gages, the weights used were 5, 10, 15, 20.7, 26.4, and 32.1 lbs. The strains measured at the gages located in the bending plane were essentially the same (an error of only 6% or less) as the theoretically strains computed by beam theory. The largest strain measured at the gages located in the plane at the neutral axis and perpendicular to the bending plane was 139 μ in/in (theoretically this strain should be zero). Since the strain is proportional to the distance from neutral axis,

these results indicate the gages have an offset of 0.043 in. or less. These small offsets are not visible.

4.3 The Effects of the Inclined and the Offset Strain Gages

The orientation and alignment of the strain gages might not be perfect. Any small misorientation or misalignment of the strain gages that are not visible might happened when the strain gages were mounted on the rods and when the transducer was assembled. The strain gage could have an inclined angle from the designated position, as shown in Figure 4.4. Consider a strain gage that is misoriented with an inclined angle, θ, as shown in Figure 4.5. Utilizing the strain

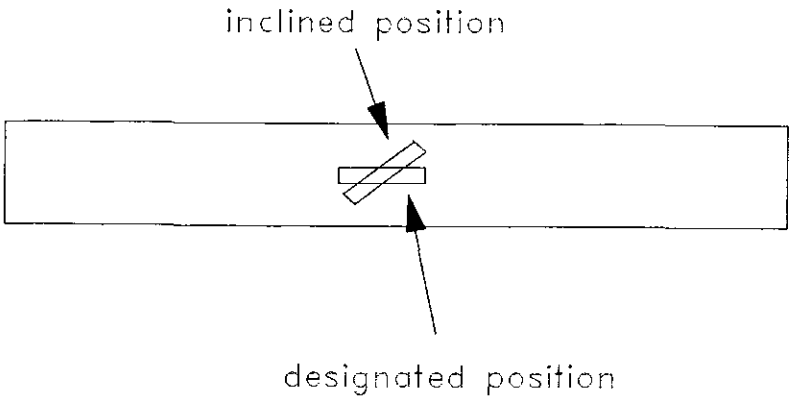

Figure 4.4. An inclined strain gage

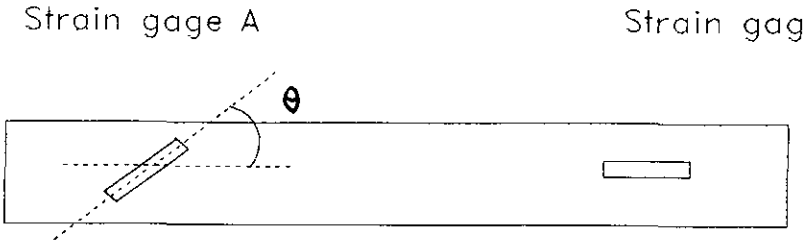

Figure 4.5. Strain gage A with an inclined angle, θ.

transformation equation [20], the strain at gage A can be expressed as

$$\epsilon_\theta = \epsilon_A \cos^2\theta - \nu\epsilon_A \sin^2\theta \qquad (4\text{-}1)$$

where: ϵ_θ= strain at inclined strain gage

ϵ_A= strain at designated position for strain gage A

The following expression is obtained by substituting Eq. 4-1 into Eq. 3-36 and replacing S with S′, ϵ_1 with ϵ_θ, and ϵ_2 with ϵ_B

$$S' = \frac{ES_x}{d}(\epsilon_B - \epsilon_A \cos^2\theta + \nu\epsilon_A \sin^2\theta) \qquad (4\text{-}2)$$

where S′= shear force resulted from imperfect orientation of strain gage A

The difference between S′ and S expressed as percentage of S is

$$\frac{S'-S}{S} x100\% = \frac{(\epsilon_B - \epsilon_A \cos^2\theta + \nu\epsilon_A \sin^2\theta) - (\epsilon_B - \epsilon_A)}{\epsilon_B - \epsilon_A} x100\% \qquad (4\text{-}3)$$

Assuming the value of ϵ_A and ϵ_B are equal but opposite in sign and substituting $-\epsilon_A$ for ϵ_B in Eq. 4-3 and simplifying, Eq. 4-4 is obtained

$$\frac{S'-S}{S} x100\% = -\frac{(1+\nu)\sin^2\theta}{2} x100\% \qquad (4-4)$$

The minus sign indicates that S' is smaller than S. If θ is equal to 5° or 10°, the percent error in the rod shear force is 0.5% or 2.0%, respectively. Therefore, any strain gage with an invisible inclination has a small effect on the calculated shear force.

A strain gage could have an imperfect alignment, as shown in Figure 4.6. The degree of misalignment of strain gage in Figure 4.6 can be measured by a radial angle, ß, which is defined as the angle between the misaligned and designated positions of strain gage as shown in Figure 4.7.

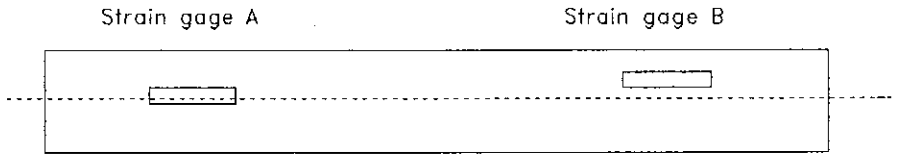

Figure 4.6. An imperfect alignment of two strain gages

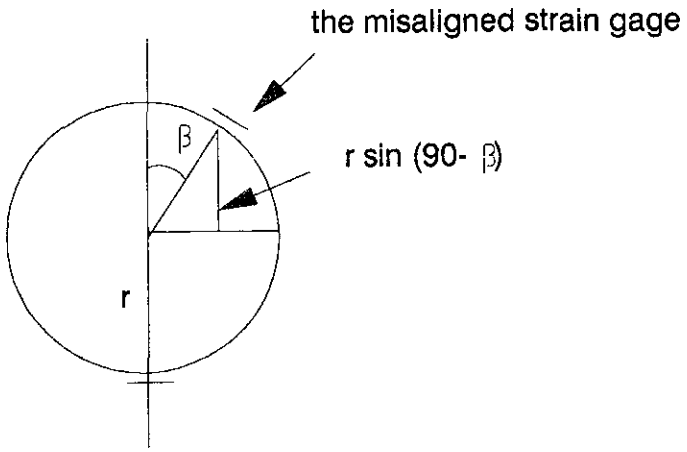

Figure 4.7. The angle ß

The strain at gage B can be expressed as

$$\epsilon_\beta = \frac{r\sin(90-\beta)}{r}\epsilon_B = \epsilon_B \sin(90-\beta) \qquad (4\text{-}5)$$

The following expression is obtained by substituting Eq. 4-5 into Eq. 3-36 an replacing S with S′, ϵ_1 with ϵ_A, and ϵ_2 with ϵ_B:

$$S' = \frac{ES_x}{d}(\epsilon_A - \epsilon_B \sin(90-\beta)) \qquad (4\text{-}6)$$

The difference between S′ and S expressed as percentage of S is

$$\frac{S'-S}{S}x100\% = \frac{(\epsilon_A - \epsilon_B \sin(90-\beta)) - (\epsilon_A - \epsilon_B)}{\epsilon_A - \epsilon_B}x100\% \qquad (4\text{-}7)$$

Substituting $-\epsilon_A$ for ϵ_B in Eq. 4-7 and simplifying produces

$$\frac{S'-S}{S}x100\% = \frac{\sin(90-\beta)-1}{2}x100\% \qquad (4-8)$$

If ß is equal to 5° or 10°, the percent error in the computed rod shear force is 0.19% or 0.76%, respectively. Therefore, any strain gage with a small misalignment has a small effect on the calculated shear force.

Another imperfect orientation that might happened is that the strain gages are not placed in the planes parallel to the orthogonal planes of the transducer. This could result from an imperfect orientation of the rod as shown in Figure 4.8. This figure shows that the strain gages A and C are not placed in the Y-Z plane and the strain gages B and D are not placed in the X-Z plane. If the angle between the Y-Z plane and the plane where strain gages A and C are located (see Figure 4.8) is γ, the shear force S′ (utilizing Eq. 3-36) can be expressed as

$$S' = \frac{ES_x}{d}\frac{r\sin(90-\gamma)}{r}(\epsilon_E-\epsilon_A) \qquad (4-9)$$

The difference between S′ and S expressed as percentage of S is given by

$$\frac{S'-S}{S}x100\% = \frac{(\epsilon_E-\epsilon_A)\sin(90-\gamma)-(\epsilon_E-\epsilon_A)}{\epsilon_E-\epsilon_A}x100\% \qquad (4-10)$$

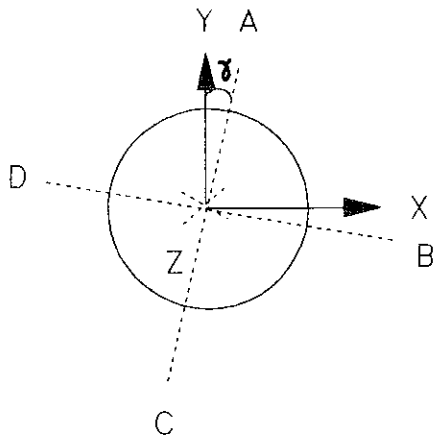

Figure 4.8. An imperfect orientation of a rod

Simplifying Eq. 4-10 produces

$$\frac{S'-S}{S} x100\% = \sin(90-\gamma) - 1 \qquad (4-11)$$

If γ is equal to 5° or 10°, the percent error in the computed rod shear force is 0.38% or 1.52%, respectively. Therefore, any rod with a small misorientation has a small effect on the calculated shear force.

4.4 Transducer Calibration

Since the transducer will be used in the field with an insulator mounted to the top plate of the transducer, the final calibration should involve forces applied to the top of the insulator. Horizontal loads would induce bending moments on the transducer. The existence of these bending moments

complicates the calibration procedure for the transducer; therefore, to study the behavior of the transducer, calibrations with and without an insulator present were performed.

Figure 4.9 shows the axes of the transducer that were used. For clarity, the horizontal rods are not shown in Figure 4.9.a. The X-axis is the axis parallel to Rod nos. 5 and 6, whereas the Y-axis is the axis parallel to Rod nos. 7 and 8. The Z-axis is the vertical direction axis. The downward direction of the vertical axis was defined as positive since most of the vertical loads act in a downward direction.

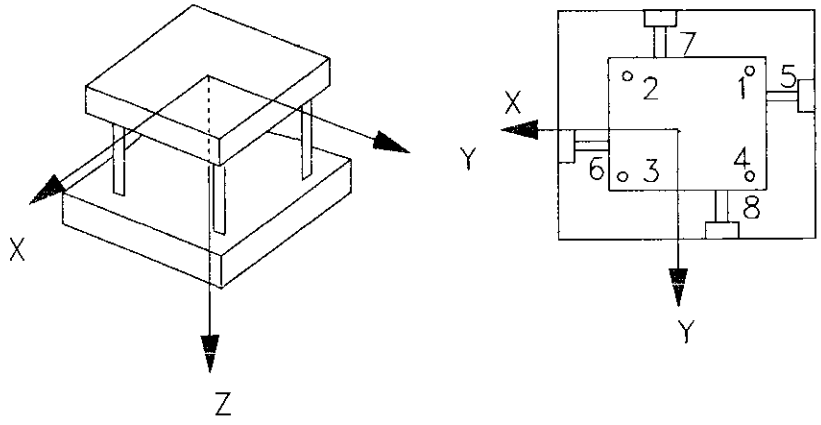

Figure 4.9. Definition of transducer axis

4.4.1 Horizontal direction without the insulator

The horizontal load calibration was conducted by pushing the load plate of the transducer with an actuator while the base plate was held in place. The arrangement of this test is shown on Figure 4.10. A load cell was placed behind the actuator in order to measure the applied load. The transducer was seated on a base which consisted of two 1/2-in.-thick plates connected by an 8-in.-diameter hollow tube, with a height of 7 5/8 in. With this arrangement, the transducer could be oriented in various positions with respect to the actuator, which permitted a horizontal load to be applied in various directions. There were 16 possible orientations available for the transducer, each with a 22.5° angle increment between them. This whole system was attached to a rigid support frame.

The calibration was conducted with the loads of 0, 200, 600, 1000, 1500, and 2500 lbs. After the readings were recorded at the maximum load, the load was decreased, and the readings were taken at the loads of 1500, 600, and 0 lbs. The loads were applied horizontally parallel to the positive and negative X and Y-axis directions. Figure 4.11 shows the calibration curves for Rod nos. 7 and 8 that were obtained when the loads were applied from the positive Y-axis direction. This figure shows the relationship between the axial force, F, in rods and the applied load, P. The

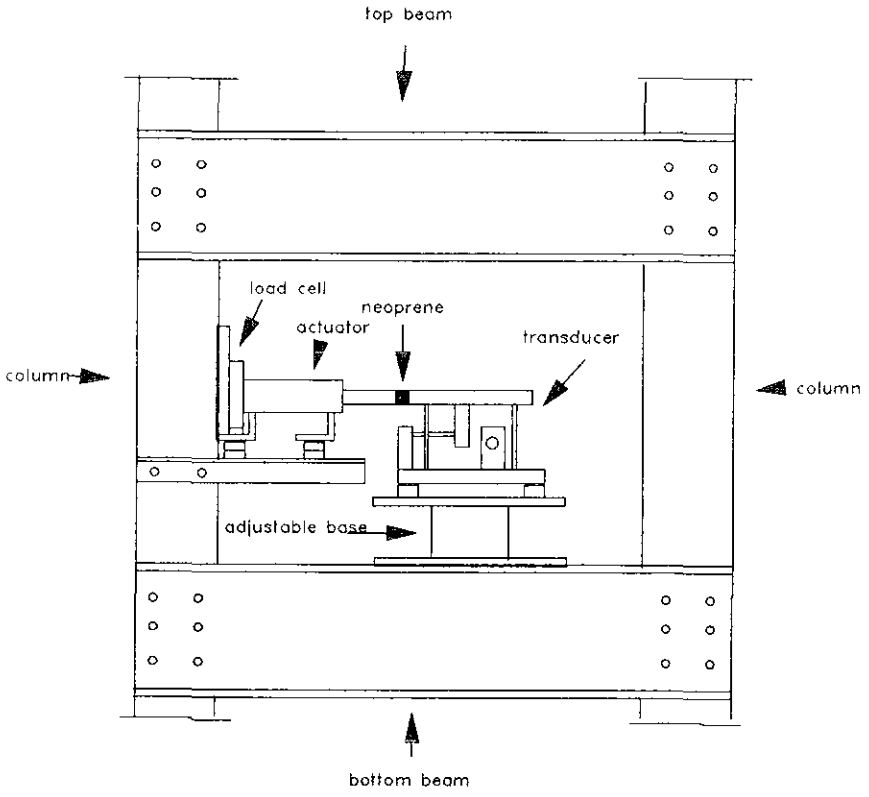

Figure 4.10. The arrangement of the test in the horizontal direction without insulator

calibration curves for the other rods and for negative Y, positive X, and negative X-axis directions are given in Appendix C. These figures show that the slopes for Rod nos. 7 and 8 are almost equal (1% and 2.6% differences for the positive and negative Y-axis directions, respectively). But, the slope For Rod no. 5 is 1.4 and 1.5 times larger than the slope for Rod no. 6, for the positive and negative X-axis directions, respectively. The calibration revealed that the

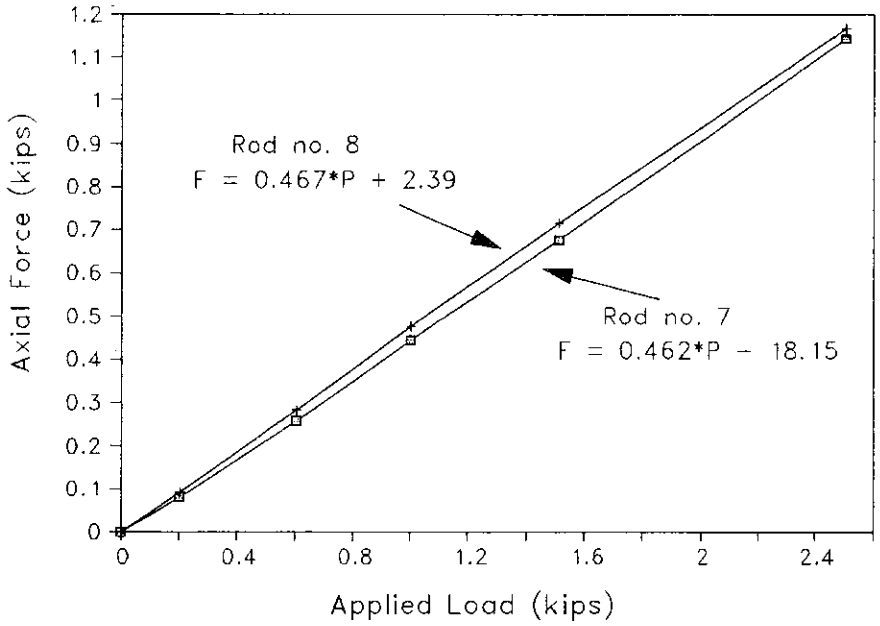

Figure 4.11. Calibration curves for positive Y-axis direction

contribution of the vertical rods and the rods in the Y-axis direction to the stiffness of the transducer in the X-axis direction caused the transducer to respond unsymmetrically.

4.4.2 Vertical direction without insulator

This test consisted of two parts; pushing-down and pulling-up on the top plate of the transducer. The arrangement for the pushing-down test is shown in Figure 4.12. In this test, a neoprene and a round plate with the same diameter as the base of the insulator were placed at the center of the top plate. A load cell was placed on the top of the round plate. The round plate was used to simulate the

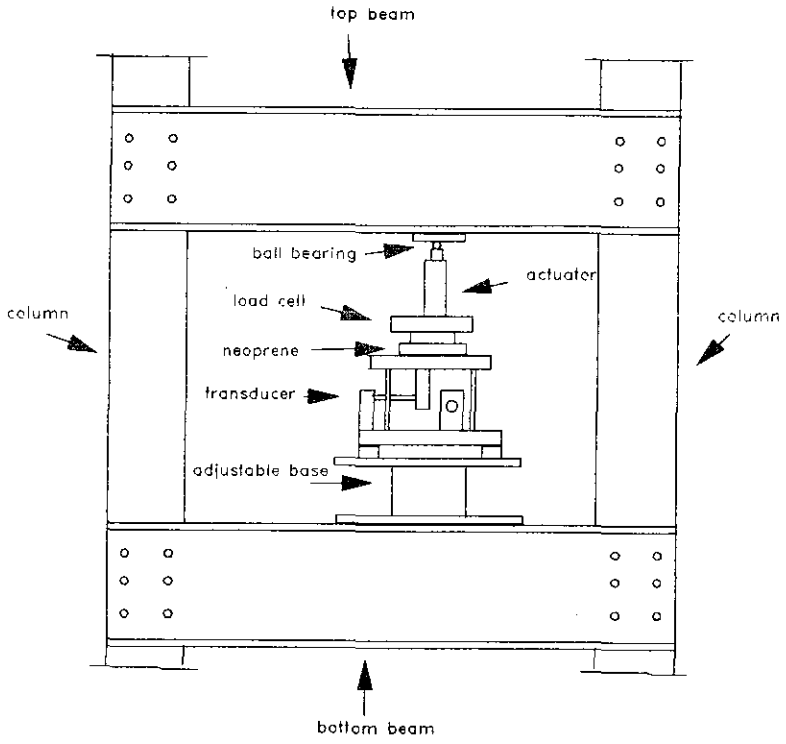

Figure 4.12. The arrangement of the test in the vertical direction (push down)

actual application of a load where an insulator is attached on the top plate of transducer. With the same bearing area, the results of this calibration should be the same as the vertical load calibration with an insulator present. A steel ball bearing was attached to the top of the actuator to prevent the occurrence of an induced bending moment at this location. Without a ball bearing, a non-uniform bearing stress at the ends of the actuator could occur resulting in bending moments at the ends of the actuator. These bending moments could

cause non-vertical loadings. A plate was attached across the top beam of the frame. The actuator acted against the plate and created a vertical compression load on the transducer. The loads were initially increased from 0 to 3500 lbs and then decreased from 3500 to 0 lbs. The strain gage readings were taken when the loads were equal to 0, 250, 500, 1000, 2000, 3500, 2000, 1000, and 0 lbs. The calibration curves for all rods when loads were applied in the positive Z-axis direction are given in Appendix C.

Figure 4.13 shows the arrangement of the pull-up test. In this test, a rod was connected and tightened with a nut to the bottom of top plate of the transducer. The other end of the rod was passed through the core of a hollow tube actuator and tightened with a nut to the top of the actuator. The actuator was placed on the top of the top beam. The upward forces on the top plate of the transducer were created by stretching the rod with the actuator. To simulate the condition occurring in an actual application, a washer was used at the bottom of the top plate of the transducer. Figure 14.14 shows the calibration curve for Rod nos. 1, 2, 3, and 4 that were obtained when the loads were applied from the negative Z-axis direction. This figure shows that the axial forces induced in the four vertical rods were nearly equal. The calibration curves for the other rods are given in Appendix C.

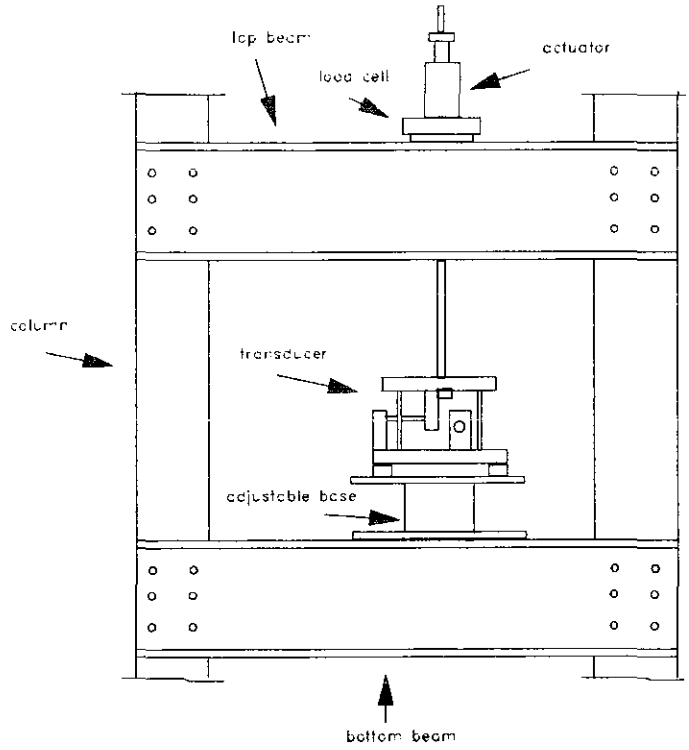

Figure 4.13. The arrangement of the test in the vertical direction (pull-up)

4.4.3 Horizontal direction with insulator

The arrangement of this test is shown in Figure 4.15. An insulator was bolted to the top of the transducer. Loads were applied at the top of the insulator. By applying the loads at the top of insulator, bending moments were induced at the top plate of transducer. The loads were initially increased from 0 to 1500 lbs and then decreased from 1500 to 0 lbs. The

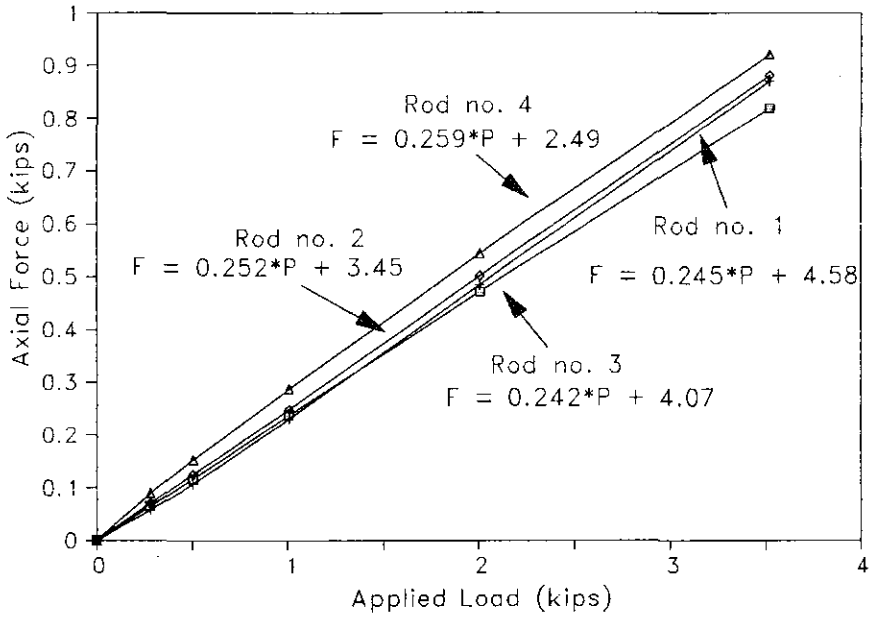

Figure 4.14. Calibration curves for the negative Z-axis direction

strain gage readings were taken when the load were equal to 0, 250, 400, 600, 1000, 1500, 1000, 500, and 0 lbs. Tests were conducted with these loads applied in the positive and negative X and Y-axis directions. The slopes of the regression line obtained for the calibration in positive and negative X-axis and positive and negative Y-axis directions were different by 30% and 27% or less, respectively. The effect of these differences will be discussed in Section 4.6.5. The vertical rods were affected the most by the bending moments. This was due to the bending moments that

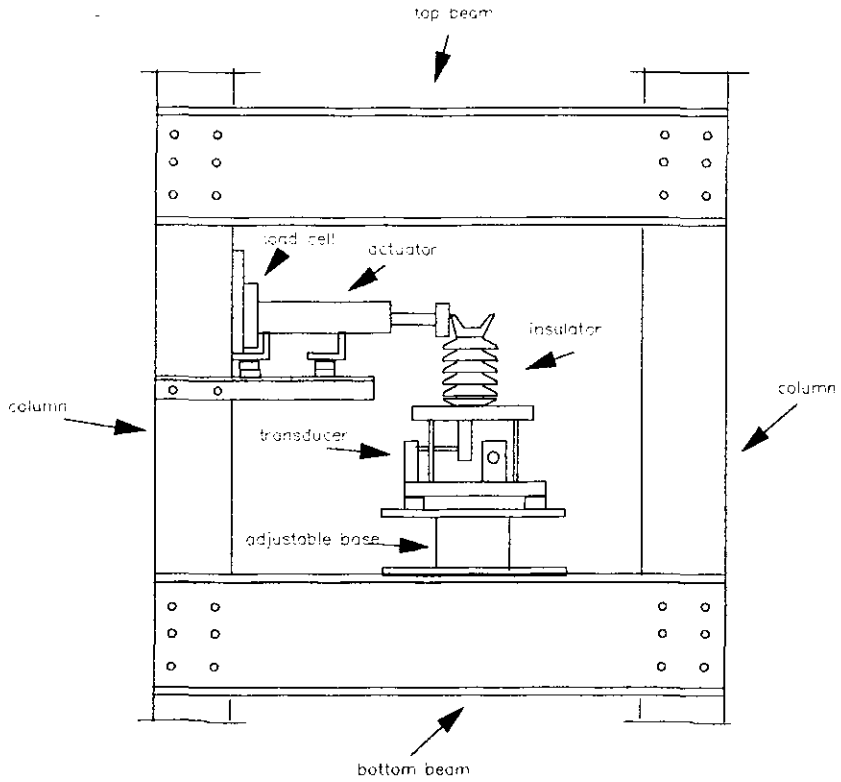

Figure 4.15. The arrangement of the test in the horizontal direction with insulator

were resisted by the couple formed by axial forces in the vertical rods. For the vertical rods, the slopes of the regression lines for the calibration with an insulator were 5 to 7 times larger than the slopes for the calibration without an insulator.

4.4.4. Vertical direction with insulator

As discussed in Section 4.4.2, the arrangements of the calibration for loads in the vertical direction without the

insulator were intended to simulate the actual application where an insulator is attached to the transducer. For pushing-down tests, a round plate with the same diameter as the base of the insulator was placed at the center of the top plate and for pulling-up tests, a washer was used at the bottom of the top plate of the transducer. Since the calibration for the vertical direction with an insulator should produce the same result as the calibration without insulator, the calibration for the vertical direction with an insulator was not performed.

4.5 Combined Vertical and Horizontal Loads Tests

Several tests involving the combination of vertical and horizontal loads were conducted. These combined loads represented the loads induced by galloping and wind. The purpose of the test was to examine the accuracy of the transducer. The examination was done by comparing the magnitudes of the applied loads and the loads measured by the transducer utilizing the approaches discussed in Section 3.8.

4.5.1 Without the insulator

This test used a combination of the testing configurations for the horizontal direction (without an insulator) and vertical direction (pushing-down) calibration tests. The arrangement for this test is shown in Figure 4.16. First, the horizontal load was applied, then, the vertical

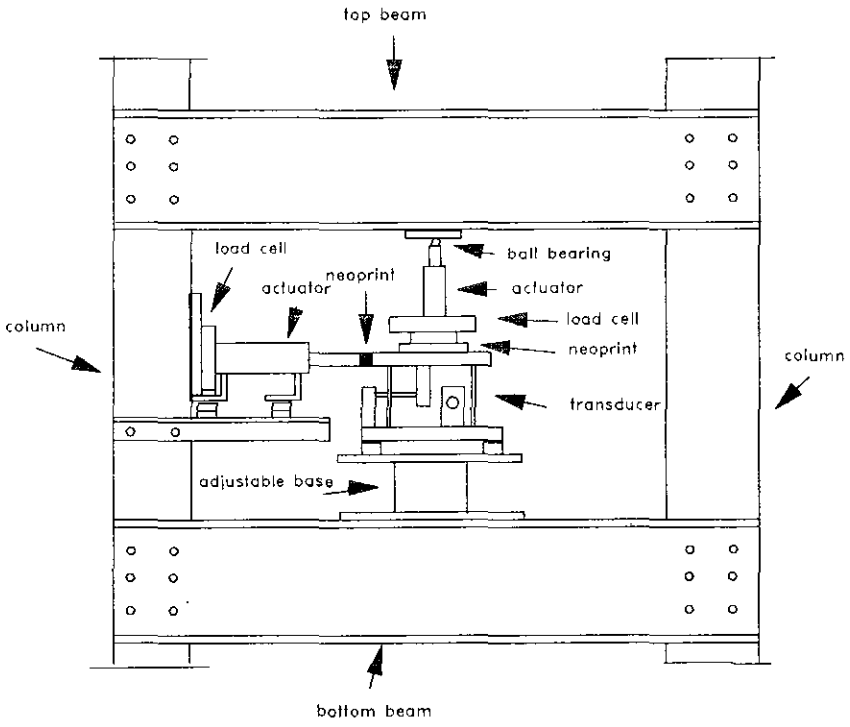

Figure 4.16. The arrangement for the combined loads test (without insulator)

load. The test was conducted for horizontal loads along the X and Y-axis directions. The magnitudes of the applied horizontal loads were 500, 1000, and 2000 lbs. The 500 lbs horizontal load was combined with several vertical loads: 500, 1000, 2000, and 3000 lbs. The 1000 and 2000 lb horizontal loads were combined with a 500 lb vertical load. The results of these tests are discussed in Section 4.6.3.

4.5.2 With the insulator

The arrangement of the test is shown in Figure 4.17. The horizontal loads were applied in the same way as they were for the calibration with the insulator. The vertical loads were applied by using a small actuator clamped to the top beam of the loading frame. A load cell was placed between this beam and the actuator. The actuator acted against a steel plate that was welded to the top of the insulator. The magnitude of the applied horizontal loads were 500, 1000, and 1500 lbs.

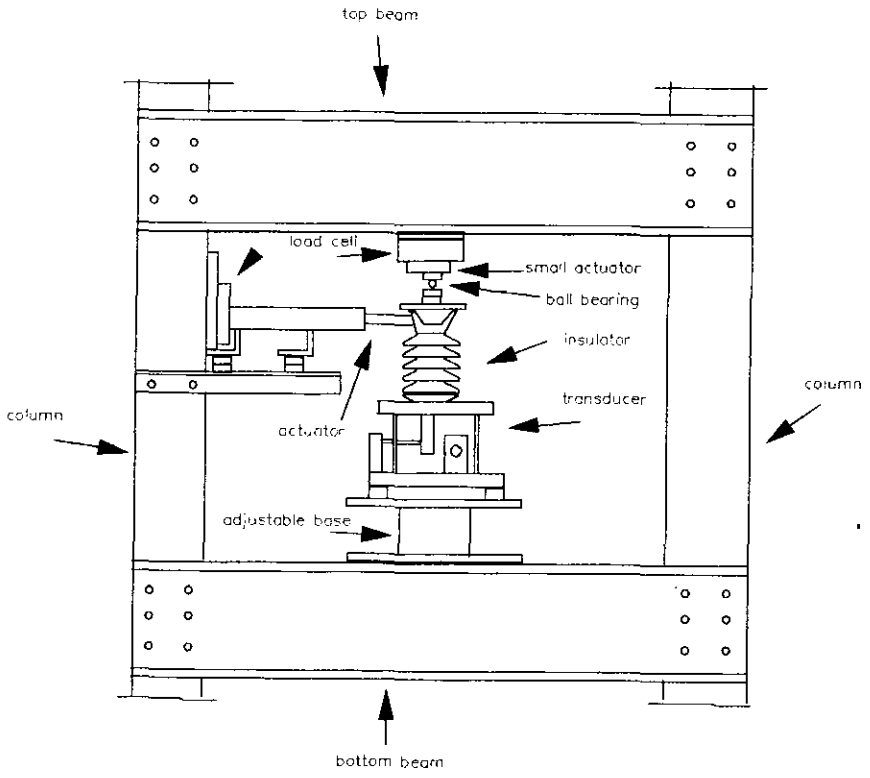

Figure 4.17. The arrangement for the combined loads test (with insulator)

The 500 lb horizontal load was combined with several vertical loads: 500, 1000, 2000, and 3000 lbs. The 1000 and 1500 lb horizontal loads were combined with a 500 lb vertical load. To represent three orthogonal forces, the horizontal loads were applied from different directions in the horizontal plane. These directions were 22.5, 45, 67.5, 135, 225, and 315 degrees from the positive X-axis direction. The results of these tests are discussed in Section 4.6.4.

4.6 Analytical Studies

4.6.1 Results of the calibration without insulator

As discussed in the Chapter 3, the calibration in the X, Y and Z-directions were conducted to obtain the first, second, and the third columns of matrix [A]. The calibration was conducted twice for each direction by applying the loads from the positive and negative directions. For each direction, the average values of the two calibrations were used to determine matrices [A] and [B].

The first three and the last three rows of matrix [A] are the slopes of the regression lines of rod nos. 1 and 8, respectively. Between these rows are the slopes of the regression lines of rod nos. 2, 3, 4, 5, 6, and 7. Each of the three calibrations (X, Y, and Z-axis directions) resulted in three regression lines for each rod. These three regression lines corresponded to the statistical analysis for

the axial force and the two orthogonal shear forces. For rod no. 1, 2, 3, and 4; the first, second and third rows represent rod shear force in the X-axis direction, rod shear force in the Y-axis direction, and rod axial force, respectively. For rod no. 5 and 6; the first, second and third rows represent rod shear force in the Z-axis direction, rod shear force in the Y-axis direction, and rod axial force, respectively. For rod no. 7 and 8; the first, second and third rows represent rod shear force in the Z-axis direction, rod shear force in the X-axis direction, and rod axial force, respectively.

The matrix $[A]_{24x3}$ obtained is given in Figure 4.18. The matrix $[A]^{-1}_{3x24}$, generalized inverse of the matrix [A], as defined in Eq. 3-32 is shown in Figure 4.19. The matrices [B1], [B2], and [B3] which represent the intercepts for the linear regression analyses for the transducer calibration with loads applied in the X, Y, and Z-axis directions, respectively, and the matrix [B], which is the summation of the matrices [B1], [B2], and [B3], obtained are given in Figure 4.20. In Eq. 3-31 the matrix [B] is subtracted from the matrix {U}; and then the results were multiplied by the matrix $[A]^{-1}_{3x24}$ to obtain {P}. Therefore, the significant digits for matrix $[A]_{24x3}$ and matrix $[A]^{-1}_{3x24}$ should be more than the significant digits for matrix [B]. Five significant digits were used for matrix $[A]_{24x3}$ and matrix $[A]^{-1}_{3x24}$, whereas two significant digits were used for the matrix [B].

$[A]_{24x3}$ =

m \ P	P_x	P_y	P_z	Rod no.
1	0.02026	0.00324	0.00037	1
2	-0.00453	0.01380	0.00393	
3	0.10258	0.14951	0.23968	
4	0.02220	0.00117	-0.00462	2
5	-0.00186	0.01285	0.00294	
6	-0.12846	0.13296	0.25226	
7	0.01316	0.00235	-0.00255	3
8	0.00358	0.01400	-0.00306	
9	-0.16295	-0.13535	0.24683	
10	0.01820	-0.00287	0.00628	4
11	-0.00565	0.01502	0.00252	
12	0.15773	-0.14957	0.25772	
13	0.02271	0.00608	0.00614	5
14	-0.01066	0.01391	0.00233	
15	0.37018	-0.01667	0.00595	
16	-0.01487	-0.00219	0.00608	6
17	-0.00058	0.01483	-0.00265	
18	-0.55231	-0.01934	0.01037	
19	-0.00256	0.01210	0.00619	7
20	0.02190	-0.00057	0.00359	
21	0.05919	0.46491	0.01658	
22	0.00395	-0.01462	0.00587	8
23	0.01767	-0.00329	0.00384	
24	0.05601	-0.47335	0.00752	

Figure 4.18. Matrix $[A]_{24x3}$ for calibration without insulator

$[A]^{-1}_{3x24}$ =

P \ m	1	2	3	4	5	6	7	8
Px	.03823	-.00837	.20973	.04155	-.00338	-.22520	.02462	.00643
Py	.00604	.02636	.28262	.00211	.02454	.25261	.00441	.02675
Pz	.00292	.01531	.96842	-.01694	.01154	1.00244	-.00930	-.01217

$[A]^{-1}_{3x24}$ =

P \ m	9	10	11	12	13	14	15	16
Px	-.28865	.03481	-.01094	.31734	.04325	-.02005	.69909	-.02761
Py	-.25990	-.00567	.02877	-.28962	.01138	.02664	-.03470	-.00414
Pz	.98077	.02657	-.01067	1.04779	.02621	.08450	.05077	.02338

$[A]^{-1}_{3x24}$ =

P \ m	17	18	19	20	21	22	23	24
Px	-.00139	-1.0413	-.00448	.04106	.10938	.00798	.03363	.10979
Py	.02837	-.03290	.02308	-.00121	.88799	-.02803	-.00645	-.90523
Pz	-.01083	.00197	.02455	-.01284	.06628	.02398	.01671	.03891

Figure 4.19. Generalized inverse $[A]^{-1}_{3x24}$ for calibration without insulator

m \ -	[B1]	[B2]	[B3]	[B]
1	-0.38	-0.45	-0.14	-0.97
2	-0.11	-0.32	-0.02	-0.45
3	0.66	-4.81	2.11	-2.04
4	-0.84	-1.17	0.30	-1.71
5	0.08	-0.44	0.03	-0.33
6	-0.85	1.80	-8.14	-7.19
7	-0.26	-0.09	-0.17	-0.53
8	-0.14	-0.82	-0.34	-1.30
9	-0.57	5.18	0.85	5.46
10	-0.36	0.24	0.38	0.26
11	-0.17	-0.31	-0.15	-0.63
12	1.05	-0.84	13.04	13.24
13	-0.70	-0.11	0.04	-0.77
14	-0.70	-0.46	-0.22	-1.38
15	6.96	-7.25	1.56	1.27
16	0.32	0.06	0.11	0.49
17	-0.22	-0.74	-0.03	-0.99
18	-9.67	0.56	-2.72	-11.88
19	-0.11	-0.30	0.01	-0.39
20	-0.99	-0.24	-0.01	-1.22
21	0.88	-9.99	-2.66	-11.78
22	-0.02	-0.14	0.28	0.13
23	-0.39	0.06	0.02	-0.31
24	-3.28	-11.25	1.55	-12.98

Figure 4.20. Matrix [B] for calibration without insulator

For the calibration involving only axial forces, $[A]_{8x3}$ and $[B]_{8x1}$ are submatrix of the matrix $[A]_{24x3}$ and $[B]_{24x1}$, respectively. The elements of the matrices $[A]_{8x3}$ and $[B]_{8x1}$ were the coefficients of the regression lines of axial forces versus applied loads.

$[A]_{8x3}$ =

m \ P	P_x	P_y	P_z
1	0.10258	0.14951	0.23968
2	-0.12846	0.13296	0.25226
3	-0.16295	-0.13535	0.24683
4	0.15773	-0.14957	0.25772
5	0.37018	-0.01667	0.00595
6	-0.55231	-0.01934	0.01037
7	0.05919	0.46491	0.01658
8	0.05601	-0.47335	0.00752

$[B]_{8x1}$ =

m \ -	1
1	-2.04
2	-7.19
3	5.46
4	13.24
5	1.27
6	-11.88
7	-11.78
8	-12.98

The generalized inverse $[A]^{-1}_{3x8}$ obtained by Eq. 3-32 was

$[A]^{-1}_{3x8}$ =

P \ m	1	2	3	4	5	6	7	8
P_x	.211	-.227	-.290	.319	.703	-1.048	.110	.111
P_y	.283	.254	-.261	-.291	-.035	-.033	.891	-.908
P_z	.970	1.004	.982	1.049	.051	.002	.066	.039

4.6.2 Results of the calibration with insulator

The procedure used to form the matrix [A] for the transducer calibration with an insulator is the same as the approach to form the matrix [A] for the calibration without an insulator. The matrix $[A]_{24x3}$ is shown in Figure 4.21, whereas the matrices $[B1]_{24x1}$, $[B2]_{24x1}$, $[B3]_{24x1}$, and $[B]_{24x1}$ are shown in Figure 4.22. The generalized inverse $[A]^{-1}_{3x24}$ is shown in Figure 4.23.

The matrices $[A]_{8x3}$ and $[B]_{8x1}$ for the calibrations considering only axial forces in the eight rods and with the insulator attached to the transducer are given by

$[A]_{8x3}$ =

m \ P	P_x	P_y	P_z
1	0.73742	0.76303	0.23968
2	-0.71368	0.77047	0.25226
3	-0.80853	-0.76192	0.24683
4	0.81173	-0.80952	0.25772
5	0.33322	0.01198	0.00595
6	-0.50744	-0.01968	0.01037
7	0.06937	0.42624	0.01658
8	0.06107	-0.44828	0.00752

$[B]_{8x1}$ =

m \ -	1
1	6.00
2	15.15
3	24.94
4	25.69
5	-3.56
6	-3.14
7	-3.04
8	10.34

The generalized inverse $[A]^{-1}_{3x8}$ obtained by Eq. 3-32 was

$[A]^{-1}_{3x8}$=

P \ m	1	2	3	4	5	6	7	8
P_x	.268	-.261	-.298	.293	.122	-.185	.026	.022
P_y	.280	.280	-.268	-.283	.005	-.007	.153	-.160
P_z	.976	1.036	.980	1.011	.022	.045	.076	.020

As discussed in section 4.4.3, the average values of the slope and intercept of the linear regression lines for the transducer calibrations for the positive and negative X-axis, for the positive and negative Y-axis directions and for the positive and negative Z-axis directions were used to establish the matrix [A]. In section 4.6.5, a sensitivity study was conducted to study the effect of using the average values as elements of matrix [A]. Another approach of establishing

$[A]_{24x3}$ =

m \ P	P_x	P_y	P_z	Rod no.
1	0.02022	0.00359	0.00037	1
2	0.00263	0.01583	0.00393	
3	0.73742	0.76303	0.23968	
4	0.02369	-0.00576	-0.00462	2
5	-0.00721	0.01885	0.00294	
6	-0.71368	0.77047	0.25226	
7	0.01870	0.00899	-0.00255	3
8	0.00844	0.01323	-0.00306	
9	-0.80853	-0.76192	0.24683	
10	0.02288	-0.01219	0.00628	4
11	-0.01191	0.02150	-0.00252	
12	0.81173	-0.80952	0.25772	
13	0.03273	0.01323	0.00614	5
14	-0.00996	0.01324	0.00233	
15	0.33322	0.01198	0.00595	
16	-0.02391	-0.00960	0.00608	6
17	0.00207	0.01382	-0.00265	
18	-0.50744	-0.01968	0.01037	
19	-0.00878	0.02131	0.00619	7
20	0.02213	-0.00389	-0.00359	
21	0.06937	0.42624	0.01658	
22	0.01098	-0.02300	0.00587	8
23	0.01714	-0.00533	0.00384	
24	0.06107	-0.44828	0.00752	

Figure 4.21. Matrix $[A]_{24x3}$ for calibration with insulator

m	[B1]	[B2]	[B3]	[B]
1	1.04	0.44	-0.02	1.34
2	0	0.24	-0.02	0.22
3	4.24	-0.35	2.11	6.00
4	-0.17	-0.66	0.30	-0.53
5	0.31	0.44	0.03	0.78
6	12.96	10.33	-8.14	15.15
7	0.31	-0.03	-0.17	0.11
8	0.35	0.27	-0.34	0.28
9	23.14	0.95	0.85	24.94
10	0.24	0.88	0.38	1.50
11	0.13	0.57	-0.15	0.55
12	1.15	11.50	13.04	25.69
13	0.08	-0.74	0.04	-0.62
14	-0.60	-0.04	-0.22	0.86
15	-5.31	0.10	1.56	-3.56
16	0.89	0.17	0.11	1.17
17	0.56	0.18	-0.03	0.71
18	-3.23	2.81	-2.72	-3.14
19	-0.11	0.21	0.01	0.11
20	0.36	0.20	-0.01	0.55
21	2.97	-3.35	-2.66	-3.04
22	0.06	0.82	0.28	1.16
23	0.26	0.18	0.02	0.46
24	0.71	8.08	1.55	10.34

Figure 4.22. Matrix [B] for calibration with insulator

$[A]^{-1}_{3x24}$ =

P \ m	1	2	3	4	5	6	7	8
Px	.00736	.00096	.26800	.00865	-.00261	-.26022	.00684	.00312
Py	.00132	.00575	.27945	-.00213	.00680	.28008	.00318	.00467
Pz	.00143	.01612	.97464	-.01882	.01228	1.03511	-.01014	-.01204

$[A]^{-1}_{3x24}$ =

P \ m	9	10	11	12	13	14	15	16
Px	-.29716	.00826	-.00428	.29241	.01189	-.00362	.12126	-.00876
Py	-.26807	-.00418	.00761	-.28225	.00492	.00477	.00495	-.00333
Pz	.97896	.02479	-.00955	1.01067	.02471	.00972	.02192	.02437

$[A]^{-1}_{3x24}$ =

P \ m	17	18	19	20	21	22	23	24
Px	.00079	.18479	-.00320	.00807	.02582	.00392	.00620	.02146
Py	.00488	.00761	.00775	-.00144	.15288	-.00807	-.00179	-.16001
Pz	-.01035	.04459	.02540	-.01466	.07584	.02295	.01516	.01955

Figure 4.23. Generalized inverse $[A]^{-1}_{3x24}$ for calibration with insulator

matrix [A] is by performing a linear regression for all of the data collected from calibration for the positive and negative directions. For example, the data obtained from calibration for the positive and negative X-directions are collectively used to obtain the relationship between the rod internal forces and the loads applied in the X direction. Figures 4.24, 4.25, and 4.26 show the regression lines that relate the applied load in the X-direction and axial force in the rod no. 5, the applied load in the Y-direction and axial force in the

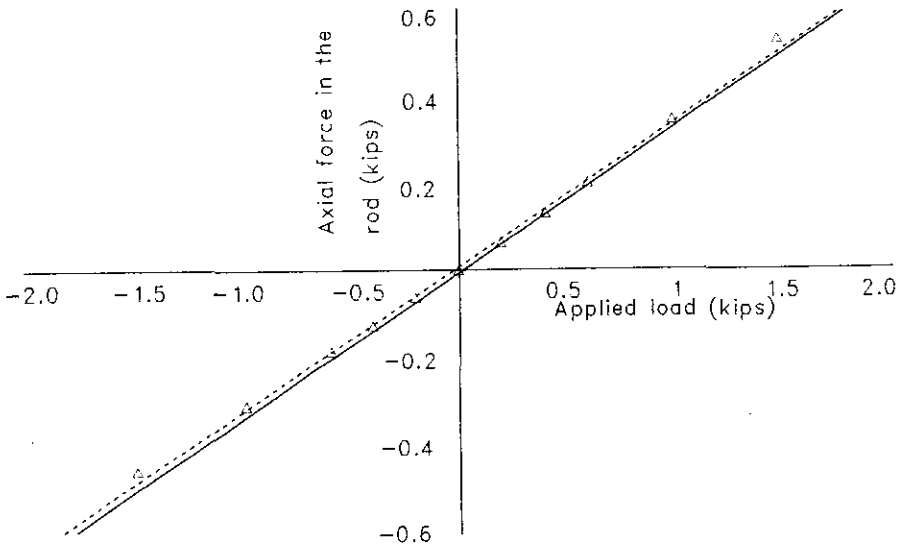

Figure 4.24. Regression lines for axial force of rod no. 5

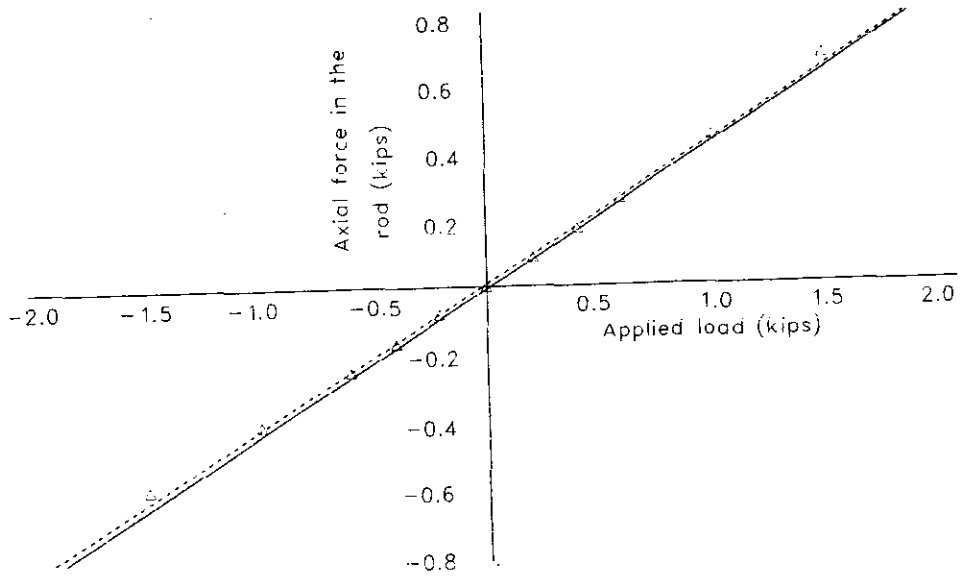

Figure 4.25. Regression lines for axial force of rod no. 7

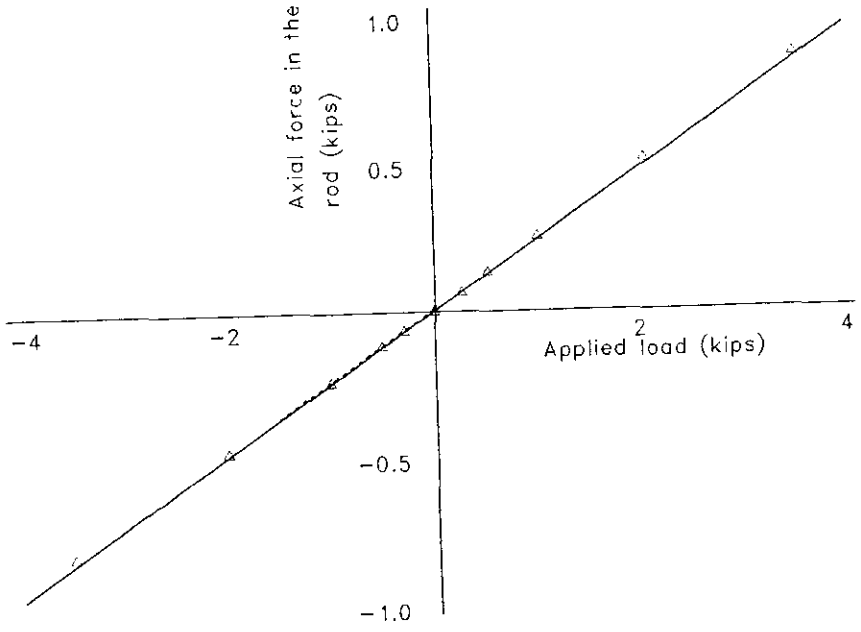

Figure 4.26. Regression lines for axial force of rod no. 1

rod no. 7, and the applied load in the Z-direction and axial force in the rod no. 1, respectively. Each figure shows two regression lines; a line obtained by using the average values of two regression lines of calibration for positive and negative directions (represented by solid line) and a regression line obtained by collectively using the data of calibration for the positive and negative directions (represented by dotted line). The approach that used the average values of two regression lines of calibration for positive and negative directions was used in this thesis. Although the approach that collectively used data of calibration for the positive and negative directions are statistically more appropriate, Figures 4.24 to 4.26 show both approach produce essentially the same slopes and intercepts; therefore using the average values of slopes and intercepts of regression lines of calibration for the positive and negative directions is justified.

4.6.3 Results of the combined load tests without insulator

The axial forces and shear forces in the rods obtained from the combined loads tests were used to form the matrix {U}. Utilizing Eq. 3-31 and the matrices listed in Section 4.6.2, the applied loads can be determined. Two solutions are possible, depending on whether or not the shear forces in the rods are considered. Besides utilizing Eq. 3-31, the applied loads could be calculated from the statical equilibrium of the

experimentally established internal rod forces. The internal forces are the axial forces and shear forces obtained from the test as discussed in Section 3.8.

Table 4.1 shows the comparison of the applied loads established by these approaches for tests not involving an insulator. The sign for the loads was determined from direction of the loads. The loads applied in the positive X, Y, and Z-axis directions have a positive sign, while the loads applied in the negative X, Y, and Z-axis directions have a negative sign. The numbers in the parenthesis are the differences between the calculated load and the applied load expressed as the percentage of the applied load. The dash sign in a parenthesis means that the percentage difference calculations are not applicable since a load was not actually applied in that particular direction. The complete results of the tests without the insulator are given in Appendix D. These results show that the force calculation approaches utilizing the matrix $[A]_{24x3}$ and $[A]_{8x3}$ produce the same results. Generally, the equilibrium approach, which requires all of the strain gages, provided more accurate results compare to the other two approaches, but, for some tests the matrix approach provided more accurate results.

4.6.4 Results of the combined load test with insulator

At the time when the combined load tests were conducted, the full-bridge strain gage configuration for Rod no. 4 and

Table 4.1. Comparison of loads measured by various approaches in tests without insulator

Load / Approach	P_x (lbs)	P_y (lbs)	P_z (lbs)	Test
measurement	0	-437	3057	1
equilibrium	-2 (-)	-456(4.3%)	3085(0.9%)	
$[A]_{24x3}$	-48(-)	-388(11.2%)	3039(0.6%)	
$[A]_{8x3}$	-48(-)	-388(11.2%)	3039(0.6%)	
measurement	439	0(-)	3037	2
equilibrium	444(1.1%)	-31(-)	3039(0.1%)	
$[A]_{24x3}$	375(14.6%)	10(-)	2970(2.2%)	
$[A]_{8x3}$	374(14.6%)	10(-)	2970(2.2%)	
measurement	0	487	3022	3
equilibrium	17(-)	436(10.5%)	2992(1%)	
$[A]_{24x3}$	-18(-)	442(9.2%)	2938(2.8%)	
$[A]_{8x3}$	-18(-)	442(9.2%)	2938(2.8%)	
measurement	-500	0	3048	4
equilibrium	-458(8.4%)	-12(-)	3061(0.4%)	
$[A]_{24x3}$	-484(3.2%)	16(-)	3021(0.9%)	
$[A]_{8x3}$	-484(3.2%)	16(-)	3020(0.9%)	

four quarter-bridge strain gage configurations; Nos. 1, 6, 7, and 8 for Rod no. 8 (see Figure 3.6) malfunctioned. Therefore, readings for these gages had to be mathematically generated. For the full-bridge strain gages of Rod no. 4, the data were generated from the established relationship between the full-bridge strain gages readings and the quarter-bridge strain gages readings of this rod. The data used were the data obtained before the strain gages malfunctioned. The results of this generation are shown in Figure 4.27. This figure shows the relationship of full-bridge reading, FB, and quarter-bridge reading, QB.

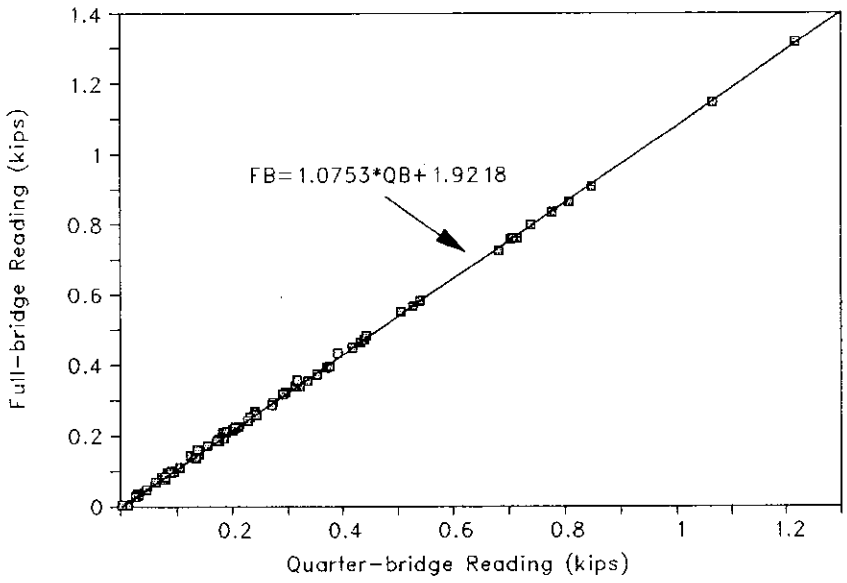

Figure 4.27. Data generation for full-bridge strain gages of rod no. 4

For the quarter-bridge strain gages of Rod no. 8, the data for the malfunctioning strain gages were generated from the remaining quarter-bridge strain gages on Rod no. 8. The data for strain gage no. 8 were generated from data of strain gage no. 4, with the assumption that the moments at these two locations on the rod are equal. This assumption is acceptable since the conditions at both ends of the rods are essentially the same; fixed by the nuts. The induced end moments are due to the relative displacement of the ends of the rod. The results of this generation are shown in Figure 4.28. This figure shows the relationship between strains on gage no. 8, G8, and gage no. 4, G4.

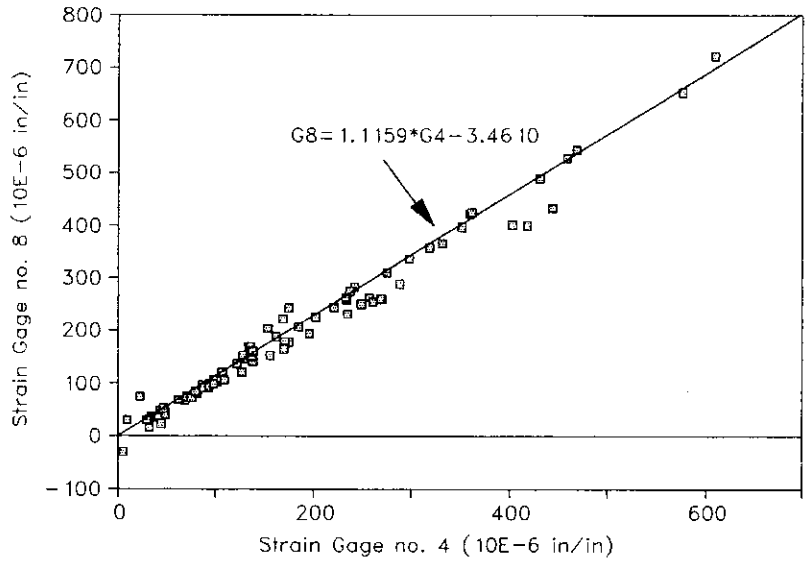

Figure 4.28. The relationship between strain at gage no. 8 and gage no. 4

The data for strain gage no. 1 were generated from strain gage no. 3 and from the full-bridge strain gages on Rod no.8. The strains at gage no. 1 induced by the axial force should be equal to the strain at gage no. 3. The bending strain at these two gages are equal in magnitude but opposite in sign. Therefore, the strain at gage no. 1 is proportional to the quantity defined by subtracting the strain at gage no. 3 (G3) from twice the axial strain at the full-bridge (D). The results of this analysis are shown in Figure 4.29.

Since the loads computed by utilizing matrix $[A]_{24x3}$ and by utilizing matrix $[A]_{8x3}$ were equal, the matrix $[A]_{8x3}$ was used for the tests with the insulator. Besides using this approach, the calculation by using statical equilibrium was

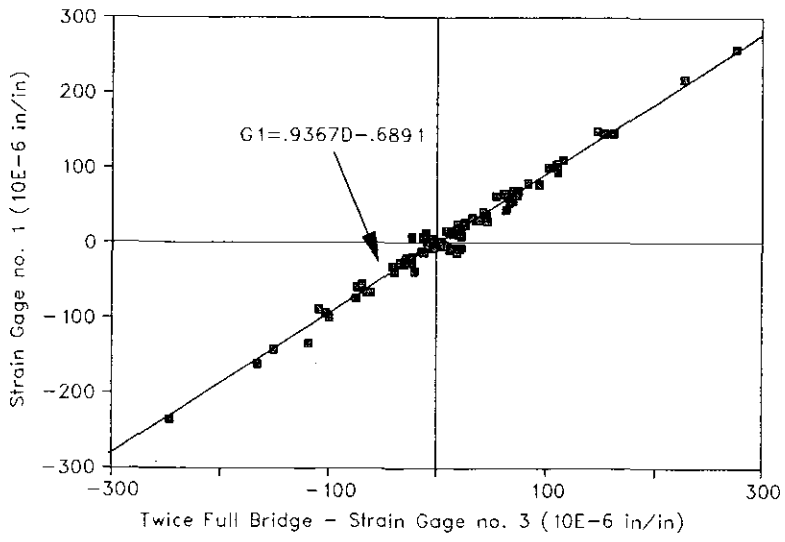

Figure 4.29. Data generation for strain gage no. 1

used to determined the applied loads as well. Table 4.2 shows some of the results of these combined tests. The sign convention for loads and the calculation procedures are the same as for Table 4.1. The complete results of the tests with

Table 4.2. Comparison of loads measured by various approaches in with insulator

Load / Approach	Px (lbs)	Py (lbs)	Pz (lbs)	Test
measurement	-608	-1467	534	1
$[A]_{8x3}$	-719(18.3%)	-1496(2.0%)	599(12.2%)	
equilibrium	-681(12%)	-1416(3.5%)	513(3.9%)	
measurement	-1157	1157	618	2
$[A]_{8x3}$	-1186(2.5%)	1186(2.5%)	652(5.5%)	
equilibrium	-1128(2.5%)	1103(4.7%)	668(8.1%)	
measurement	1107	1107	598	3
$[A]_{8x3}$	1231(11.2%)	1109(0.2%)	738(23.4%)	
equilibrium	1145(3.4%)	1059(4.3%)	675 (12.9%)	
measurement	812	-812	520	4
$[A]_{8x3}$	883(8.7%)	-862(6.2%)	564(8.5%)	
equilibrium	833(2.6%)	-815(0.4%)	428(17.7%)	

the insulator are given in Appendix D. Generally, the equilibrium approach, which requires all of the strain gages, provided more accurate results compare to the other two approaches, but, for some tests the matrix approach provided more accurate results.

As discussed in Section 4.6.2, two approaches can be used in establishing the matrix [A]; by using the average values of the linear regression coefficients from the two regression lines associated with the calibrations for the positive and negative directions (defined as approach A) and by collectively using all of the data related to the calibrations for both the positive and negative directions (defined as approach B). The comparison of the loads calculated by using these two approaches is presented in Table 4.3. Table 4.3 shows that for certain cases the approach A produces better result, but for other cases approach B produces better result. The difference between the results of the two approaches are small (less than 5%).

4.6.5 Sensitivity study

A sensitivity study was performed to study the effect of a change in an element of the matrix [A] on the computed load result. The elements (3,3), (15,1), (18,1), (21,2), and (24,2) of the matrix [A] which are associated with axial forces in rod no. 1, no. 5, no. 6, no. 7, and no. 8, respectively, were increased or decreased by 5, 10, and 15%.

Table 4.3. Loads calculated by approach A and B

Load / Approach	Px (lb)	Py (lb)	Pz(lb)	Test no.
Measurement	-712	-712	502	1
Approach A	-727(2.1%)	-691(2.9%)	571(13.7%)	
Approach B	-728(2.2%)	-683(4.1%)	556(10.8%)	
Measurement	812	-812	520	2
Approach A	883(8.7%)	-862(6.2%)	564(8.5%)	
Approach B	869(7.0%)	-848(4.4%)	516(0.8%)	
Measurement	-1157	1157	618	3
Approach A	-1186(2.5%)	1186(2.5%)	652(5.5%)	
Approach B	-1179(1.9%)	1180(2.0%)	651(5.3%)	
Measurement	1107	1107	598	4
Approach A	1231(11.2%)	1109(0.2%)	738(23.4%)	
Approach B	1240(12.0%)	1088(1.7%)	767(28.3%)	

The results of this study are summarized in Tables 4.4, 4.5, 4.6, 4.7, and 4.8, and Figures. 4.30, 4.31, 4.32, 4.33, and 4.34. Cases 1, 2, 3, 4, 5, and 6 are 5% increment, 5% decrement, 10% increment, 10% decrement, 15% increment, and 15% decrement, respectively. These tables show that a change in an element of matrix [A] affects the loads acting in the direction of the rod which is associated to that element, more than the loads in other two directions. For instance, by changing element (3,3) which is associated with axial forces in the vertical rod (no.1), the changes in the X and Y

Table 4.4. Results of the sensitivity study for element (3,3)

Load / Approach	P_x (lbs)	P_y (lbs)	P_z (lbs)	Test
Measurement	-608	-1467	534	1
$[A]_{24x3}$	-719	-1496	599	
Case 1	-717(-0.3%)	-1494(-0.1%)	597(-0.3%)	
Case 2	-721(0.3%)	-1498(0.1%)	600(0.2%)	
Case 3	-715(-0.6%)	-1492(-0.3%)	595(-0.7%)	
Case 4	-723(0.6%)	-1500(0.3%)	601(0.3%)	
Case 5	-713(-0.8%)	-1490(-0.4%)	592(-1.2%)	
Case 6	-725(0.8%)	-1502(0.4%)	601(0.3%)	
Measurement	-1157	1157	618	2
$[A]_{24x3}$	-1186	1186	652	
Case 1	-1184(-0.2%)	1188(0.2%)	638(-2.1%)	
Case 2	-1188(0.2%)	1183(-0.3%)	665(2.0%)	
Case 3	-1182(-0.3%)	1190(0.3%)	625(-4.1%)	
Case 4	-1190(0.3%)	1181(-0.4%)	679(4.1%)	
Case 5	-1180(-0.5%)	1192(0.5%)	612(-6.1%)	
Case 6	-1193(0.6%)	1179(-0.6%)	692(6.1%)	

Table 4.4. (continued)

Load / Approach	P_x (lbs)	P_y (lbs)	P_z (lbs)	Test
Measurement	1107	1107	598	3
$[A]_{24x3}$	1231	1109	738	
Case 1	1234(0.2%)	1111(0.2%)	736(-0.3%)	
Case 2	1229(-0.2%)	1106(-0.3%)	740(0.3%)	
Case 3	1236(0.4%)	1114(0.5%)	733(-0.7%)	
Case 4	1227(-0.3%)	1104(-0.5%)	741(0.4%)	
Case 5	1238(0.6%)	1116(0.6%)	730(-1.1%)	
Case 6	1224(-0.6%)	1101(-0.7%)	742(0.5%)	
Measurement	812	-812	520	4
$[A]_{24x3}$	883	-862	564	
Case 1	885(0.2%)	-860(-0.2%)	553(-2.0%)	
Case 2	881(-0.2%)	-864(0.2%)	574(1.8%)	
Case 3	886(0.3%)	-859(-0.3%)	543(-3.7%)	
Case 4	879(-0.5%)	-866(0.5%)	585(3.7%)	
Case 5	888(0.6%)	-857(-0.6%)	533(-5.5%)	
Case 6	877(-0.7%)	-868(0.7%)	595(5.5%)	

Table 4.5. Results of the sensitivity study for element (15,1)

Load / Approach	P_x (lbs)	P_y (lbs)	P_z (lbs)	Test
Measurement	-608	-1467	534	1
$[A]_{24x3}$	-719	-1496	599	
Case 1	-717(-0.3%)	-1496(0.0%)	598(-0.2%)	
Case 2	-721(0.3%)	-1496(0.0%)	598(-0.2%)	
Case 3	-715(-0.6%)	-1496(0.0%)	598(-0.2%)	
Case 4	-722(0.4%)	-1496(0.0%)	599(0.0%)	
Case 5	-713(-0.8%)	-1495(-0.07%)	598(-0.2%)	
Case 6	-724(0.7%)	-1496(0.0%)	599(0.0%)	
Measurement	812	-812	520	2
$[A]_{24x3}$	883	-862	564	
Case 1	881(-0.2%)	-862(0.0%)	564(0.0%)	
Case 2	885(0.2%)	-862(0.0%)	563(-0.2%)	
Case 3	878(-0.6%)	-862(0.0%)	564(0.0%)	
Case 4	887(0.5%)	-862(0.0%)	563(-0.2%)	
Case 5	876(-0.8%)	-862(0.0%)	565(0.2%)	
Case 6	888(0.6%)	-862(0.0%)	563(-0.2%)	

Table 4.5. (continued)

Load / Approach	P_x (lbs)	P_y (lbs)	P_z (lbs)	Test
Measurement	1107	1107	598	3
$[A]_{24x3}$	1231	1109	738	
Case 1	1229(-0.2%)	1109(0.0%)	738(0.0%)	
Case 2	1234(0.2%)	1108(-0.09%)	738(0.0%)	
Case 3	1226(-0.4%)	1109(0.0%)	739(0.1%)	
Case 4	1236(0.4%)	1109(0.0%)	737(-0.1%)	
Case 5	1223(-0.6%)	1108(-0.09%)	739(0.1%)	
Case 6	1237(0.5%)	1109(0.0%)	737(-0.1%)	
Measurement	-1157	1157	618	4
$[A]_{24x3}$	-1186	1186	652	
Case 1	-1184(-0.2%)	1186(0.0%)	651(-0.2%)	
Case 2	-1188(0.2%)	1186(0.0%)	652(0.0%)	
Case 3	-1181(-0.4%)	1186(0.0%)	650(-0.3%)	
Case 4	-1190(0.3%)	1186(0.0%)	652(0.0%)	
Case 5	-1178(-0.7%)	1186(0.0%)	650(-0.3%)	
Case 6	-1192(0.5%)	1185(-0.08%)	653(0.2%)	

Table 4.6. Results of the sensitivity study for element (18,1)

Load / Approach	P_x (lbs)	P_y (lbs)	P_z (lbs)	Test
Measurement	-608	-1467	534	1
$[A]_{24x3}$	-719	-1496	599	
Case 1	-716(-0.4%)	-1496(0.0%)	599(0.0%)	
Case 2	-722(0.4%)	-1496(0.0%)	598(-0.2%)	
Case 3	-712(-1.0%)	-1495(-0.07%)	600(0.2%)	
Case 4	-725(0.8%)	-1496(0.0%)	597(-0.3%)	
Case 5	-708(-1.5%)	-1495(-0.07%)	601(0.3%)	
Case 6	-728(1.3%)	-1496(0.0%)	596(-0.5%)	
Measurement	812	-812	520	2
$[A]_{24x3}$	883	-862	564	
Case 1	879(-0.5%)	-862(0.0%)	563(-0.2%)	
Case 2	886(0.3%)	-862(0.0%)	565(0.2%)	
Case 3	874(-1.0%)	-863(0.1%)	562(-0.4%)	
Case 4	890(0.8%)	-862(0.0%)	566(0.4%)	
Case 5	870(-1.5%)	-863(0.1%)	561(-0.5%)	
Case 6	893(1.1%)	-862(0.0%)	567(0.5%)	

Table 4.6. (continued)

Load / Approach	P_x (lbs)	P_y (lbs)	P_z (lbs)	Test
Measurement	1107	1107	598	3
$[A]_{24x3}$	1231	1109	738	
Case 1	1225(-0.5%)	1109(0.0%)	737(-0.1%)	
Case 2	1238(0.6%)	1109(0.0%)	739(0.1%)	
Case 3	1217(-1.1%)	1108(-0.09%)	735(-0.4%)	
Case 4	1244(1.1%)	1109(0.0%)	741(0.4%)	
Case 5	1210(-1.7%)	1108(-0.09%)	734(-0.5%)	
Case 6	1249(1.5%)	1109(0.0%)	742(0.5%)	
Measurement	-1157	1157	618	4
$[A]_{24x3}$	-1186	1186	652	
Case 1	-1180(-0.5%)	1186(0.0%)	653(0.2%)	
Case 2	-1192(0.5%)	1186(0.0%)	650(-0.3%)	
Case 3	-1173(-1.1%)	1186(0.0%)	654(0.3%)	
Case 4	-1197(0.9%)	1185(-0.08%)	649(-0.5%)	
Case 5	-1166(-1.7%)	1186(0.0%)	655(0.5%)	
Case 6	-1202(1.3%)	1185(-0.08%)	647(-0.8%)	

Table 4.7. Results of the sensitivity study for element (21,2)

Load / Approach	P_x (lbs)	P_y (lbs)	P_z (lbs)	Test
Measurement	-608	-1467	534	1
$[A]_{24x3}$	-719	-1496	599	
Case 1	-718(-0.1%)	-1490(-0.4%)	596(-0.5%)	
Case 2	-720(0.1%)	-1500(0.3%)	601(0.3%)	
Case 3	-717(-0.3%)	-1485(-0.7%)	594(-0.8%)	
Case 4	-721(0.3%)	-1505(0.6%)	603(0.7%)	
Case 5	-717(-0.3%)	-1481(-1.0%)	592(-1.2%)	
Case 6	-721(0.3%)	-1508(0.8%)	605(1.0%)	
Measurement	812	-812	520	2
$[A]_{24x3}$	883	-862	564	
Case 1	883(0.0%)	-859(-0.3%)	562(-0.4%)	
Case 2	882(-0.1%)	-865(0.3%)	565(0.2%)	
Case 3	884(0.1%)	-855(-0.8%)	561(-0.5%)	
Case 4	882(-0.1%)	-868(0.7%)	567(0.5%)	
Case 5	884(0.1%)	-852(-1.2%)	560(-0.7%)	
Case 6	882(-0.1%)	-870(0.9%)	568(0.7%)	

Table 4.7. (continued)

Load / Approach	P_x (lbs)	P_y (lbs)	P_z (lbs)	Test
Measurement	1107	1107	598	3
$[A]_{24x3}$	1231	1109	738	
Case 1	1231(0.0%)	1104(-0.5%)	740(0.3%)	
Case 2	1232(0.08%)	1113(0.5%)	736(-0.3%)	
Case 3	1230(-0.08%)	1100(-0.8%)	742(0.5%)	
Case 4	1233(0.2%)	1116(0.6%)	734(-0.5%)	
Case 5	1230(-0.08%)	1097(-1.1%)	743(0.7%)	
Case 6	1233(0.2%)	1119(0.9%)	733(-0.7%)	
Measurement	-1157	1157	618	4
$[A]_{24x3}$	-1186	1186	652	
Case 1	-1187(0.08%)	1182(-0.3%)	653(0.2%)	
Case 2	-1185(-0.08%)	1189(0.3%)	649(-0.5%)	
Case 3	-1187(0.08%)	1178(-0.7%)	655(0.5%)	
Case 4	-1185(-0.08%)	1192(0.5%)	648(-0.6%)	
Case 5	-1188(0.2%)	1175(-0.9%)	657(0.8%)	
Case 6	-1184(-0.2%)	1194(0.7%)	646(-0.9%)	

Table 4.8. Results of the sensitivity study for element (24,2)

Load / Approach	P_x (lbs)	P_y (lbs)	P_z (lbs)	Test
Measurement	-608	-1467	534	1
$[A]_{24x3}$	-719	-1496	599	
Case 1	-720(0.1%)	-1490(-0.4%)	599(0.0%)	
Case 2	-718(-0.1%)	-1501(0.3%)	598(-0.2%)	
Case 3	-720(0.1%)	-1484(-0.8%)	600(0.2%)	
Case 4	-717(-0.3%)	-1506(0.7%)	597(-0.3%)	
Case 5	-721(0.3%)	-1479(-1.1%)	600(0.2%)	
Case 6	-717(-0.3%)	-1509(0.9%)	597(-0.3%)	
Measurement	812	-812	520	2
$[A]_{24x3}$	883	-862	564	
Case 1	882(-0.1%)	-859(-0.3%)	564(0.0%)	
Case 2	883(0.0%)	-865(0.3%)	563(-2.0%)	
Case 3	882(-0.1%)	-856(-0.7%)	564(0.0%)	
Case 4	884(0.1%)	-868(0.7%)	563(-0.2%)	
Case 5	882(-0.1%)	-853(-1.0%)	564(0.0%)	
Case 6	884(0.1%)	-869(0.8%)	563(-0.2%)	

Table 4.8. (continued)

Load / Approach	P_x (lbs)	P_y (lbs)	P_z (lbs)	Test
Measurement	1107	1107	598	3
$[A]_{24x3}$	1231	1109	738	
Case 1	1232(0.08%)	1105(-0.4%)	737(-0.1%)	
Case 2	1231(0.0%)	1112(0.3%)	738(0.0%)	
Case 3	1232(0.08%)	1101(-0.7%)	737(-0.1%)	
Case 4	1230(-0.08%)	1115(0.5%)	739(0.1%)	
Case 5	1233(0.2%)	1098(-1.0%)	737(-0.1%)	
Case 6	1230(-0.08%)	1117(0.7%)	739(0.1%)	
Measurement	-1157	1157	618	4
$[A]_{24x3}$	-1186	1186	532	
Case 1	-1185(-0.08%)	1181(-0.4%)	651(0.2%)	
Case 2	-1187(0.08%)	1190(0.3%)	652(0.0%)	
Case 3	-1185(-0.08%)	1175(-0.9%)	650(-0.3%)	
Case 4	-1187(0.08%)	1195(0.8%)	652(0.0%)	
Case 5	-1185(-0.08%)	1172(-1.2%)	650(-0.3%)	
Case 6	-1188(0.2%)	1197(0.9%)	653(0.2%)	

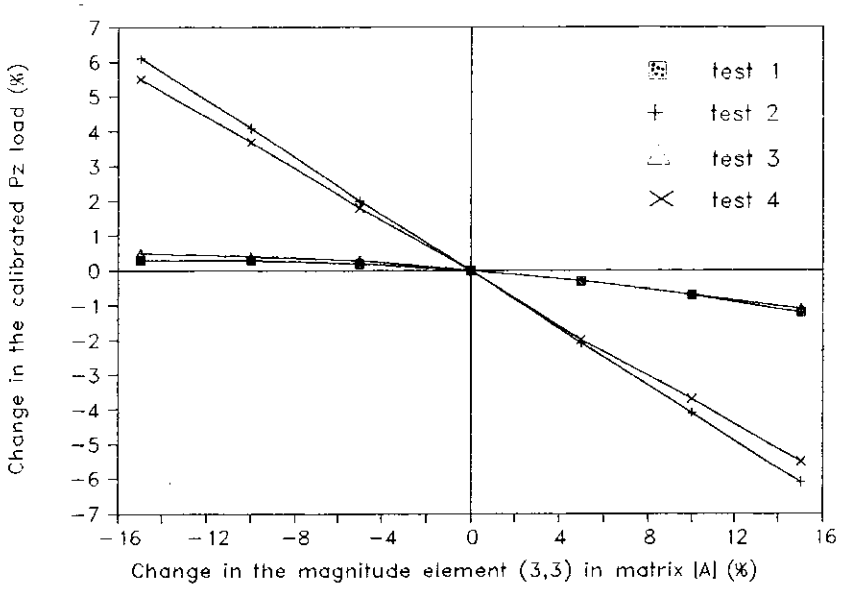

Figure 4.30. Results of the sensitivity study for element (3,3)

directions loads are small (less than 1%) compare to the changes in the Z direction loads (0.2 to 6.1%). The small changes in the calculated loads (less than 1% for X and Y directions loads and less than 6.1% for Z direction loads) indicates that the variation of the internal forces readings during the calibration of the transducer, if any, do not substantially affect the performance of the transducer. Figures 4.30, 4.31, 4.32, 4.33, and 4.34 show that an increment of an element of matrix [A] results a decrement of the calculated loads and a decrement of an element of matrix [A] results an increment of the calculated loads. In Eq. 3-31

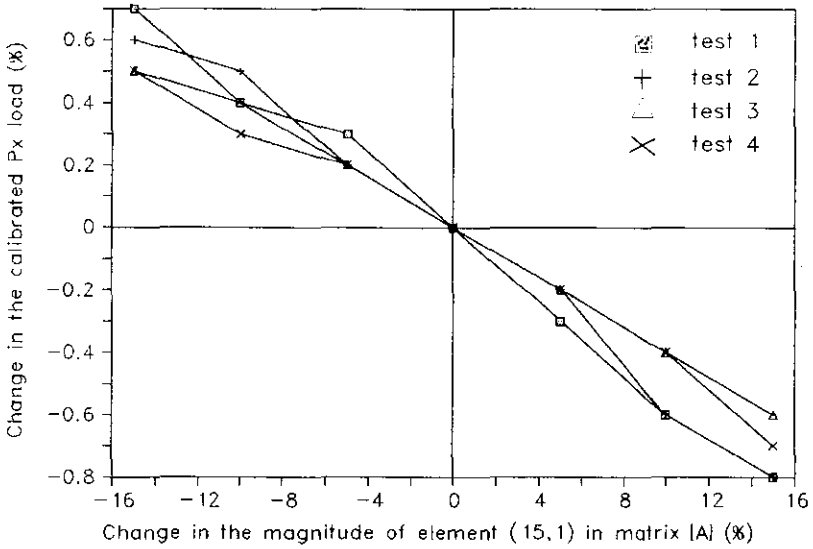

Figure 4.31. Results of the sensitivity study for element (15,1)

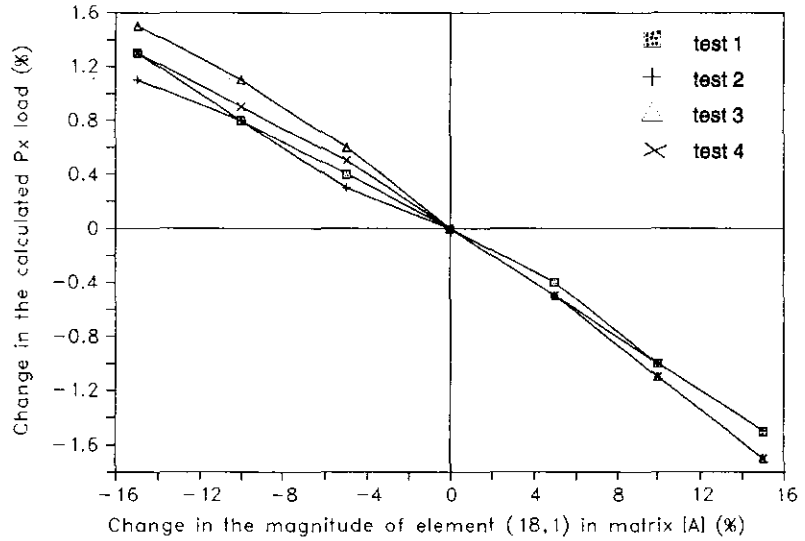

Figure 4.32. Results of the sensitivity study for element (18,1)

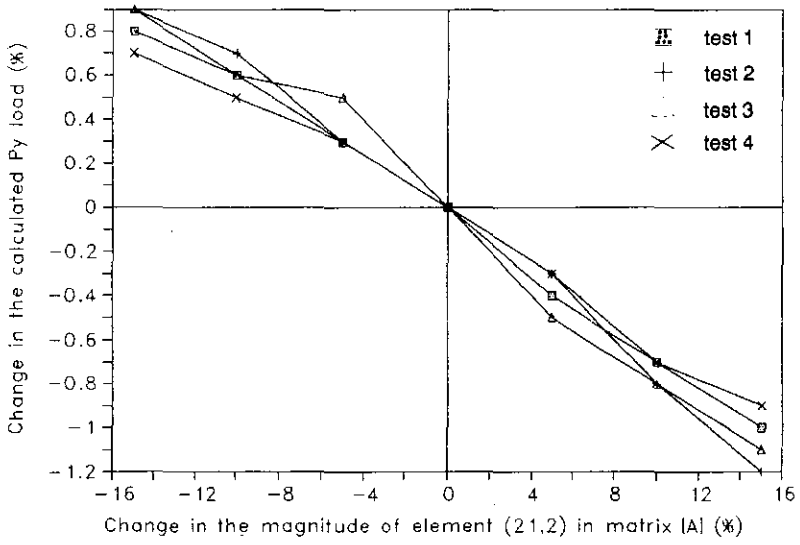

Figure 4.33. Results of the sensitivity study for element (21,2)

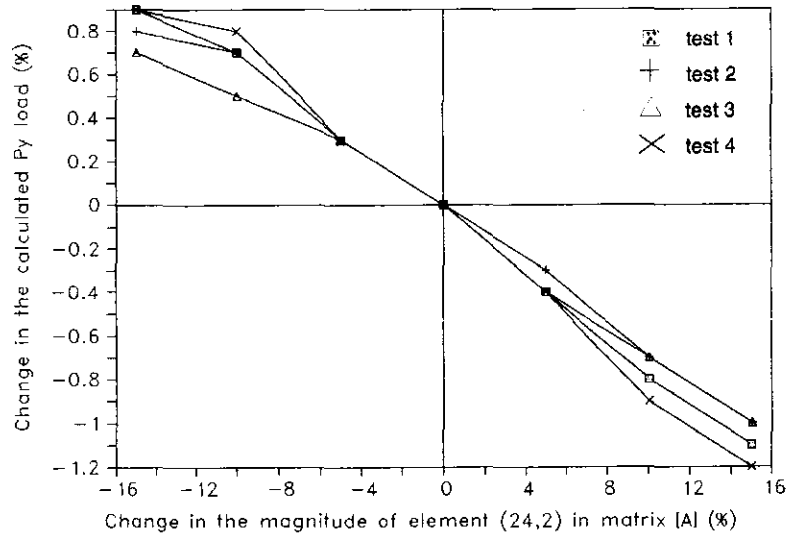

Figure 4.34. Results of the sensitivity study for element (24,2)

the matrix [B] is subtracted from the matrix {U}; and then the results were multiplied by matrix $[A]^{-1}_{3x24}$ to obtain {P}. The coefficients of matrix [B] were smaller (one-tenth or less) than the coefficients of matrix {U}. This means that the effect of variation in element of matrix [B] is negligible.

4.6.6 Error analysis

The percent differences between the measured and the calculated applied loads for all of the combined loading tests were calculated. The measured applied loads were the loads determined from load cell readings, whereas the calculated applied loads were the loads determined by both equilibrium and calibration approaches. Two methods of comparison were used: the absolute value and the algebraic value. A plus sign means an overestimate of a load whereas a minus sign means an underestimate of a load.

Figures 4.35, 4.36, and 4.37 show the plots of the measured applied loads versus the absolute error of the equilibrium and the matrix approaches. The applied loads are the loads in the X, Y, and Z-axis directions. The solid and dotted lines are the linear regression lines of the absolute error from the equilibrium approach and the absolute error from the matrix approach, respectively. The magnitudes of the loads induced by a 60 mph wind on a 350-ft and 500-ft span transmission line are shown also in Figures 4.35 and 4.36 by the arrows. Depending on the orientation of the transducer in

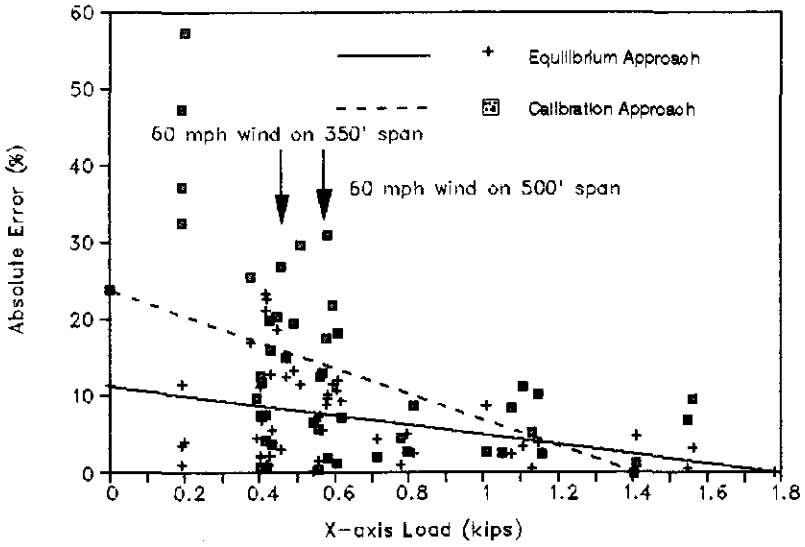

Figure 4.35. Distribution of absolute error for loads in the X-axis direction

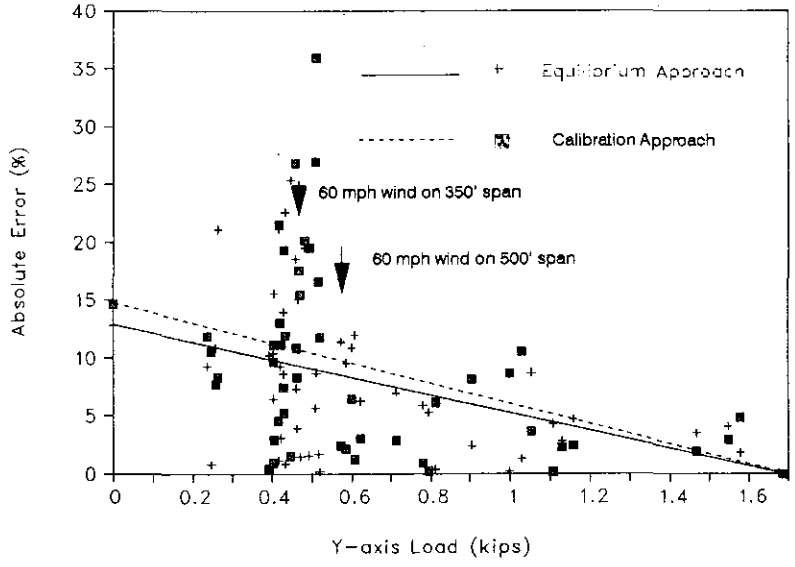

Figure 4.36. Distribution of absolute error for loads in the Y-axis direction

a field application, the wind loads could be in X-axis (longitudinal) or Y-axis (transverse) directions. Therefore, the wind loads are shown in both Figures. 4.35 and 4.36. Most of the applied loads in the tests are equivalentto the magnitude of the load induced by 60 mph wind; therefore, the load induced by 60 mph wind was selected to represent the wind loads. Based on the regression line for the matrix approach, the error obtained for 60-mph-wind load on 500-ft-span transmission line is 13%. This indicates that the transducer provide an accuracy of 87% in measuring the load induced by a 60 mph wind.

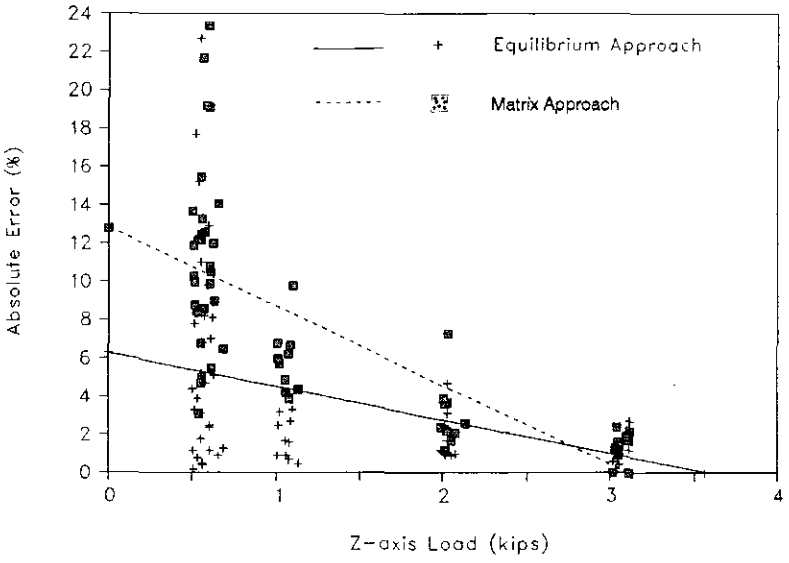

Figure 4.37. Distribution of absolute error for loads in the Z-axis direction

Figures. 4.38, 4.39, and 4.40 show the plot of the measured applied loads versus the algebraic error from the equilibrium and the matrix approaches. The applied loads are the loads in the X, Y, and Z-axis directions. The loads in

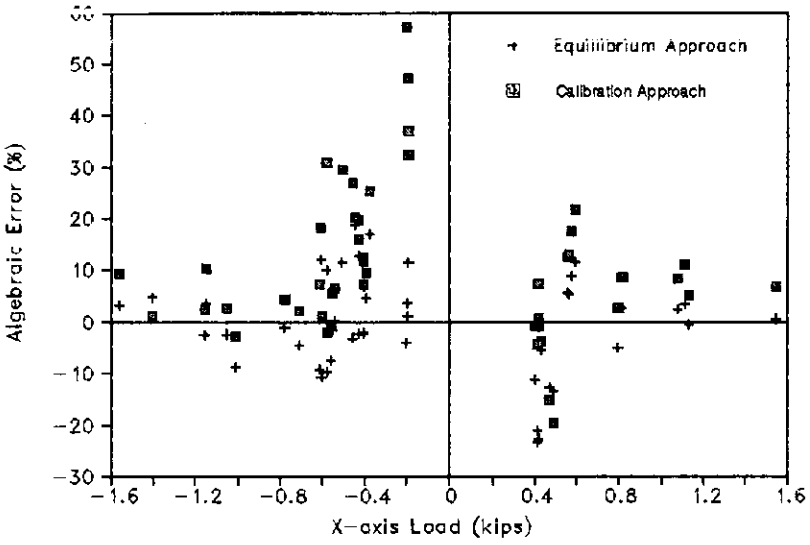

Figure 4.38. Distribution of algebraic error for loads in the X-axis direction

the X-Y plane (horizontal plane) can be applied from either the positive or negative X or Y-axis directions, whereas the loads in the vertical direction are in the positive Z-axis direction (push-down). These figures show

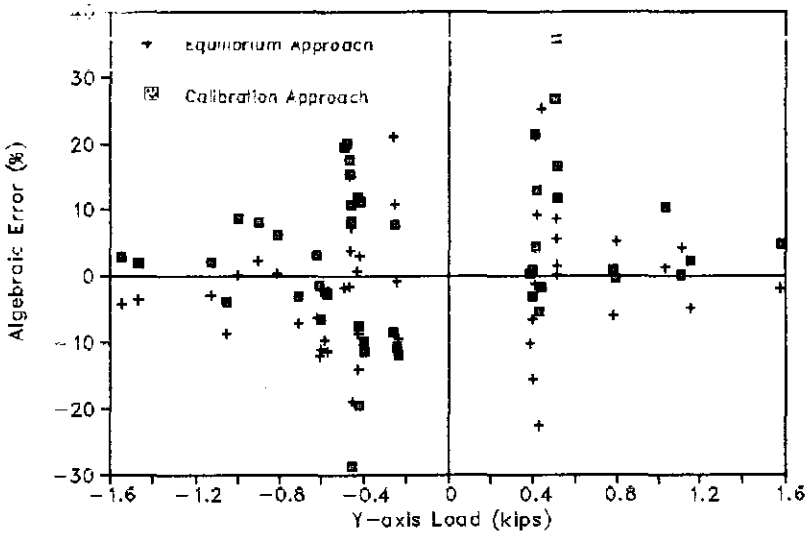

Figure 4.39. Distribution of algebraic error for loads in the Y-axis direction

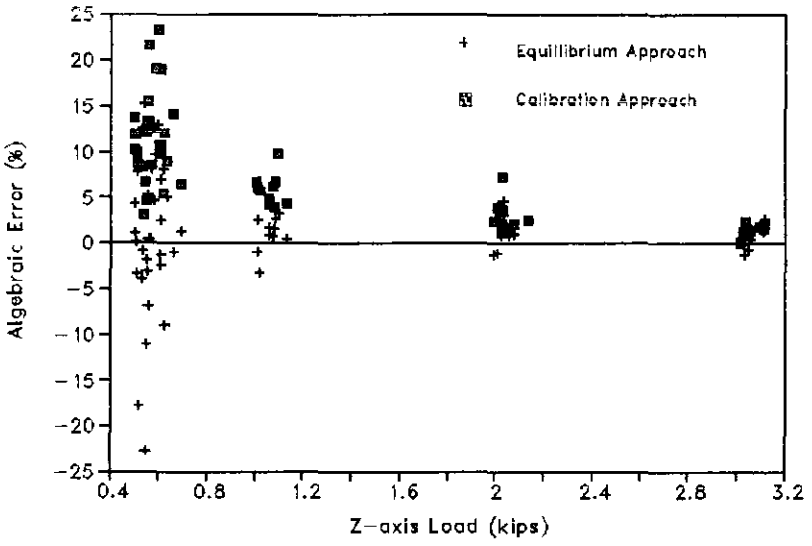

Figure 4.40. Distribution of algebraic error for loads in the Z-axis direction

that the algebraic error decreases for higher loads. For instance, the algebraic error associated with the equilibrium approach of solution for a horizontal load applied in the negative Y-axis direction (Figure 4.39) decreases from about 20% at a 0.3 kips load to about 3% at a 1.6 kips load. Figure 4.38 shows that for horizontal applied loads in the negative X-axis direction, the equilibrium approach has essentially the same probability of underestimating the loads as overestimating the loads, whereas the matrix approach overestimates the loads most of the time.

Figure 4.39 shows that equilibrium approach has essentially the same probability of underestimating the loads as overestimating the loads. Generally, matrix approach overestimates the positive Y-axis direction loads and has essentially the same probability of underestimating as overestimating the negative Y-axis direction loads. Figure 4.40 shows that the matrix approach always overestimates the loads, whereas the equilibrium approach has essentially the same probability of underestimating or overestimating the loads.

Figures 4.41, 4.42, and 4.43 show the plot of data points representing the measured applied loads versus the calculated applied loads by equilibrium and matrix approaches. The applied loads are the loads in the X, Y, and Z-axis directions. The solid line represents the conditions where

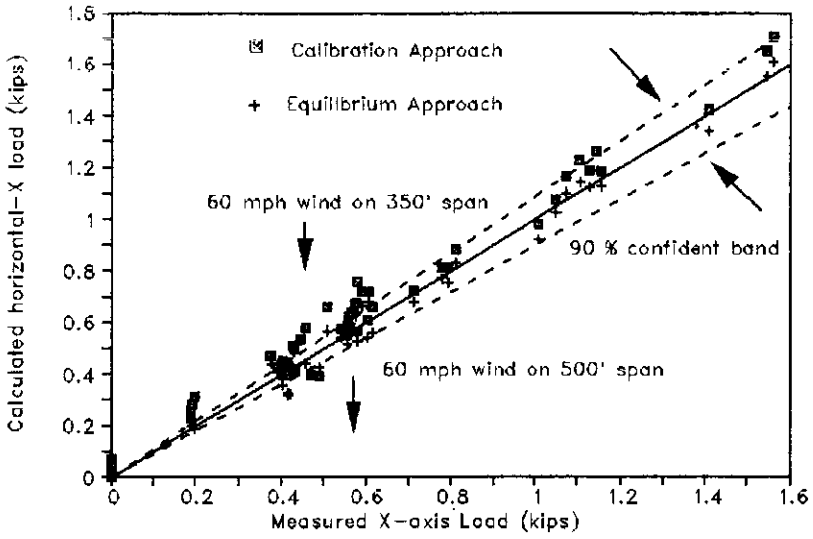

Figure 4.41. Measured versus calculated load in the X-axis direction

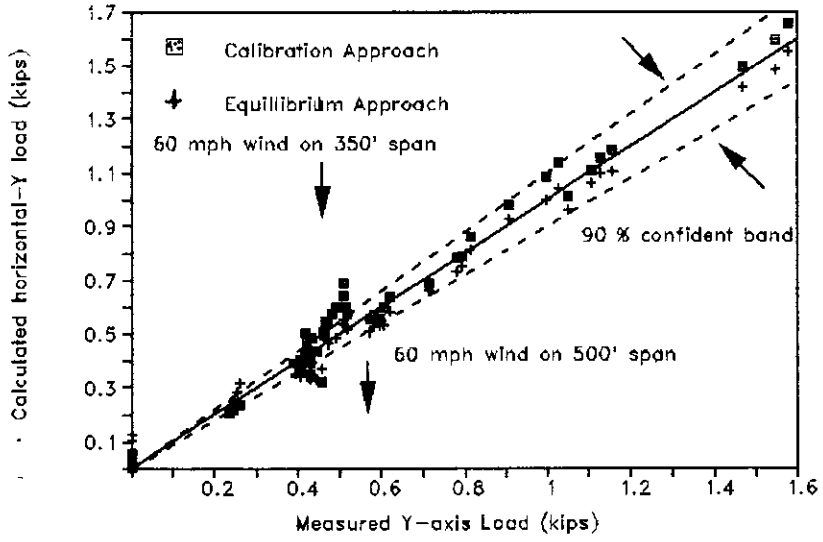

Figure 4.42. Measured versus calculated load in the Y-axis direction

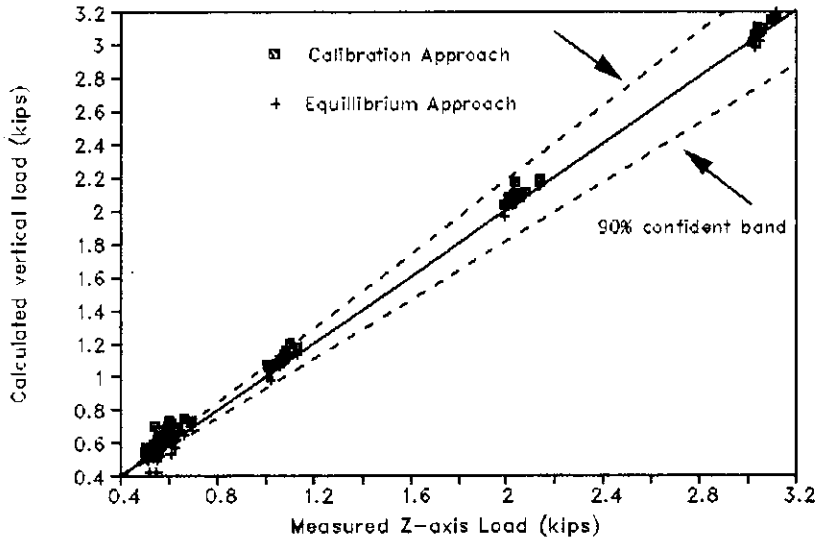

Figure 4.43. Measured versus calculated load in the Z-axis direction

the measured applied loads and the calculated applied loads are the same. The dotted lines define the limits of a 90% confident band. The loads induced by a 60 mph wind on a 350-ft and 500-ft span transmission lines are shown by the vertical arrows in Figures 4.41 and 4.42. These figures show that the equilibrium approach results are within the 90% confident band most of the time, whereas the matrix approach results are essentially within the 90% confidence band for horizontal and vertical loads greater than 0.6 kips and 1 kips, respectively. To improve the accuracy of the transducer for loads smaller than 0.6 kips in the horizontal direction,

smaller diameter horizontal rods should be used.

Figure 4.44 shows the plot of the applied vertical loads versus the calculated vertical loads by the equilibrium and matrix approach. The data in this figure represent the data

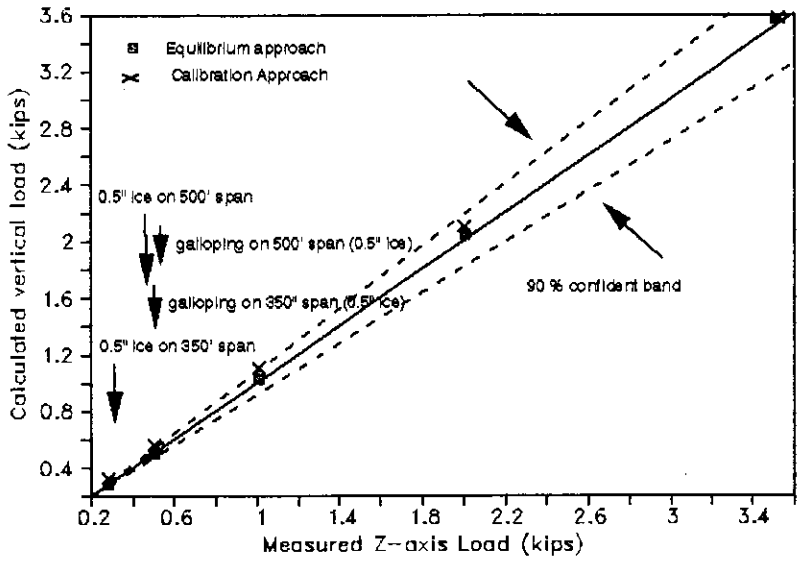

Figure 4.44. Measured versus calculated vertical (only) load

obtained from the test which applied loads are the loads applied in the vertical direction only. The magnitudes of the loads induced by 0.5 in. of radial ice on a 350-ft and a 500-ft span; and galloping on a 350-ft and a 500-ft span with a 10

mph wind and 0.5 in. of radial ice are shown by the arrows. The transverse loads induced by a 10 mph wind on a 350-ft and a 500-ft span are 24 and 33 lbs, respectively, which are small compare to the load induced by galloping. Therefore, only vertical loads were considered in measuring the loads induced by galloping. The figure shows that the accuracy of the transducer in measuring the ice and galloping loads on 500-ft-span transmission line resulted from equilibrium and matrix approach are within the 90% and close to 90% confident band (precisely 86%), respectively. Although the equilibrium approach produces more accurate results, the matrix approach is simpler to apply and still produces reasonable accuracy.

5. SUMMARY, CONCLUSIONS AND RECOMMENDATION

Transmission line damage caused by galloping is not an unusual occurrence in some regions of the United States and Canada. In order to design cost-efficient structures that are strong enough to resist typical galloping forces, one needs to know the magnitude of the forces involved. The results of the survey conducted in this research and the lack of the published information on transmission line instrumentation indicates more research addressing the forces acting on the transmission lines is needed. This study was devoted to designing an instrumentation device that would measure the forces acting on transmission line structures. Although the main purpose was to measure the forces induced by galloping, the concepts for the device developed in this work can be applied to measure other forces such as wind and ice forces. The transducer was initially designed to be mounted on transmission lines with post-type insulators. However, the transducer can be used on transmission lines with suspension-type insulators as well.

The transducer developed was intended to be used on a 500-ft span transmission lines. The transducer consists of two aluminum plates and eights aluminum rods: Four vertical rods and four horizontal rods. For the uniformity, the same diameter was used for the horizontal and vertical rods. The rods were connected to the plates by nuts. Electrical

resistance strain gages were used to establish the forces acting on the transducer. Each rod contained 12 strain gages: 8 strain gages in quarter-bridge configurations for establishing rod shear forces and 4 strain gages in full-bridge configurations for establishing rod axial forces.

An important point learned during this research was that the tightness of the connection between the rods and the plates can effect the performance of the transducer. If the connections are not tight enough, the response of the transducer would not be constant for repeated loads. To produce the tightness needed, the nuts were initially tighten by an ordinary wrench. The final tightness was accomplished by using a calibrated torque wrench. All nuts were tightened to a torque of 35 ft-lbs.

Three approaches can be used in establishing the loads acting on the transducer; the equilibrium approach, the calibration matrix $[A]_{8x3}$ approach which does not include the rod shear forces, and the calibration matrix $[A]_{24x3}$ approach which includes the rod shear forces. The calibration matrices $[A]_{8x3}$ and $[A]_{24x3}$ produce essentially identical results. Therefore, if a calibration matrix approach is to be used, only the axial forces in the rods need to be measured. Comparing the results associated with the equilibrium and calibration matrix $[A]_{8x3}$ approaches, the former method generally produces better accuracy, but the later is simpler

to apply and still produces reasonable accuracy. The calibration matrix $[A]_{8x3}$ requires fewer strain gages than are needed with the equilibrium approach. Thus, the transducer is easier to develop. Also, with fewer strain gages, less data would have to be recorded in field applications and fewer computations would be needed in analyzing the recorded data. Therefore, the approach involving the calibration matrix $[A]_{8x3}$ is recommended to be used in future research.

The sensitivity study of matrix $[A]_{24x3}$ indicated that small variations of the magnitude of an element of matrix $[A]_{24x3}$ does not substantially affect the performance of the transducer. The results of the experimental tests showed that the prototype transducer will be capable of monitoring the loads induced by the wind with the speed of 60-mph or higher, galloping, and ice. To measure the forces induced by lower-speed wind more accurately, smaller diameter horizontal rods should be used. Based on the regression line of the matrix approach, the error obtained for 60-mph-wind load on 500-ft-span transmission line is 13%. This indicates that the transducer provide an accuracy of 87% in measuring the load induced by 60 mph wind. The accuracy of the transducer in measuring the 0.5 in. of radial ice and galloping under 10 mph wind loads is 86% or more. The accuracy of the transducer increases for larger loads.

The loads to be resisted and measured on transmission lines with spans less than 500 ft are smaller than the loads on longer span transmission lines. Therefore, smaller diameter aluminum rods should be used when a transducer is to be mounted on transmission lines with spans less than 500 ft. With smaller diameter rods, the transducer will produce better accuracy for small loads, and it will still maintain the structural safety needed.

For transmission lines with spans greater than 500 ft., the diameter of the aluminum rods should be increased to provide the required structural safety of the transmission lines. With larger diameter aluminum rods, the transducer will become less sensitive to small loads. However, the loads to be measured on the larger spans are also larger; therefore, the transducer will produce the accuracy needed.

Several improvements in assembling and testing the transducer should be considered for future research on this measurement device. Several tabs for the quarter-bridge strain gages were broken by accidentally pulling on the lead wires. There are two ways to minimize this type of instrumentation failure: Use strain gages with a larger tab area and reverse the position of the strain gages (see Fig. 5.1). A larger tab area will have a stronger attachment between the tab and the strain gages. With the suggested positions of the strain gages as shown in Fig. 5.1b, the

attachment of the wires to the rod are stronger than the attachment of the wires to the rod in Fig. 5.1a. To avoid accidentally pulling on the wires, the transducer should not be moved during the test. Therefore, a test frame should be built to enable the loads to be applied from all directions.

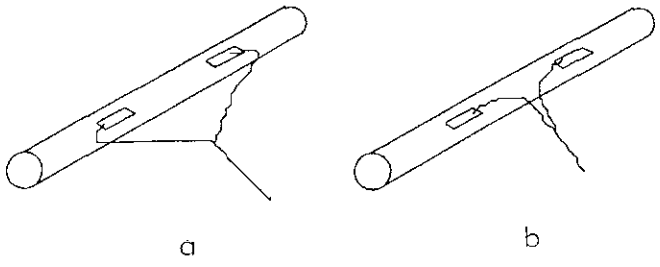

Figure 5.1. Positions for quarter-bridge strain gages

The measurements of conductor ice, wind, and galloping loads in the field are planned to be conducted in the future. With these measurements a computer system will be placed in the field and will record the data. The program to be used on the computer should be able to record the static loads, such as ice weight, and dynamic loads, such as galloping. The frequency of the strain gage readings for the dynamic loads should be more than the frequency of the readings for static loads. Therefore, the program to be used to monitor the instrumentation should be able to detect the occurrence of galloping so that the frequency of the readings can be

increased during the occurrence of galloping. Besides the measurements of the loads, the movements of the conductors during the occurrence of galloping should be videotaped as well.

REFERENCES

1. EPRI. Transmission Line Reference Book. EPRI, Palo Alto, California, 1979.

2. R. N. Dubey and C. Sahay. "Vibration of Overhead Transmission Lines III." Shock & Vibration Digest vol. 12 no. 12 (Dec. 1980): 11-14.

3. J. P. Denhartog. "Transmission Line Vibration Due to Sleet." AIEE Transactions vol. 51 (1932): 1074-1076.

4. O. Nigol and G.J. Clark. "Conductor Galloping and Control Based on Torsional Mechanism." IEEE Conference Paper C74016-2 (Feb. 1974).

5. M. A. Baenziger, W. James, B. Wouters, and L. Li. "Dynamic Loads on Transmission Line Structures Due to Galloping Conductors." Engineering Research Institute, Iowa State University, Ames, Iowa, (August) 1990.

6. L. Li. "Dynamics Loads on Pole Transmission Line Structures from Galloping Conductors." Masters Thesis, Iowa State University, Ames, Iowa, 1990.

7. H. M. Irvine. Cable Structures. The MIT Press, Cambridge, Mass., 1981.

8. C.B. Rawlins. "Analysis of Conductor Galloping Field Observation - Single Conductor." IEEE Transactions on Power Apparatus and Systems vol. PAS-100 no. 8 (Aug. 1981): 3744-3753.

9. J. Kortschinski. "Line Ice Detectors for the Indication and Study of Conductor Galloping." IEEE Conference Paper C6867PWR (Feb. 1968).

10. S. Krishnasamy. "Wind and Ice Loads on Overhead Transmission Lines." Ontario Hydro Research Review vol. 3 (June 1981): 11-18.

11. A. Akhtar. " A Monitoring System for the Mechanical Safety of Remote Transmission Lines." Fall Meeting of the Canadian Electrical Association (Transmission). Winnipeg, Manitoba, Sept. 1980.

12. N. Streat, and N.W. Brodie. "Triaxial Load Cells for Monitoring Overhead Transmission Lines." Experimental Techniques (Nov. 1984): 27-29.

13. M. L. Jacobs, and G.A. Vaselaar. "A ground based sensor for the detection of transmission line conductor motion. "IEEE Transactions on Power Delivery vol.5 no.2 (April 1990): (1170-1174).

14. M. A. Baenziger. "Cable: A Program for Dynamics Loads on Pole Transmission Line Structures from Galloping Conductors." [Computer program] Iowa State University, Ames, Iowa.

15. ASCE. Guidelines for Electrical Transmission Line Structural Loading. ASCE, New York, 1991.

16. ANSI and IEEE. National Electrical Safety Codes. ANSI and IEEE, New York, 1981.

17. ASCE. Design of Steel Transmission Pole Structures. 2nd ed., ASCE, New York, 1990.

18. Aluminum Company of America. Alcoa Aluminum Handbook. Aluminum Company of America, Pittsburgh, Pennsylvania, 1957.

19. A. Bazergui, N.E. Eryuzlu, and J.P. Saucet. "A Submersible 3-d Load Transducer Platform." Experimental Techniques (Sept. 1987): 25-28.

20. J. W. Dally and W. F. Riley. Experimental Stress Analysis. 2nd ed., Mcgraw-Hill, New York, 1978.

21. G. J. Desalvo and J. A. Swanson. Ansys Engineering Analysis System User's Manual. Swanson Analysis Systems, Inc, Houston, Pennsylvania, 1985.

22. S. A. Ridlon. "Modeling Guidelines." In Finite Element Idealization, Ed. C. Meyer. ASCE, New York, 1987. 212-272

23. Y. Rocard. General Dynamics of Vibrations. Frederick Ungar Publishing Co., New York, 1960.

24. R.D. Adams. "The Damping Characteristics of Certain Steels, Cast Irons and Other Metals." Journal of Sound and Vibration (July 1972): 199-216

25. F. A. Graybill. Matrices with Applications in Statistics. Wadsworth International Group, Belmont, California, 1983.

26. The Aluminum Association. Aluminum Standards and Data 1990. The Aluminum Association, Inc., Washington, D.C., 1990.

ACKNOWLEDGEMENTS

I would like to express my sincere gratitude to Dr. Robert E. Abendroth and Dr. Mardith A. Baenziger, my co-major professors, for their guidance and supervision in this research. They also contributed a great deal to the completion of this thesis.

I would like to thank Dr. Loren Zachary for his participation as a member of my graduate committees and his helpful suggestions.

I also would like to thank the EPRC, Electric Power Research Center of Iowa State University for sponsoring this research.

I would like to dedicate this thesis to my parents: Liem Tjeng Kie and Go Lian Moei.

APPENDIX A. QUESTIONNAIRE

Questionnaire on Transmission Line Behavior

Department of Civil Engineering
Iowa State University, Ames, IA 50011

Company/Utility Name: _____
Address: _____
Contact Person: _____ Phone: _____

1. Mechanical Damage since 1980 caused by wind, ice, galloping, thermal or other. Please fill in the blanks of the following table using a scale of: 0 to never, 1 for few, 2 for several, 3 for many.

	Wind	Ice	Galloping	Thermal	Other
Number of Events					
Failure of:					
Conductor(s)					
Conductor connection(s) to insulator					
Post insulator(s)					
Suspension insulator(s)					
Insulator connection(s) to support					
Support arm(s)					
Wood pole					
Steel pole					
Wood H-frame					
Steel H-frame					
Lattice structure					
Y-type structure					
Multiple towers					
Other: _____					

2. How did you monitor the movement of the conductors:
(Please check more than one answer if appropriate)
____Physical observation by citizens
____Physical observation by utility personnel
____Automatic data acquisition at the site
____Monitoring of conductor movements was not performed
____Other: _____

3. Instrumentation of lines since 1980
Please mark your answer(s) with an (X) where appropriate and fill in the blank where indicated.

Parameters Measured (Include attempts to measure even if not successful)	Voltage Level(s) (kv)	Structure Type							Insulator Type			Span Length		
		Wood Pole	Steel Pole	Wood H Frame	Steel H Frame	Lattice	Y-Type	Other ___	Post	Suspension	Other ___	< 250 ft	250 to 500 ft	> 500 ft
Wind speed	___													
Temperature	___													
Ice thickness	___													
Ice shape profile	___													
Insulator swing angle(s)	___													
Vertical force	___													
Force parallel to line	___													
Force perpendicular to line	___													
Amplitude of galloping	___													
Frequency of galloping	___													
Duration of galloping	___													
Other:_____	___													

If you have monitored your line(s) for any of parameters listed in Question #3 would you be willing to share your experience with us? ___ Yes ___ No
If you answered yes, we will be contacting you for additional information.

4. Do you want us to send you the results of this survey? ___ Yes ___ No

Please feel free to write any additional comments which you believe are appropriate on the reverse side of this sheet.

Please return this questionnaire by August 15, 1991.

APPENDIX B. TRANSDUCER DRAWINGS

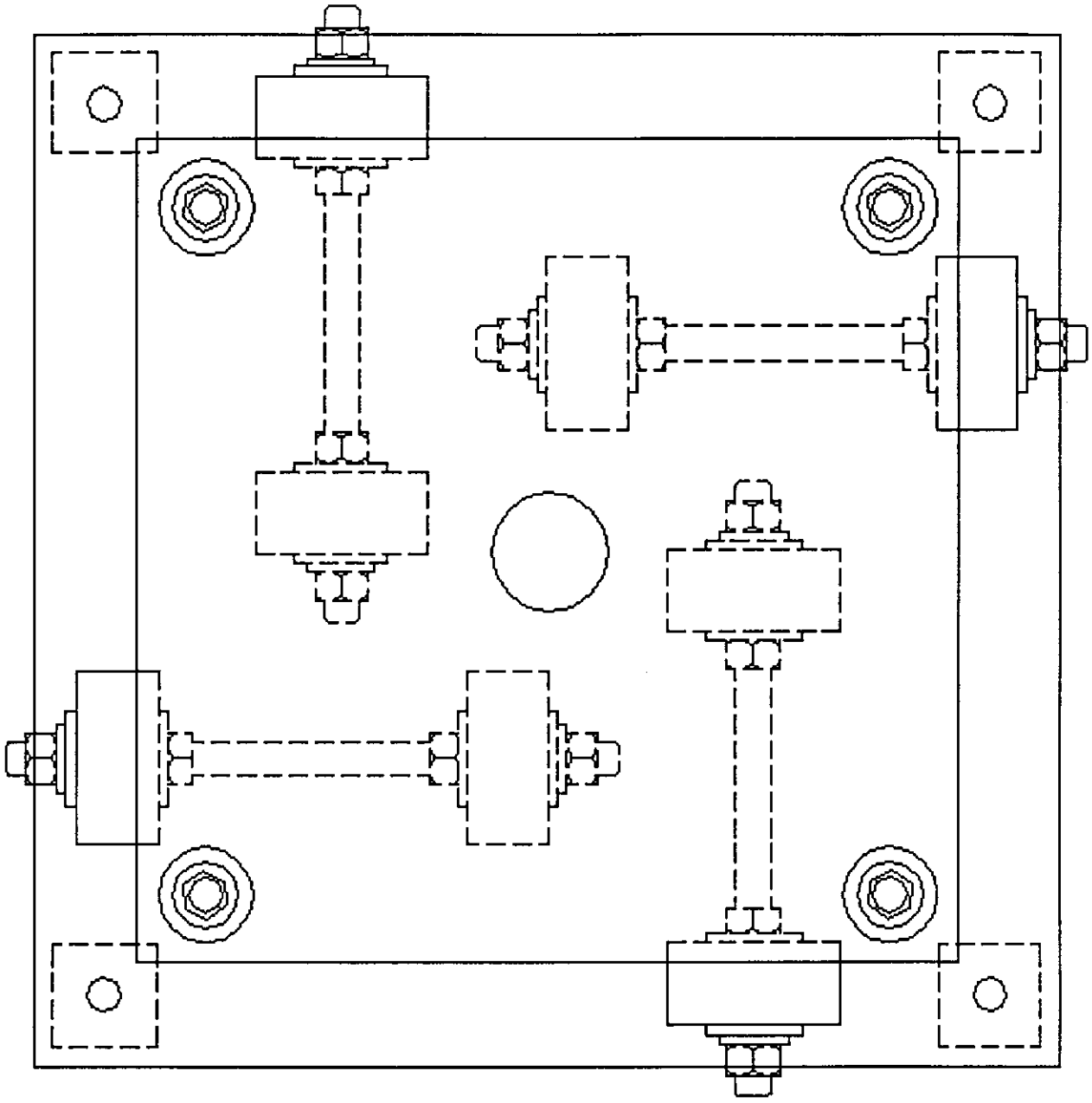

Figure B.1. Plan view of the transducer

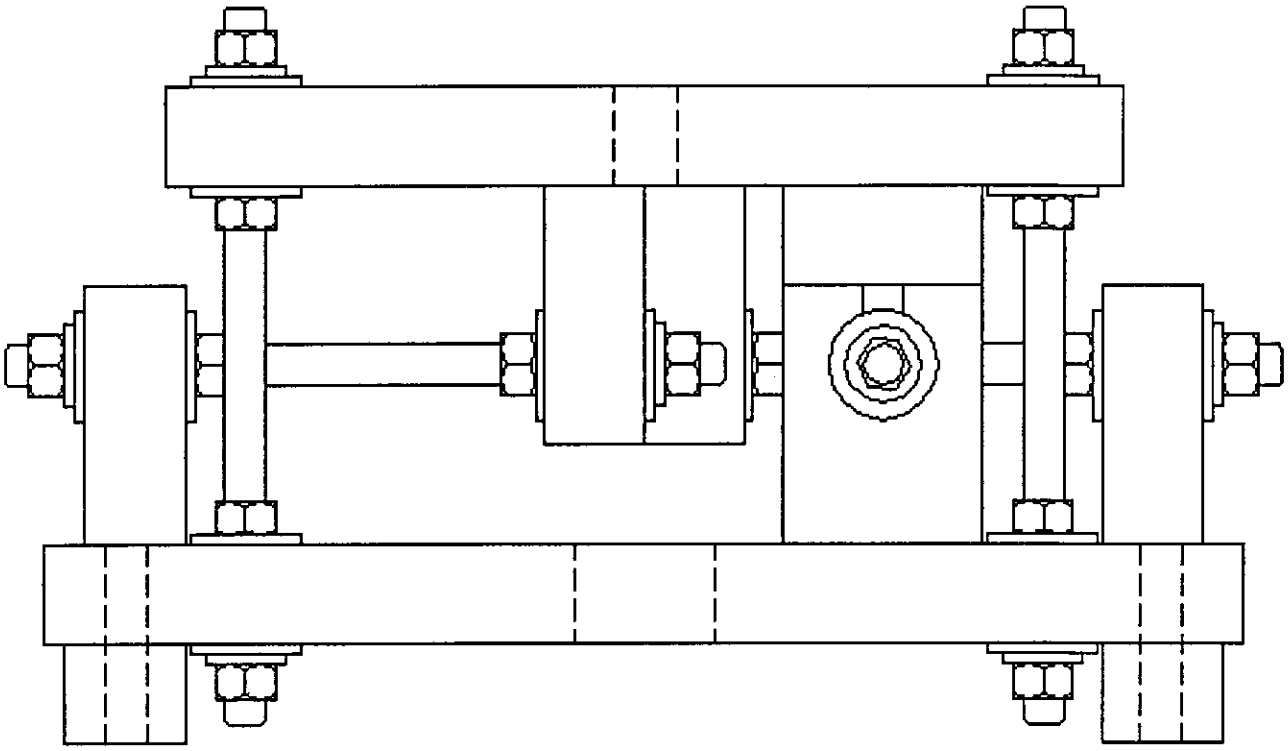

Figure B.1. Plan view of the transducer

APPENDIX C. CALIBRATION CURVES

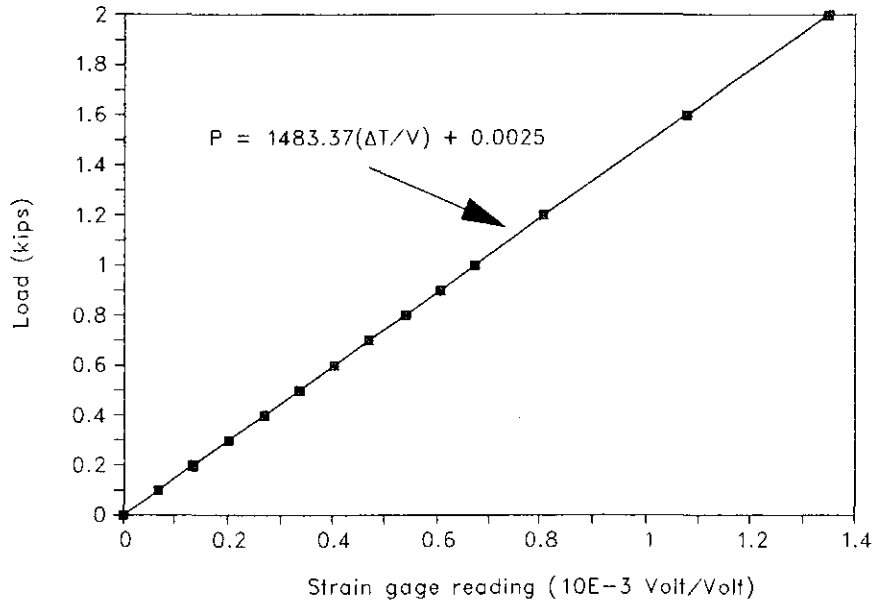

Figure C.1. Regression Line for Rod no. 2

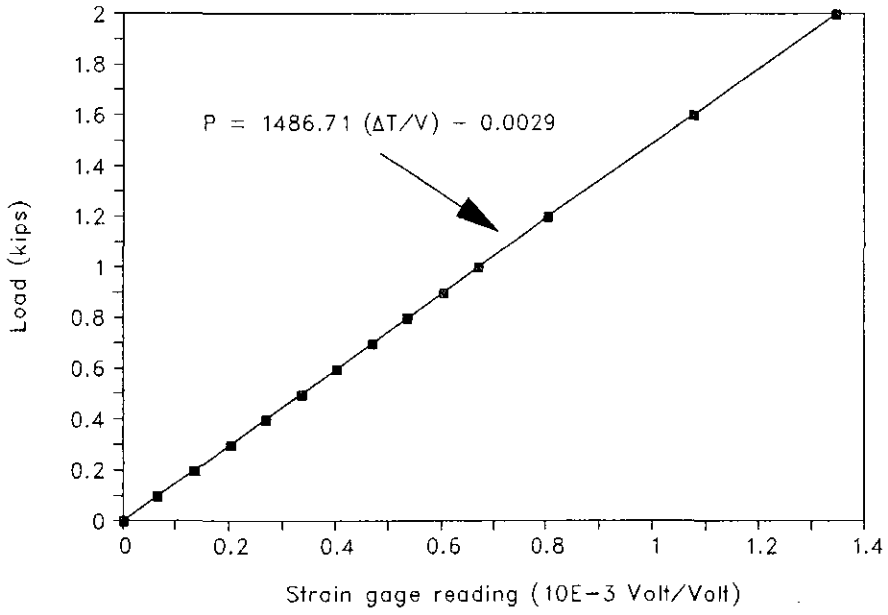

Figure C.2. Regreession line for rod no. 3

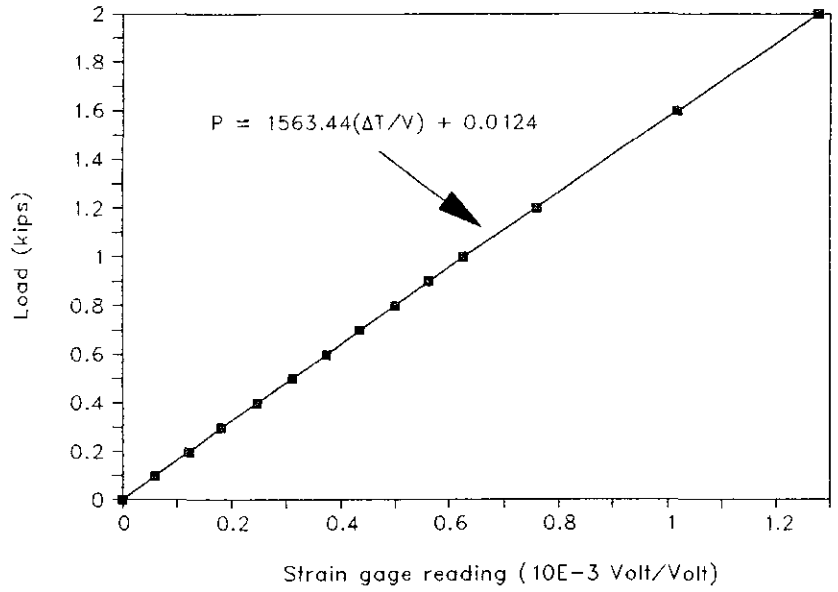

Figure C.3. Regression line for rod no. 4

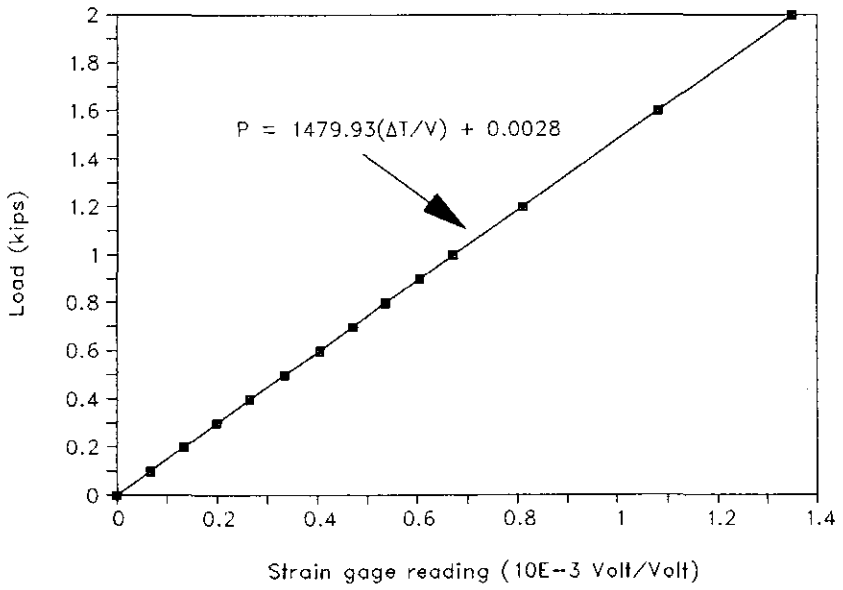

Figure C.4. Regression line for rod no. 5

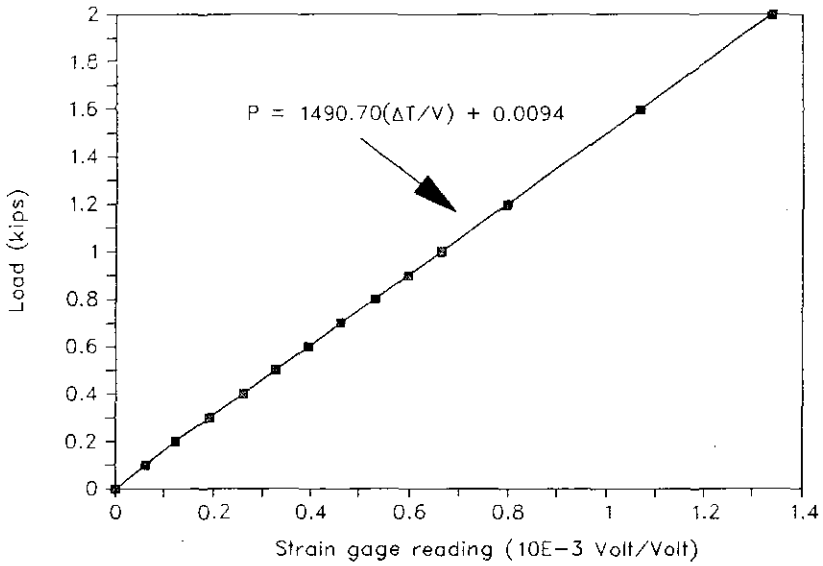

Figure C.5. Regression line for rod no. 6

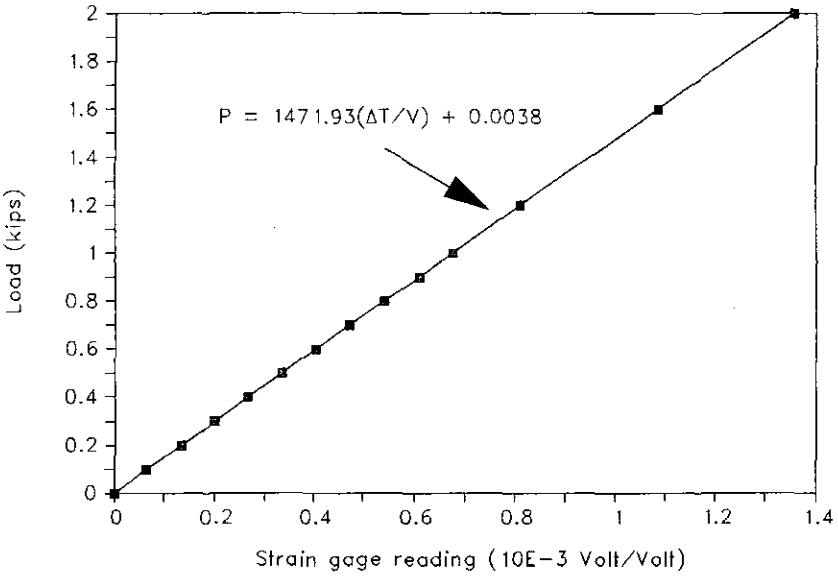

Figure C.6. Regression line for rod no. 7

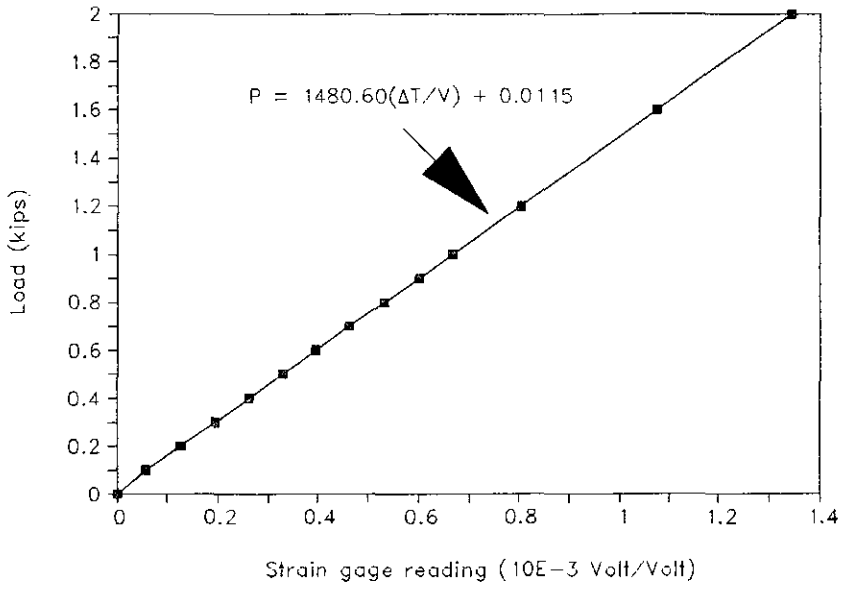

Figure C.7. Regression line for rod no. 8

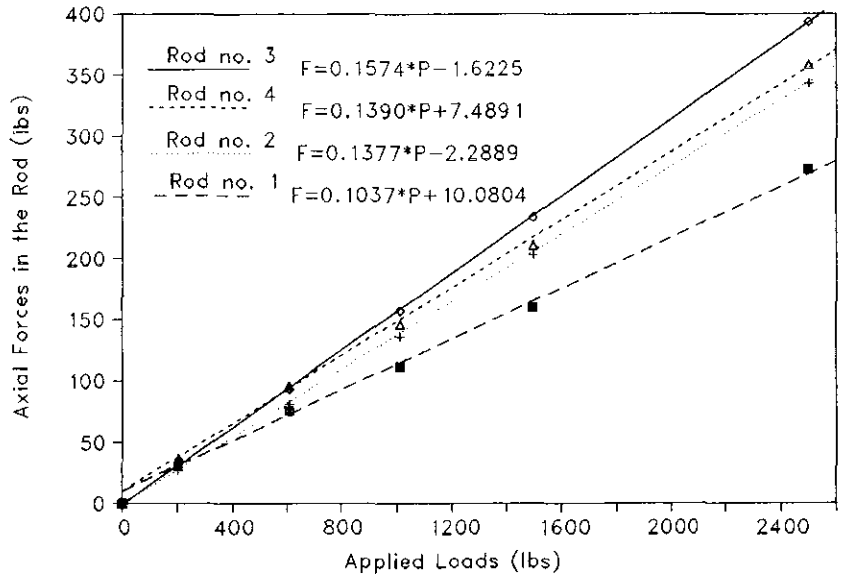

Figure C.8. Calibration curves for the positive X−axis direction (without insulator)

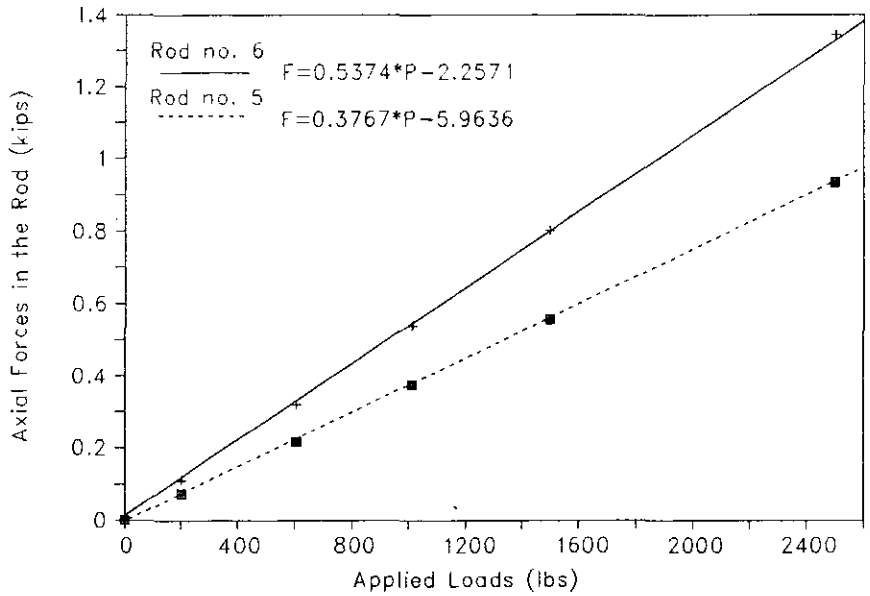

Figure C.9. Calibration curves for the positive X-axis direction (without insulator)

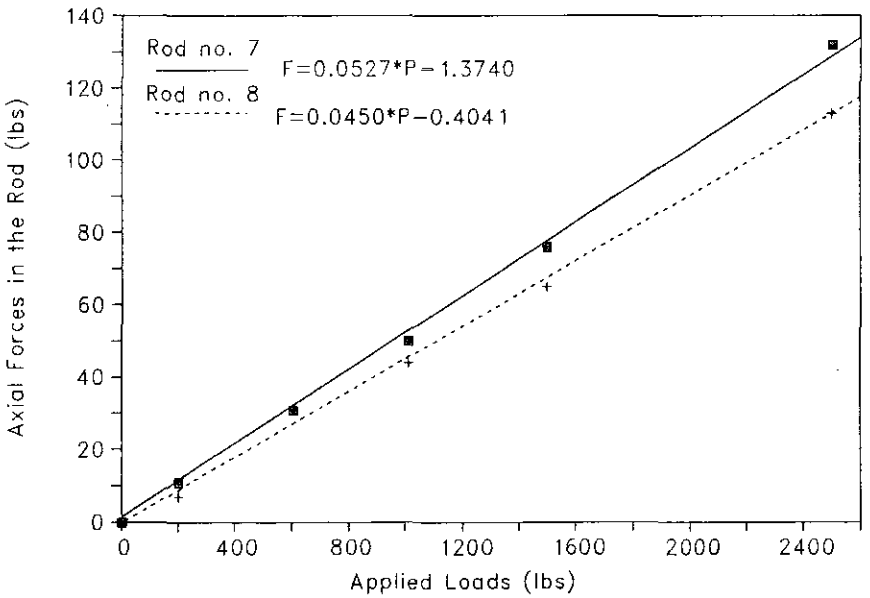

Figure C.10. Calibration curves for the positive X-axis direction (without insulator)

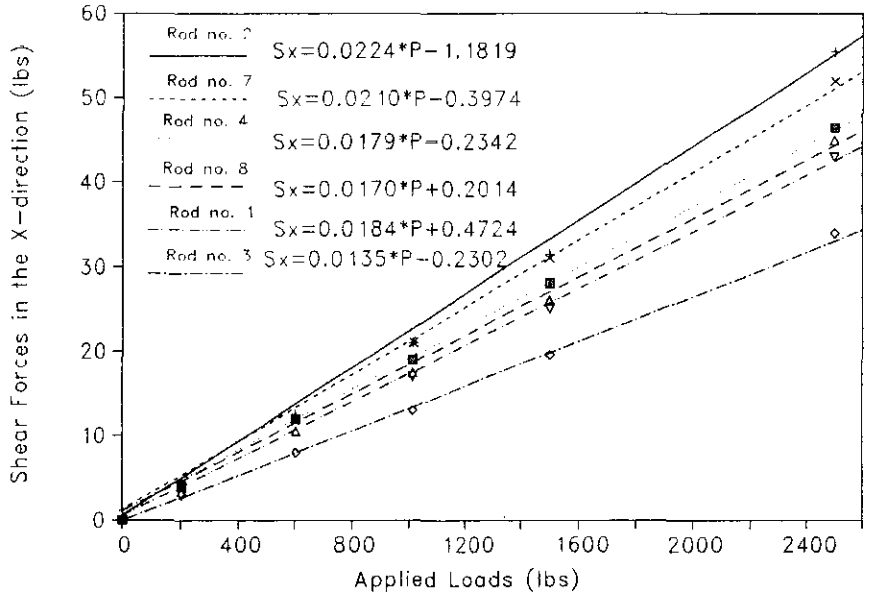

Figure C.11. Calibration curves for the positive X-axis direction (without insulator)

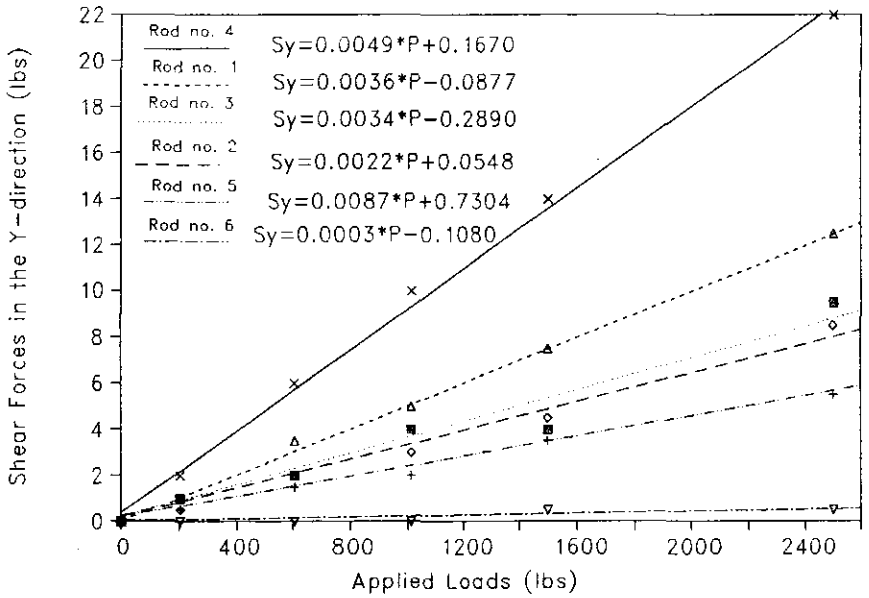

Figure C.12. Calibration curves for the positive X-axis direction (without insulator)

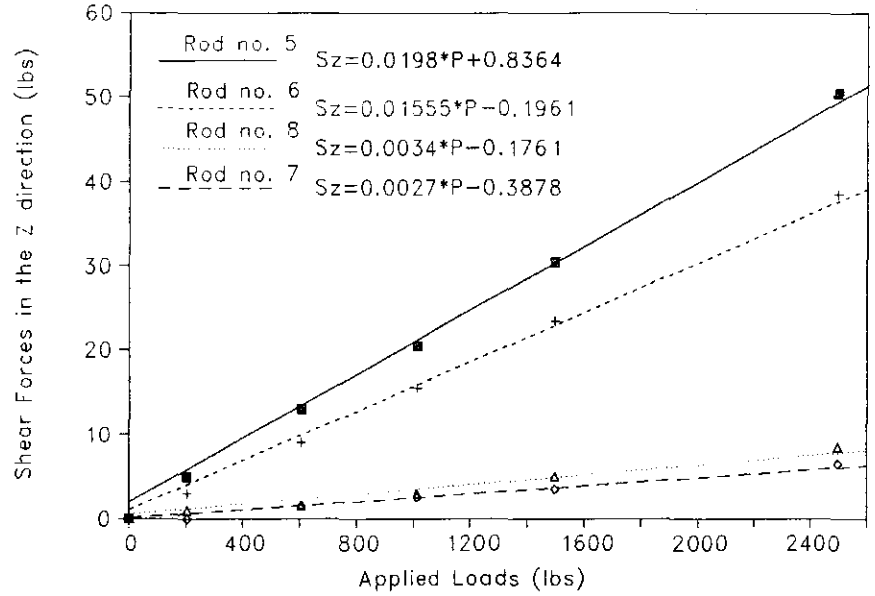

Figure C.13. Calibration curves for the positive X-axis direction (without insulator)

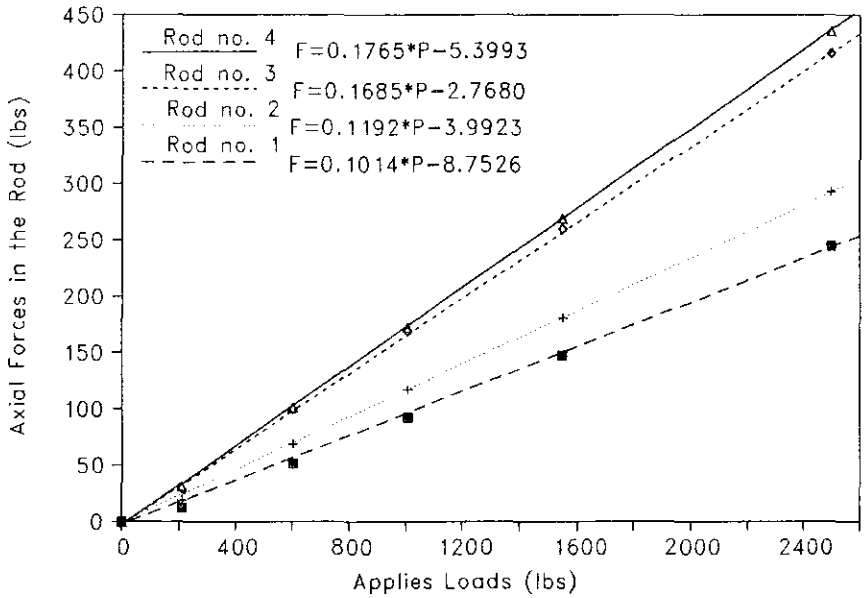

Figure C.14. Calibration curves for the negative X-axis direction (without insulator)

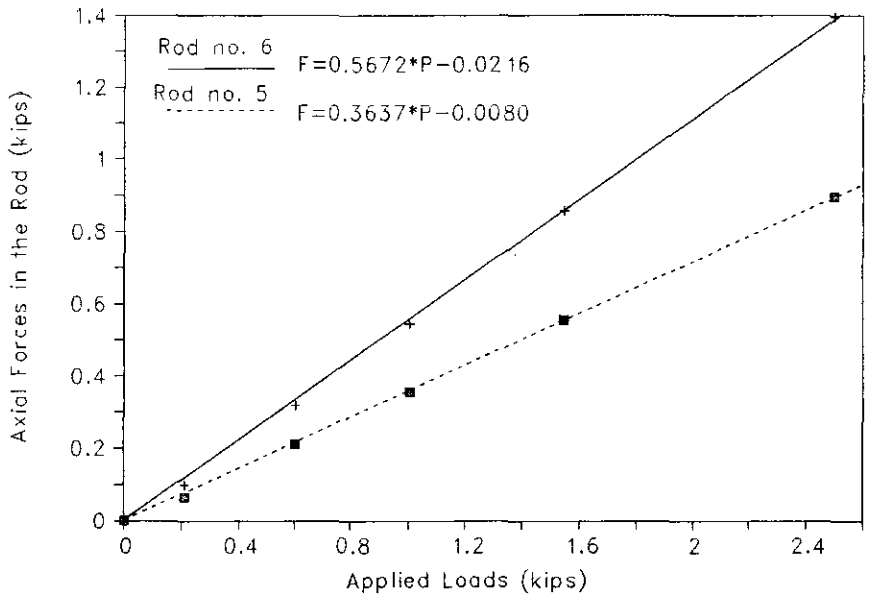

Figure C.15. Calibration curves for the negative X-axis direction (without insulator)

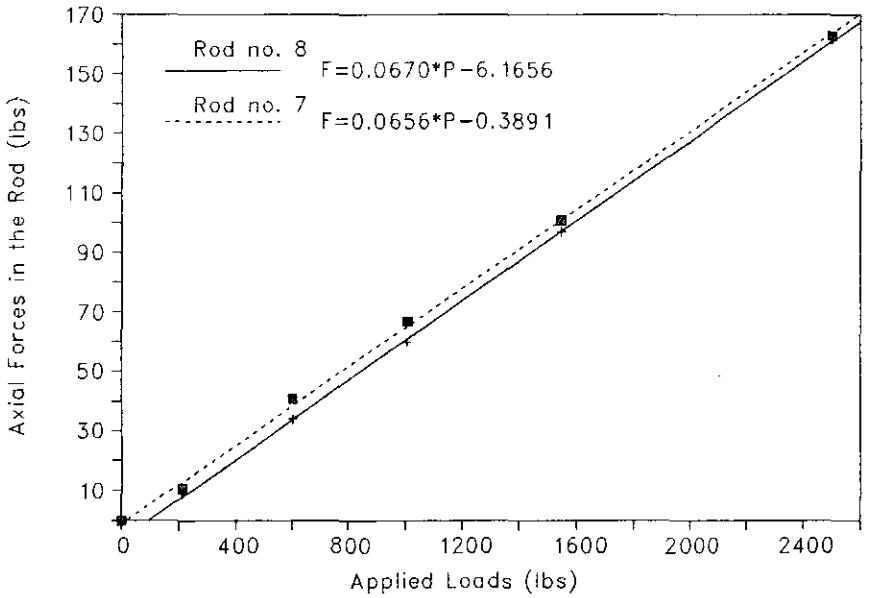

Figure C.16. Calibration curves for the negative X-axis direction (without insulator)

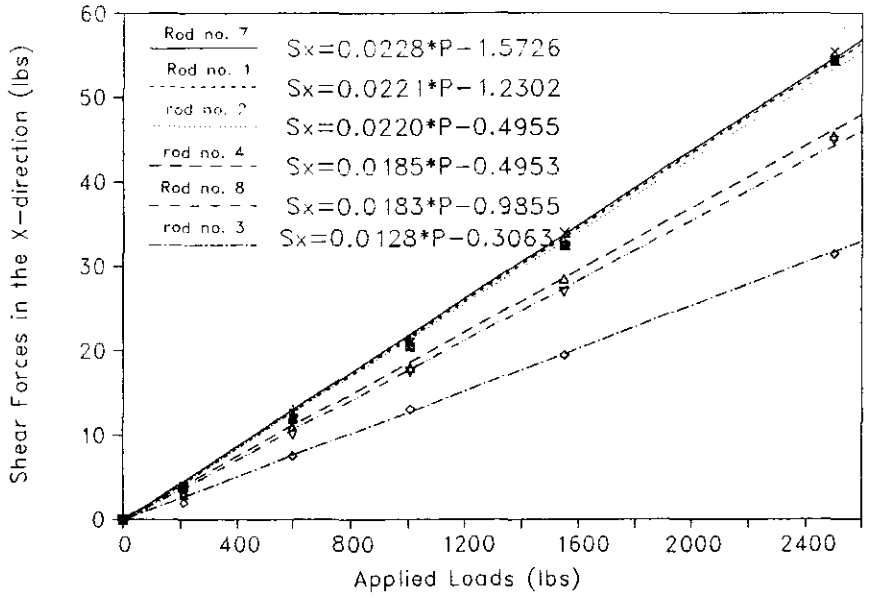

Figure C.17. Calibration curves for the negative X-axis direction (without insulator)

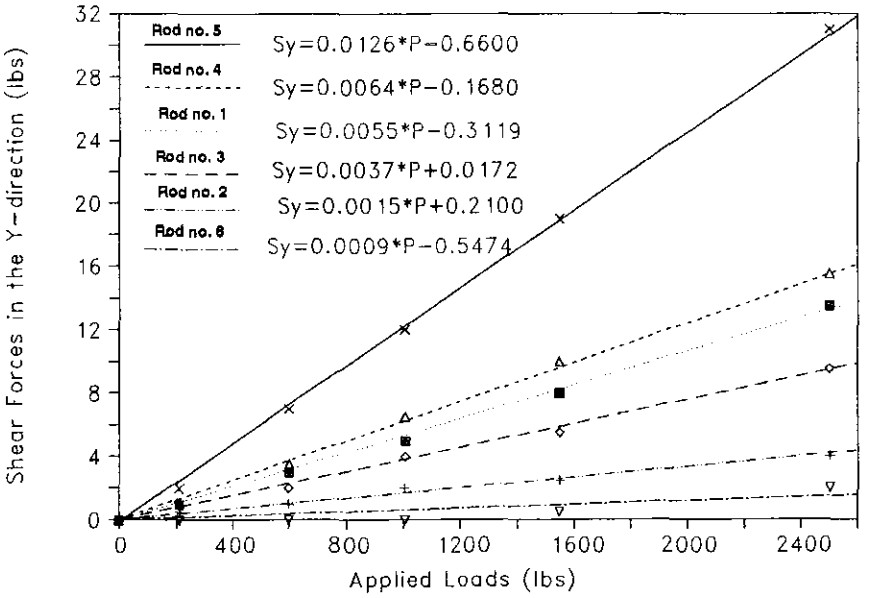

Figure C.18. Calibration curves for the negative X-axis direction (without insulator)

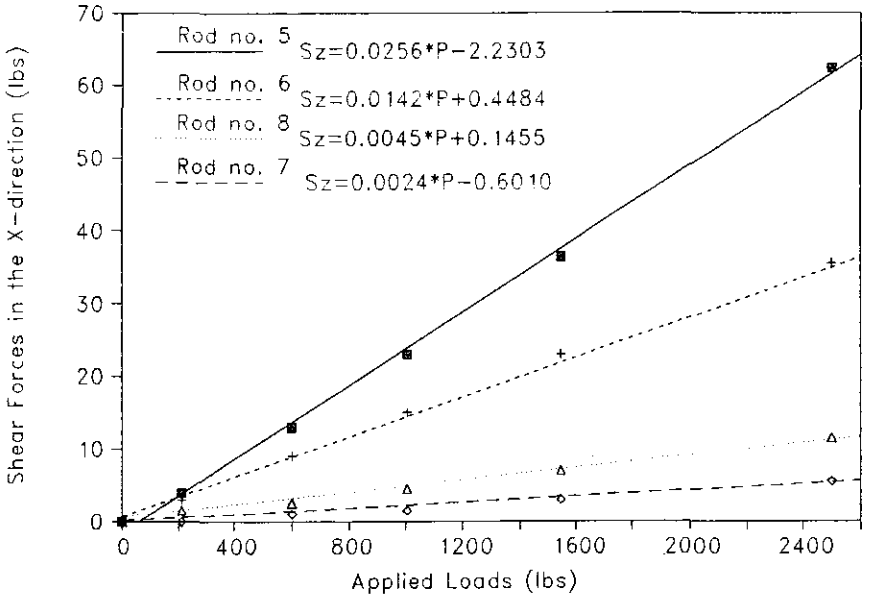

Figure C.19. Calibration curves for the negative X-axis direction (without insulator)

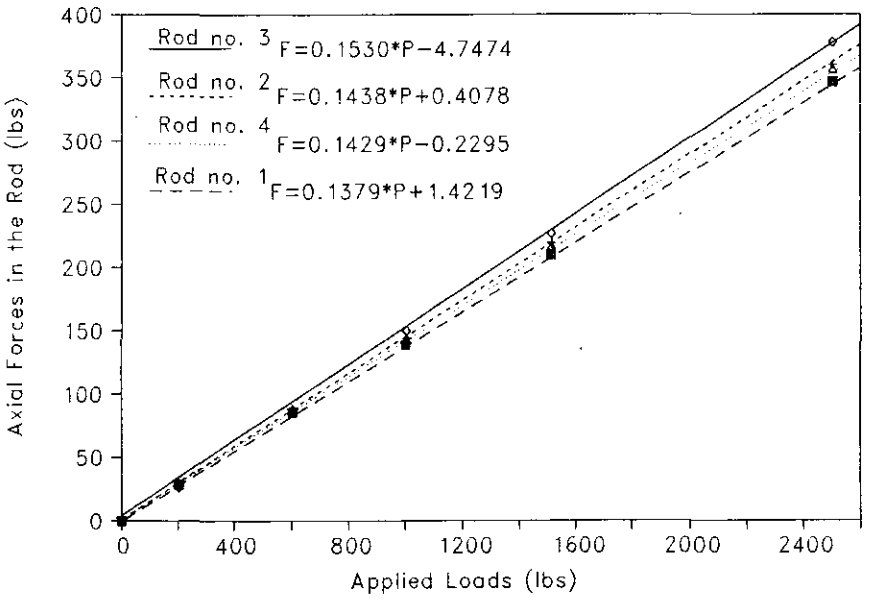

Figure C.20. Calibration curves for the positive Y-axis direction (without insulator)

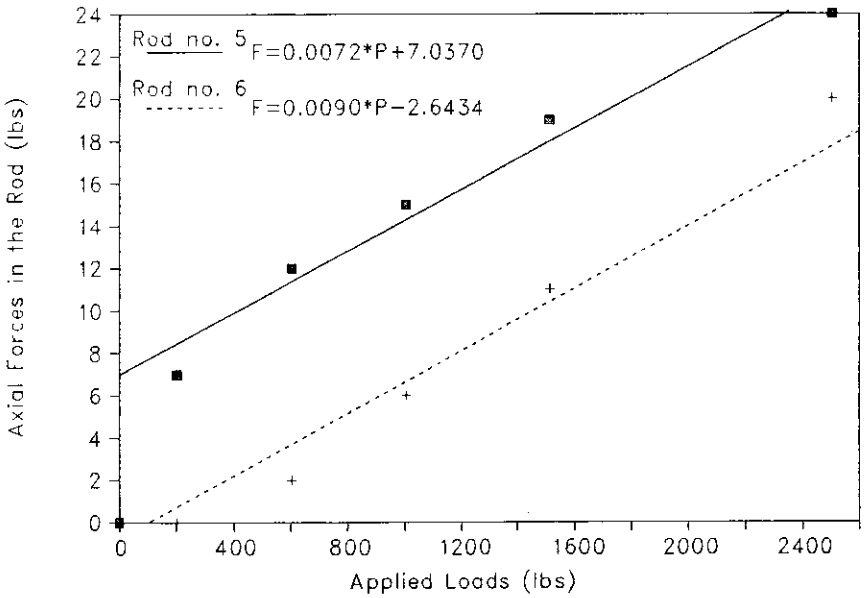

Figure C.21. Calibration curves for the positive Y-axis direction (without insulator)

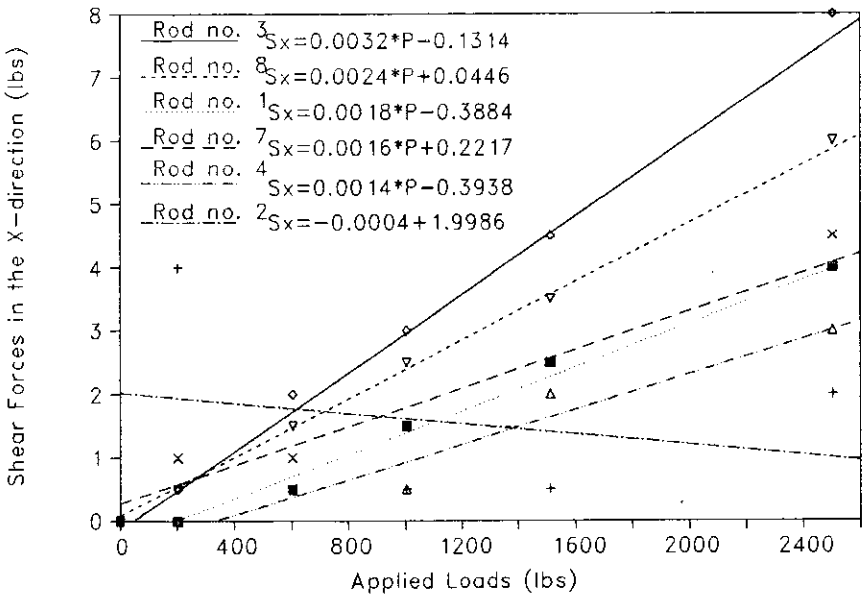

Figure C.22. Calibration curves for the positvie Y-axis direction (without insulator)

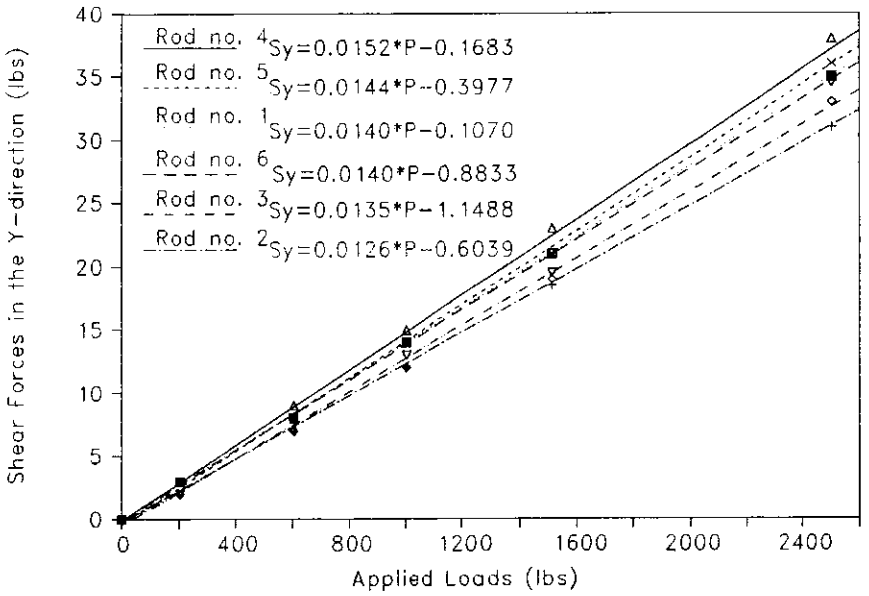

Figure C.23. Calibration curves for the positive Y-axis direction (without insulator)

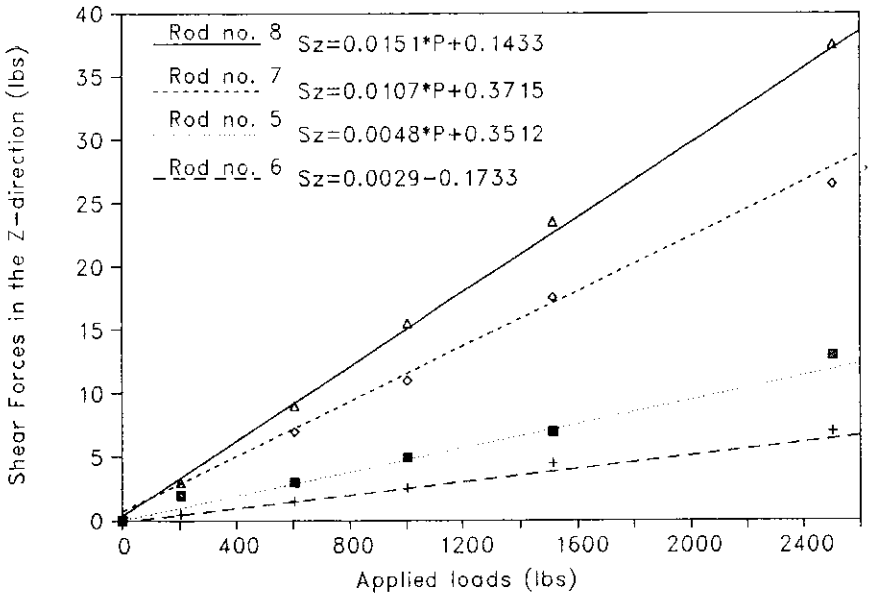

Figure C.24. Calibration curves for the positive Y-axis direction (without insulator)

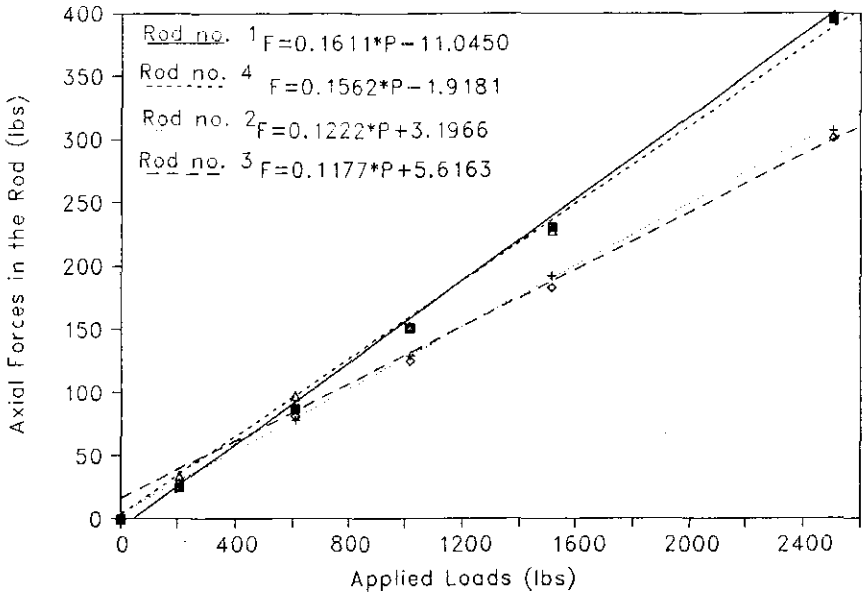

Figure C.25. Calibration curves for the negative Y-axis direction (without insulator)

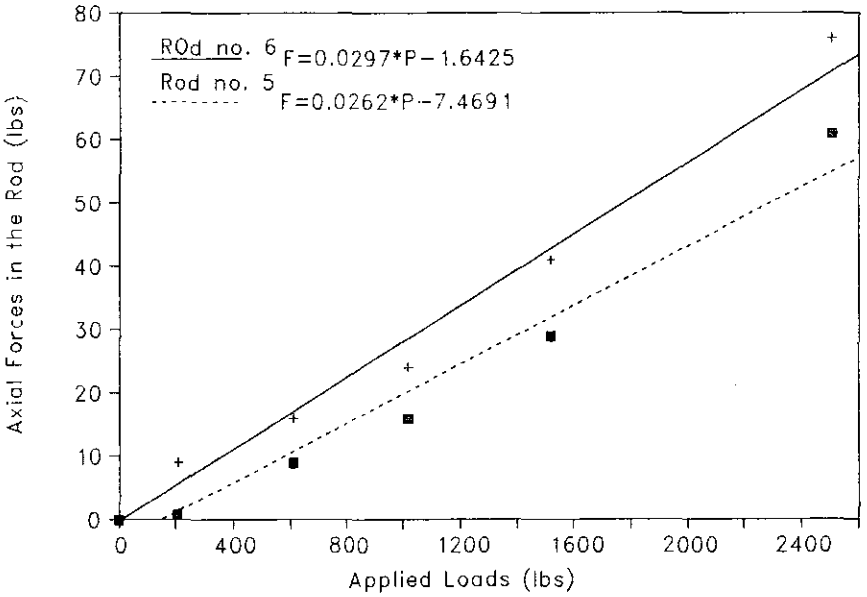

Figure C.26. Calibration curves for the negative Y-axis direction (without insulator)

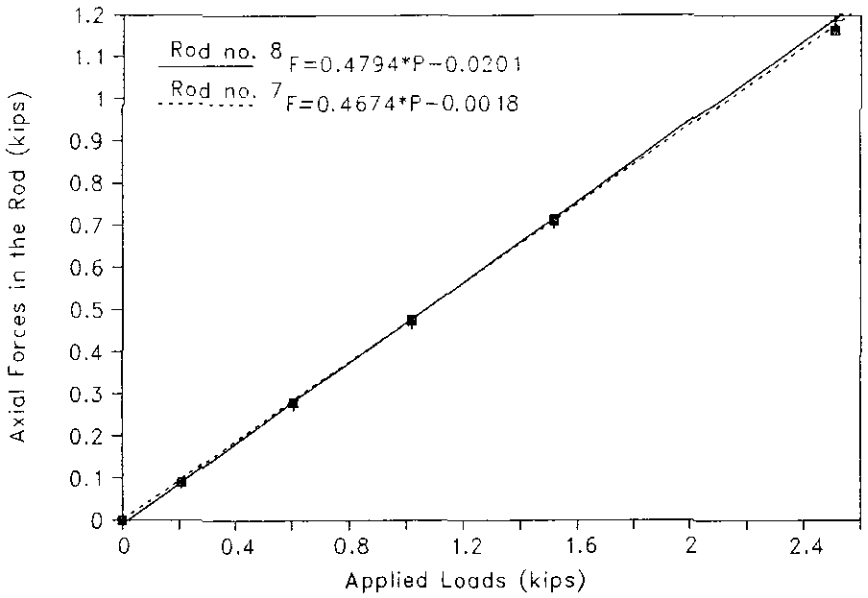

Figure C.27. Calibration curves for the negative Y-axis direction (without insulator)

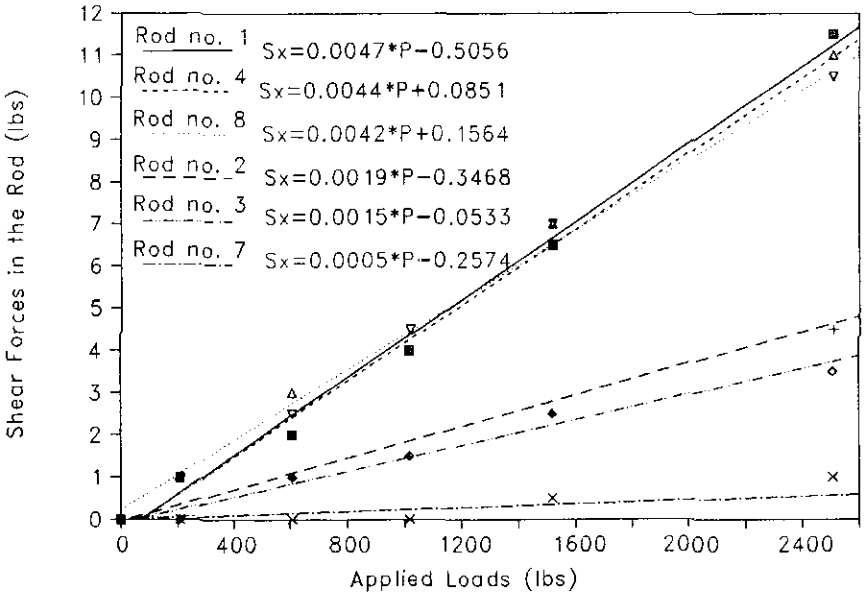

Figure D.28. Calibration curves for the negative Y-axis direction (without insulator)

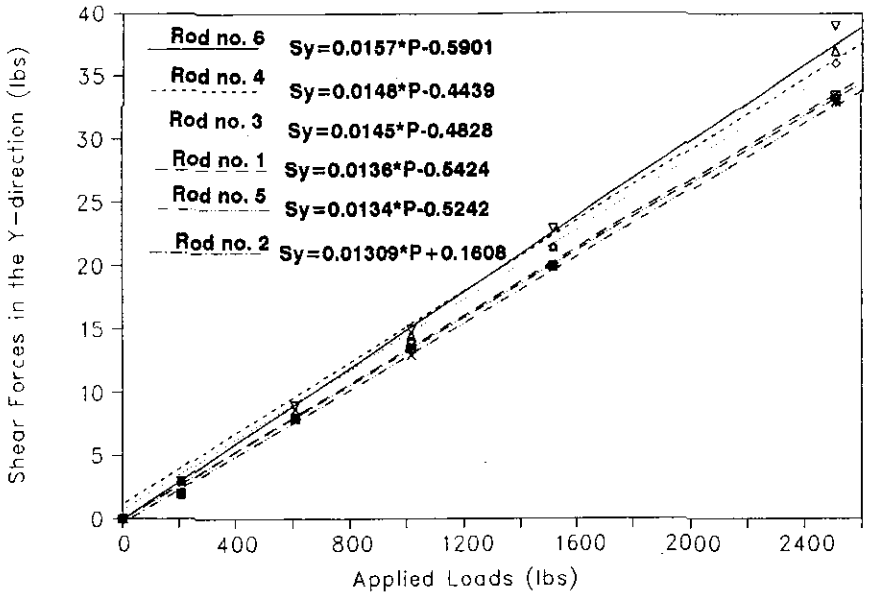

Figure C.29. Calibration curves for the negative Y-axis direction (without insulator)

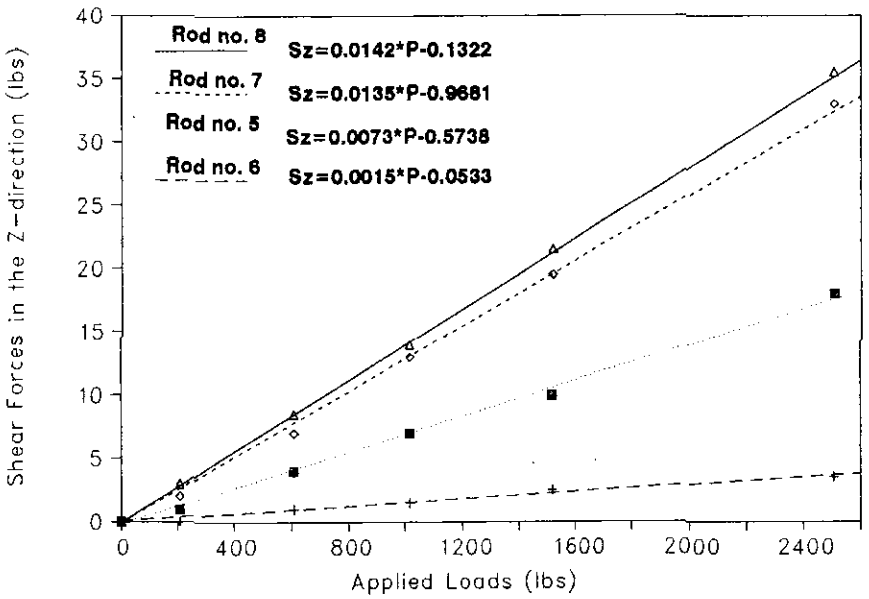

Figure C.30. Calibration curves for the negative Y-axis direction (without insulator)

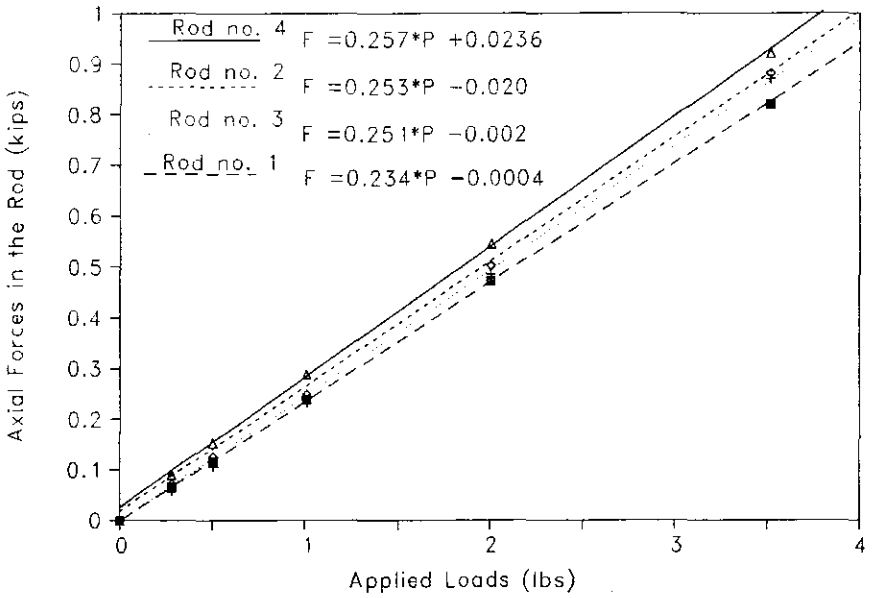

Figure C.31. Calibration curves for the neagative Z-axis direction (without insulator)

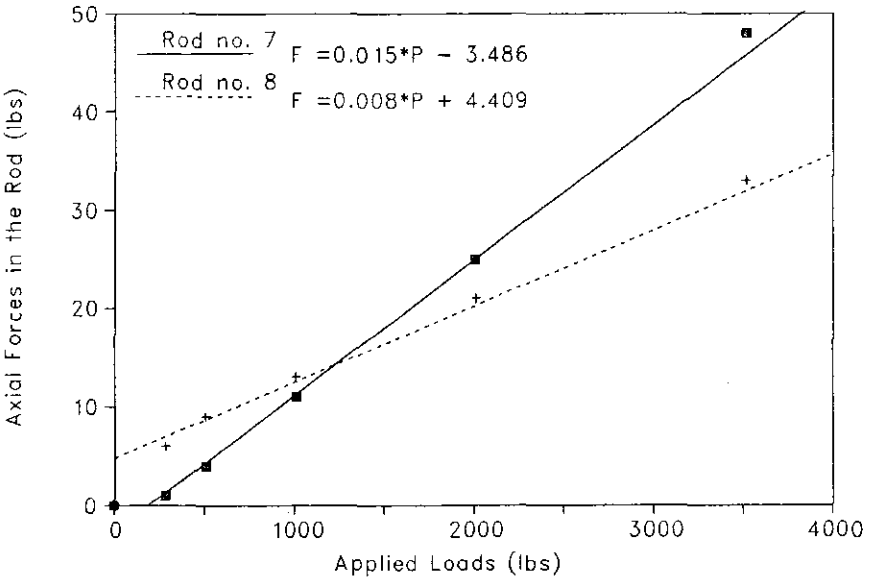

Figure C.33. Calibration curves for the negative Z-axis direction (without insulator)

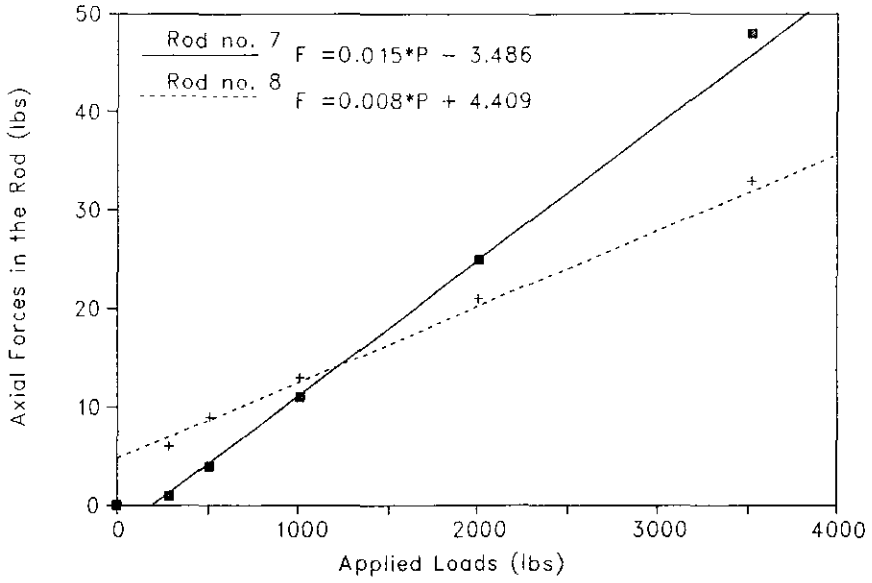

Figure C.33. Calibration curves for the negative Z-axis direction (without insulator)

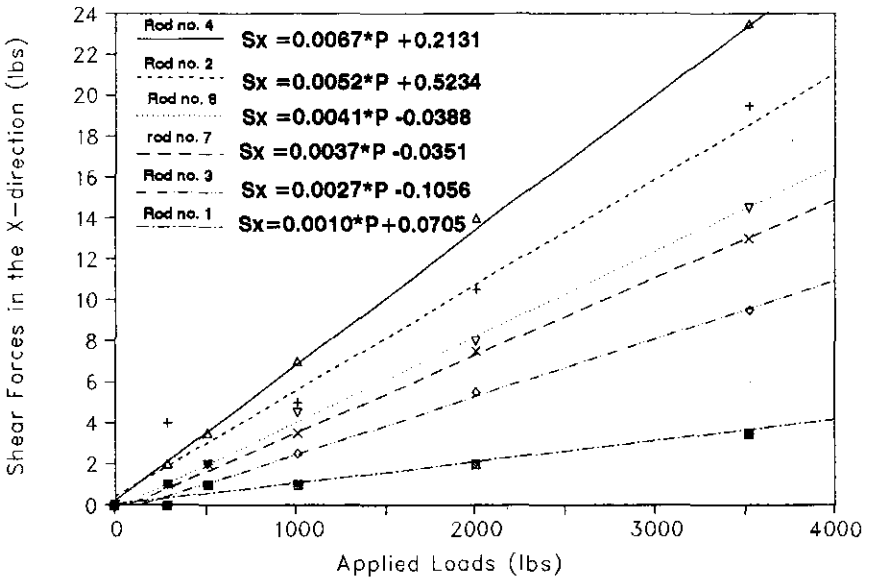

Figure C.34. Calibration curves for the negative Z-axis direction (without insulator)

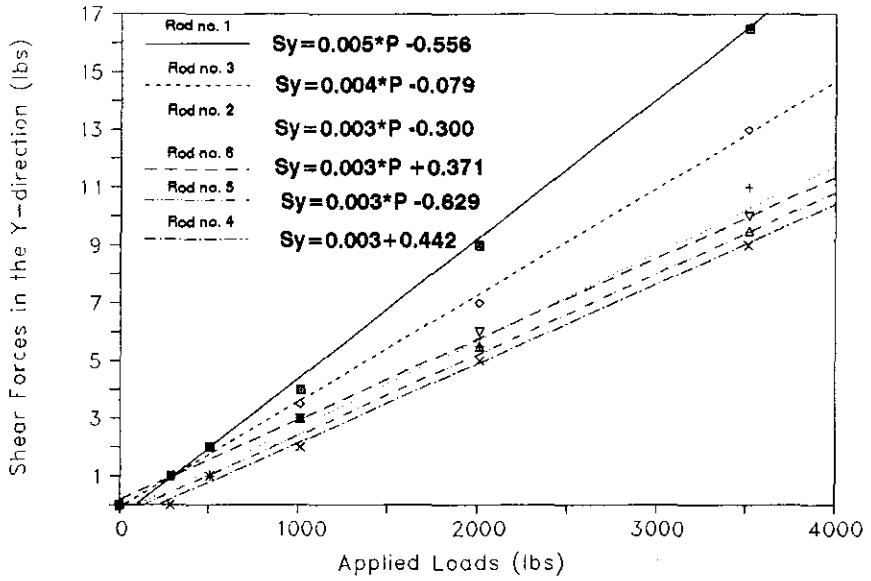

Figure C.35. Calibration curves for the negative Z-axis direction (without insulator)

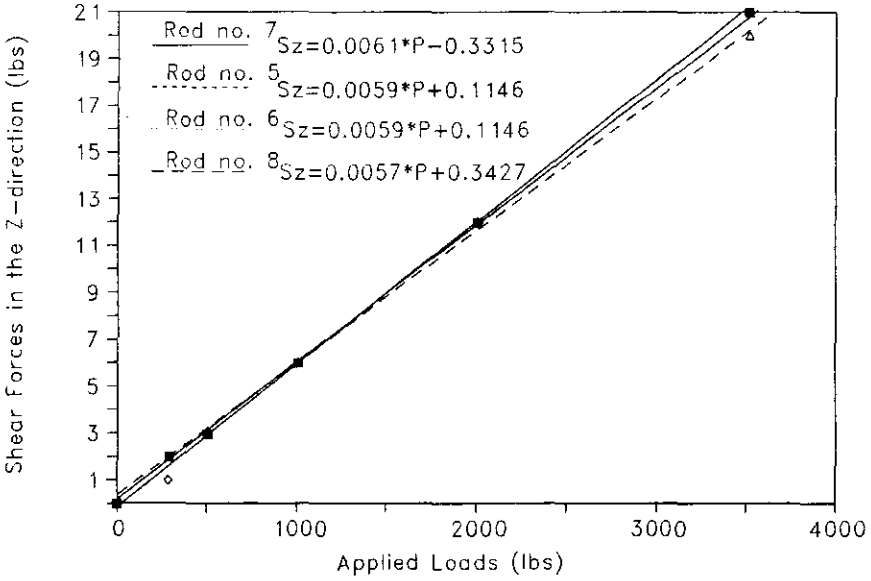

Figure D.36. Calibration curves for the negative Z-axis direction (without insulator)

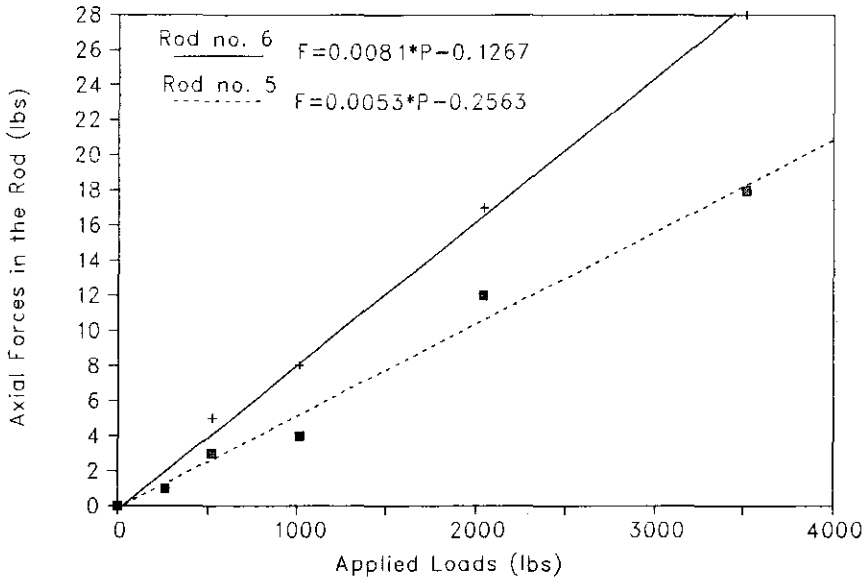

Figure C.37. Calibration curves for the positive Z-axis direction (without insulator)

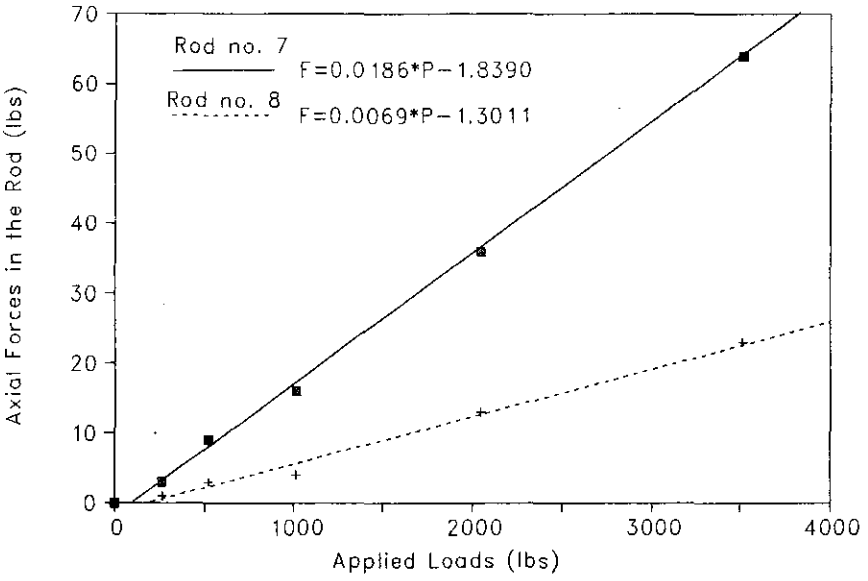

Figure C.38. Calibration curves for the positive Z-axis direction (without insulator)

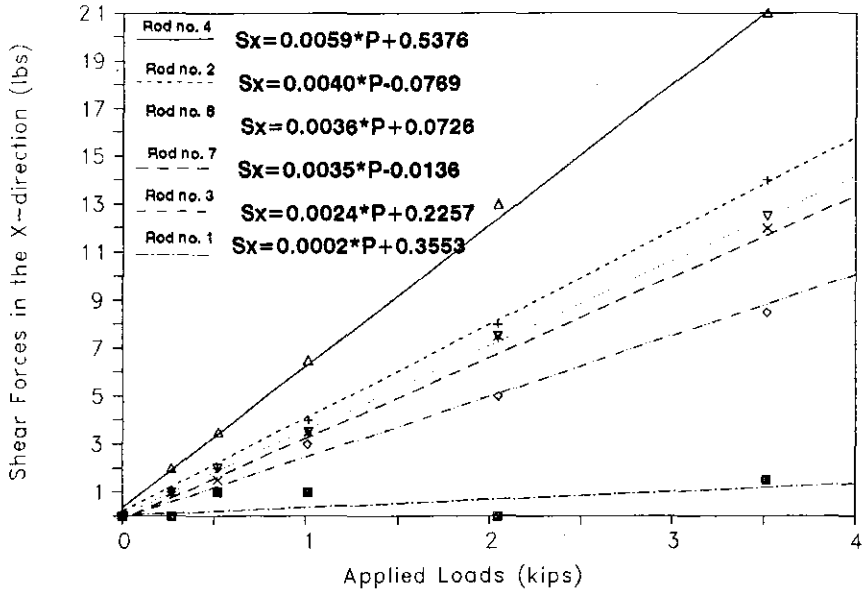

Figure C.39. Calibration curves for the the positive Z-axis direction (without insulator)

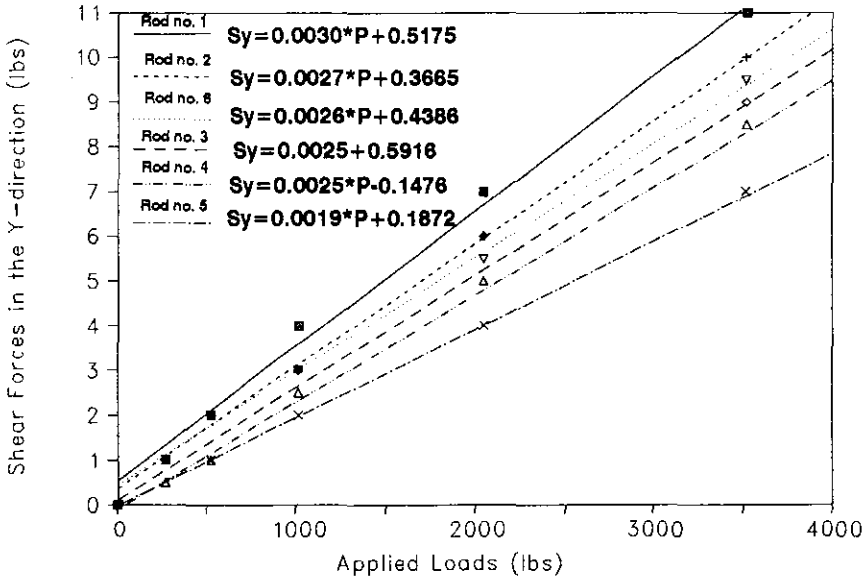

Figure C.40. Calibration curves for the positive Z-axis direction (without insulator)

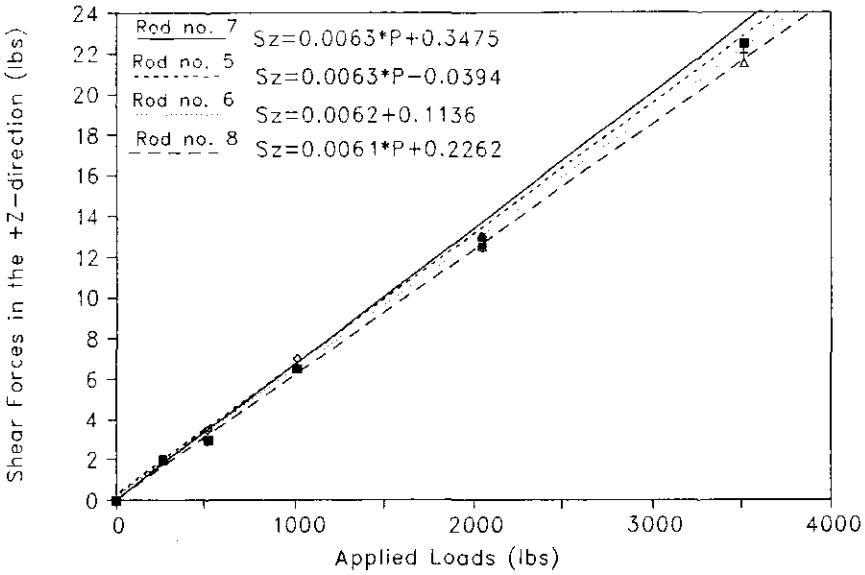

Figure C.41. Calibration curves for the positive Z-axis direction (without insulator)

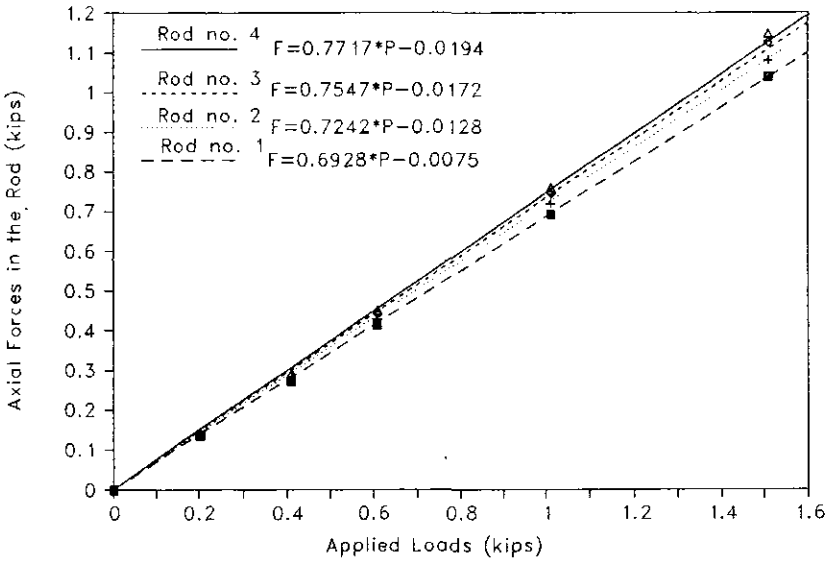

Figure C.42. Calibration curves for the positive X-axis direction (with insulator)

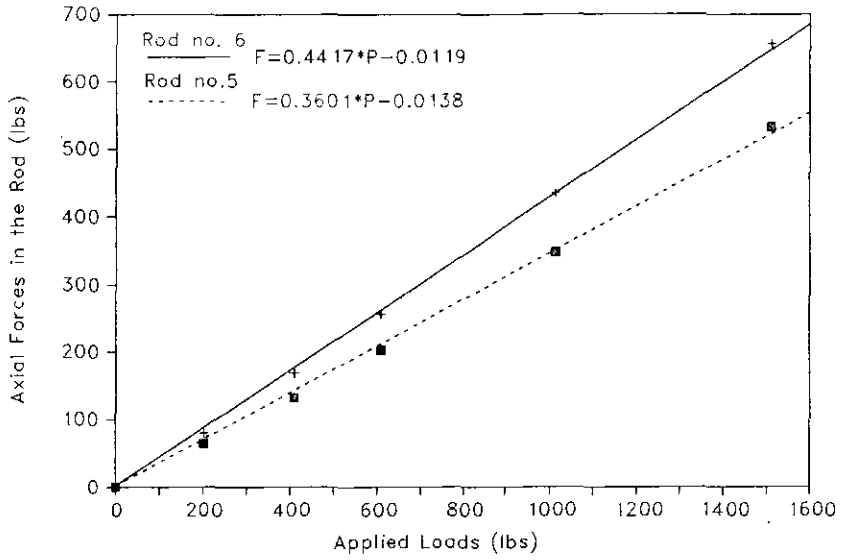

Figure C.43. Calibration curves for the positive X-axis direction (with insulator)

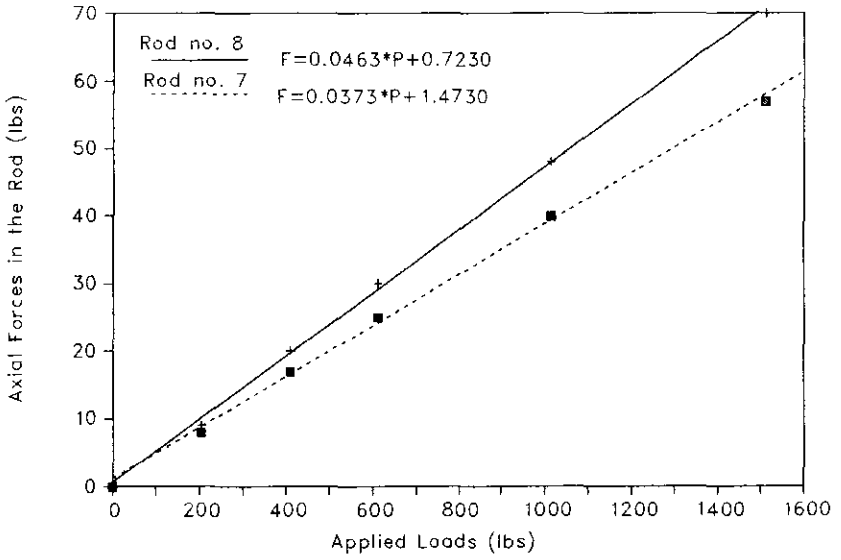

Figure C.44. Calibration curves for the positive X-axis direction (with insulator)

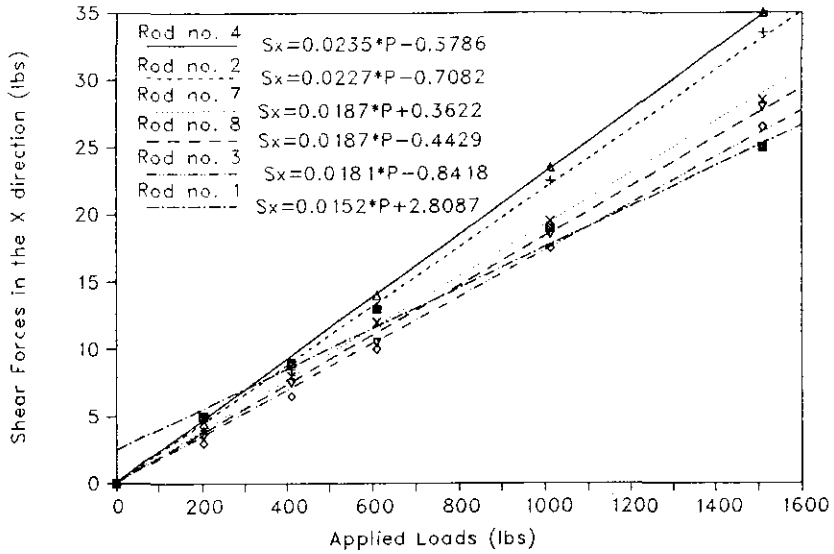

Figure C.45. Calibration curves for the positive X-axis direction (with insulator)

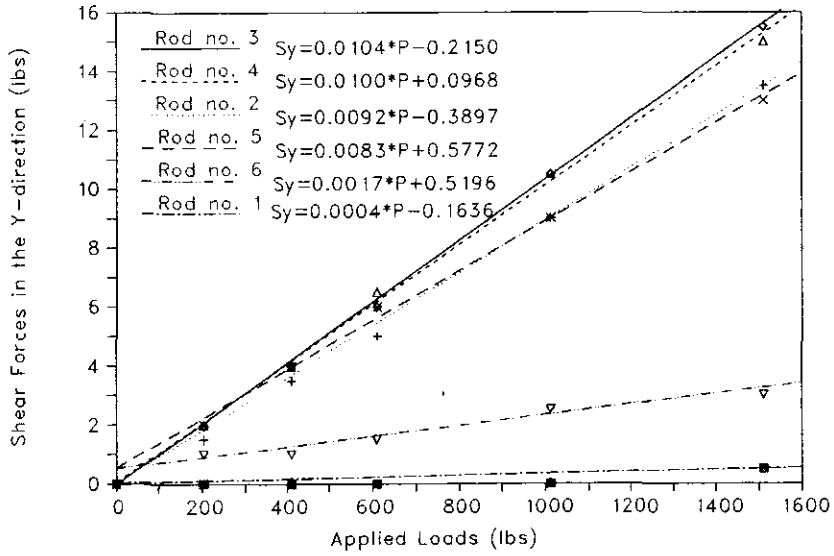

Figure C.46. Calibration curves for the positive X-axis direction (with insulator)

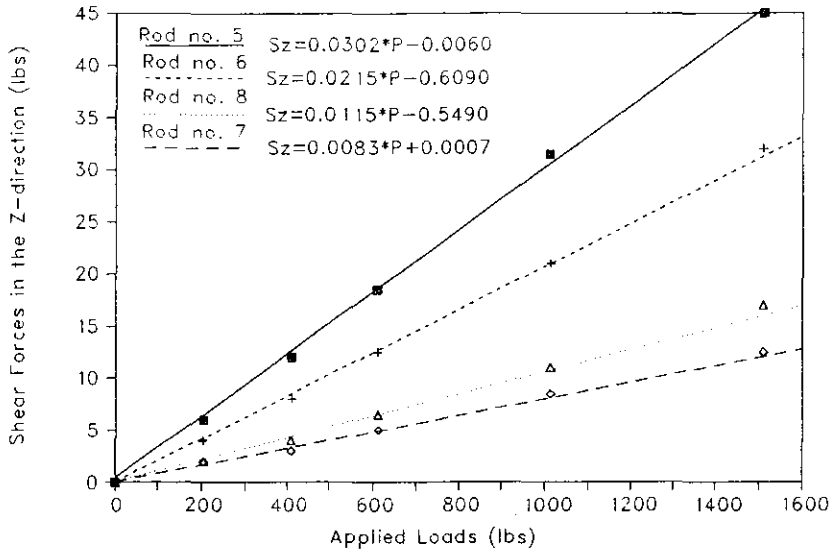

Figure C.47. Calibration curves for the positive X-axis direction (with insulator)

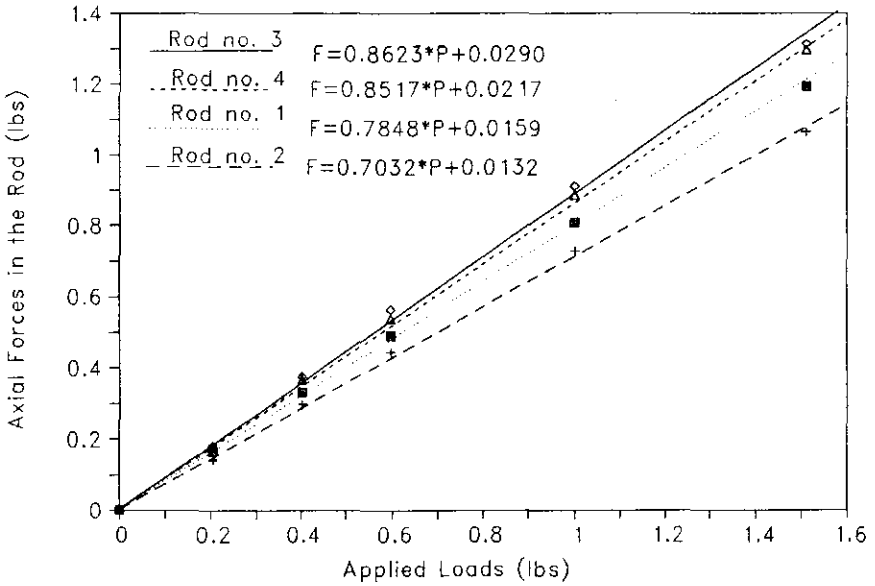

Figure C.48. Calibration curves for the negative X-axis direction (with insulator)

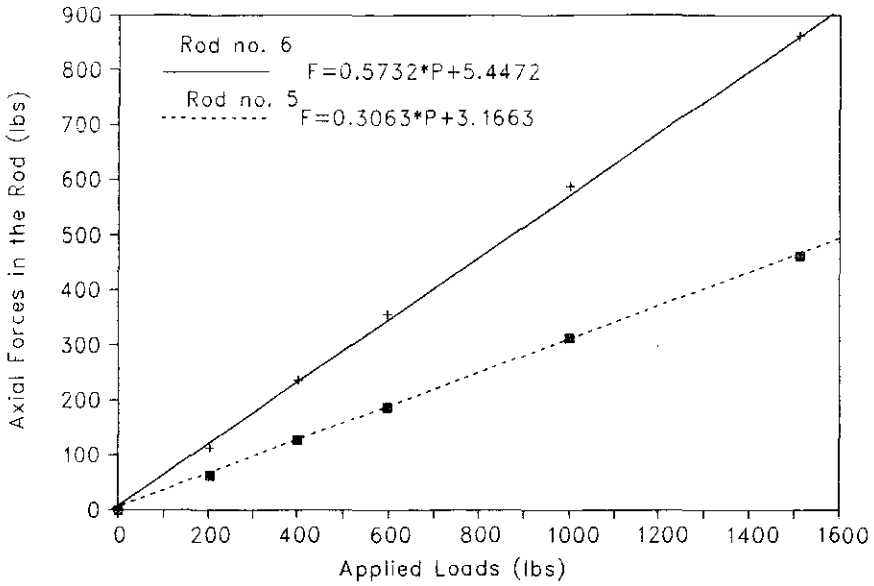

Figure C.49. Calibration curves for the negative X-axis direction (with insulator)

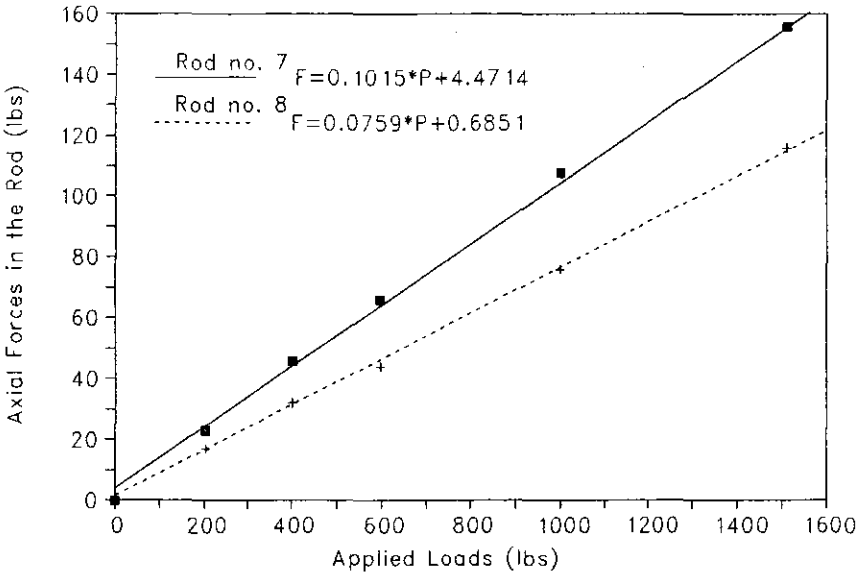

Figure C.50. Calibration curves for the negative X-axis direction (with insulator)

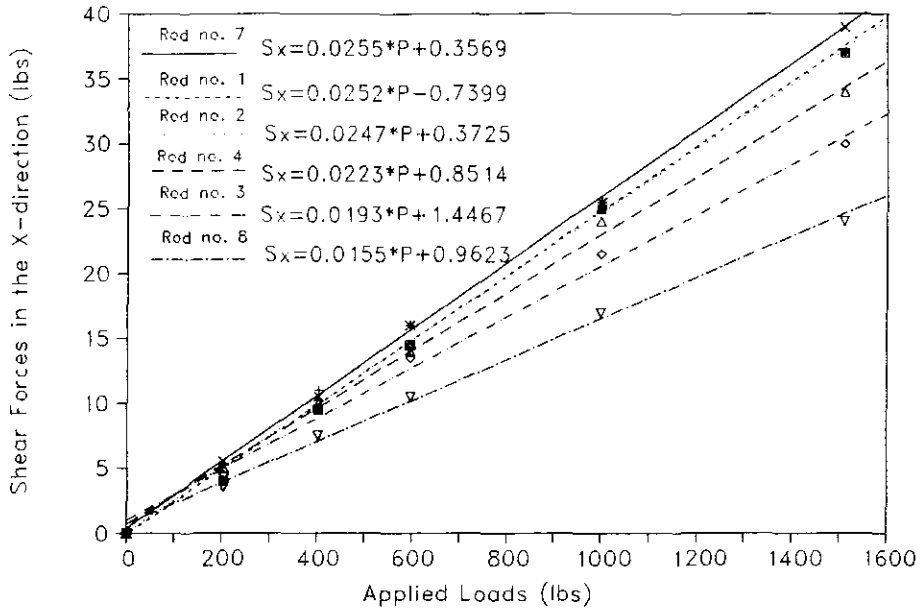

Figure C.51. Calibration curves for the negative X-axis direction (with insulator)

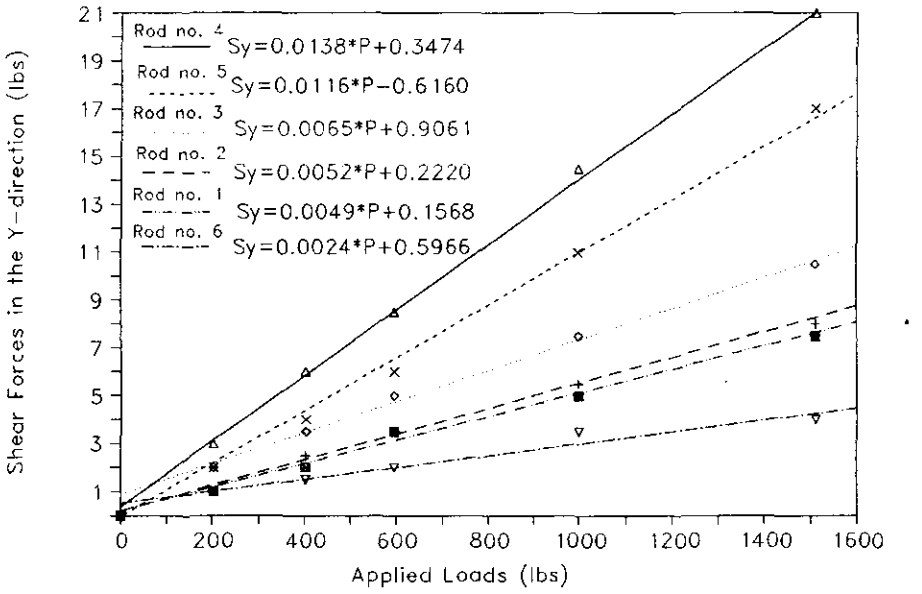

Figure C.52. Calibration curves for the negative X-axis direction (with insulator)

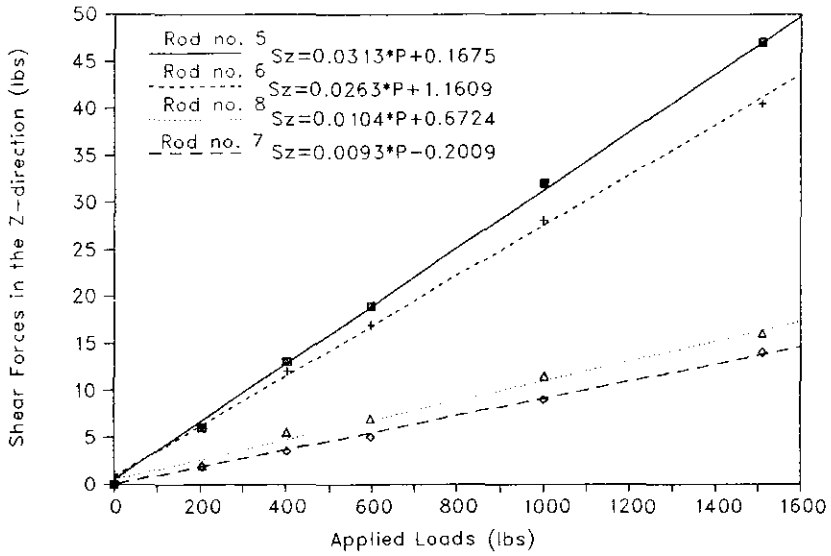

Figure C.53. Calibration curves for the negative X-axis direction (with insulator)

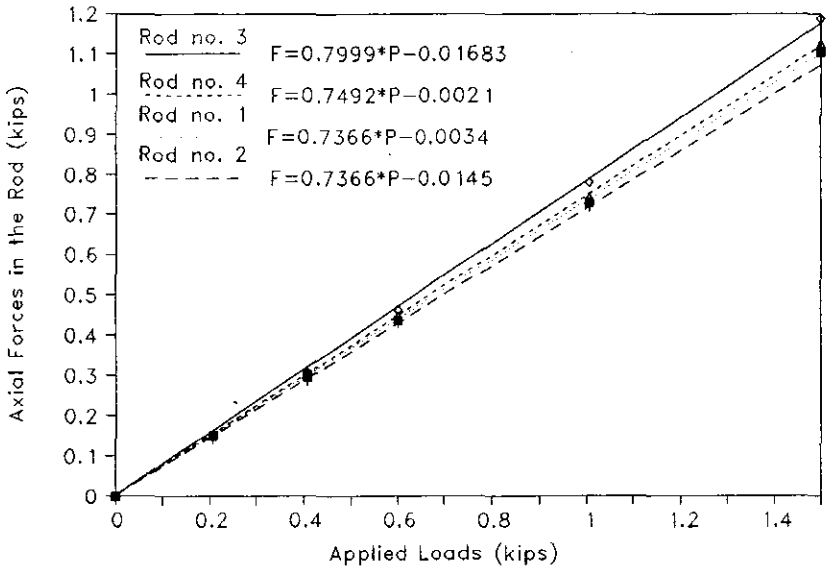

Figure C.54. Calibration curves for the positive Y-axis direction (with insulator)

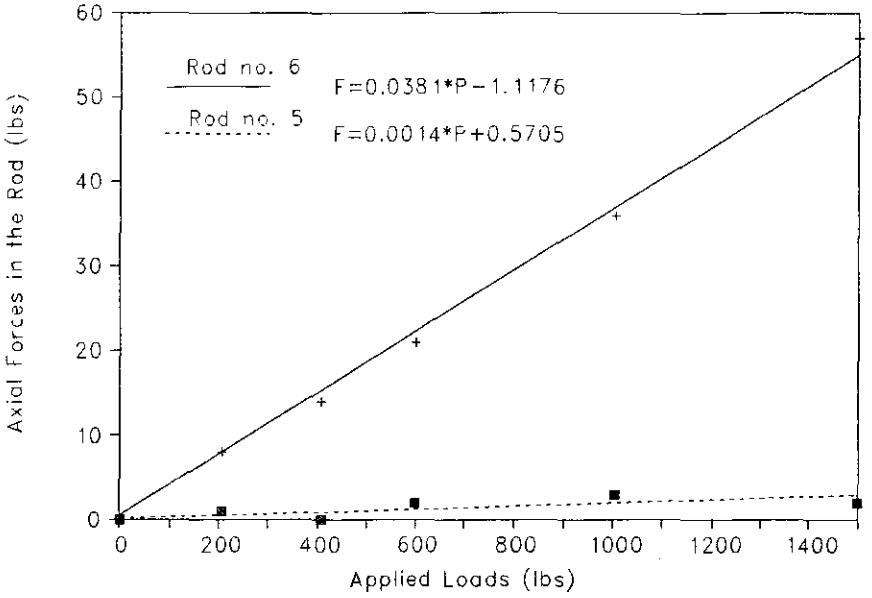

Figure C.55. Calibration curves for the positive Y-axis direction (with insulator)

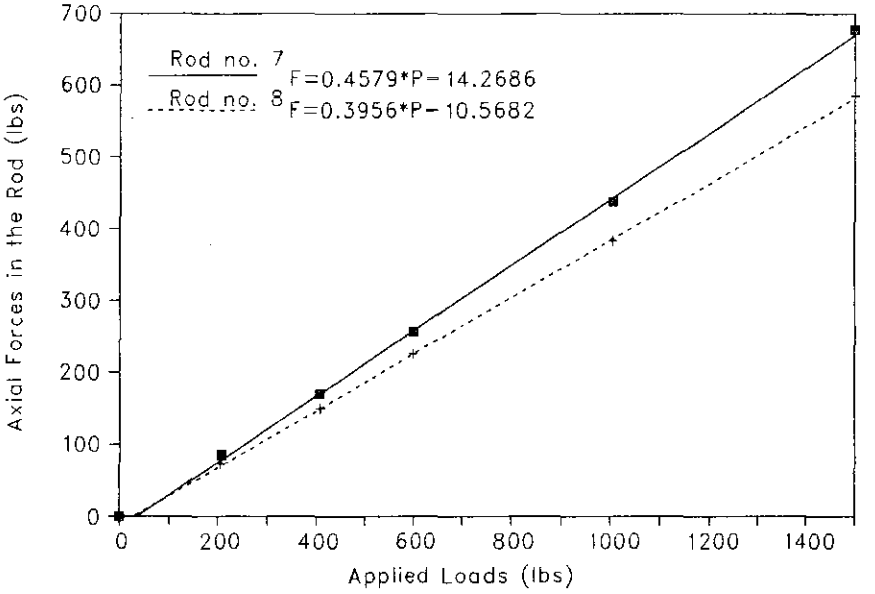

Figure C.56. Calibration curves for the positive Y-axis direction (with insulator)

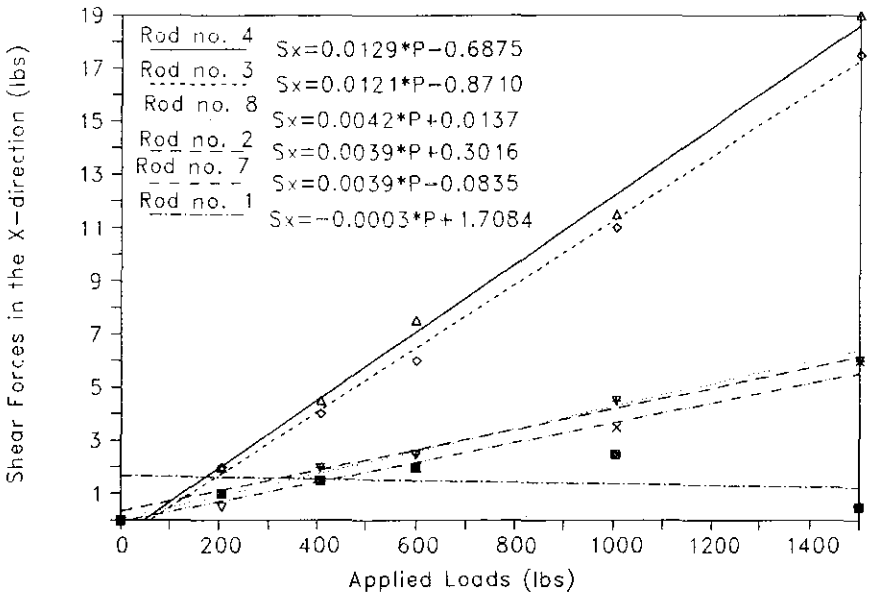

Figure C.57. Calibration curves for the positive Y-axis direction (with insulator)

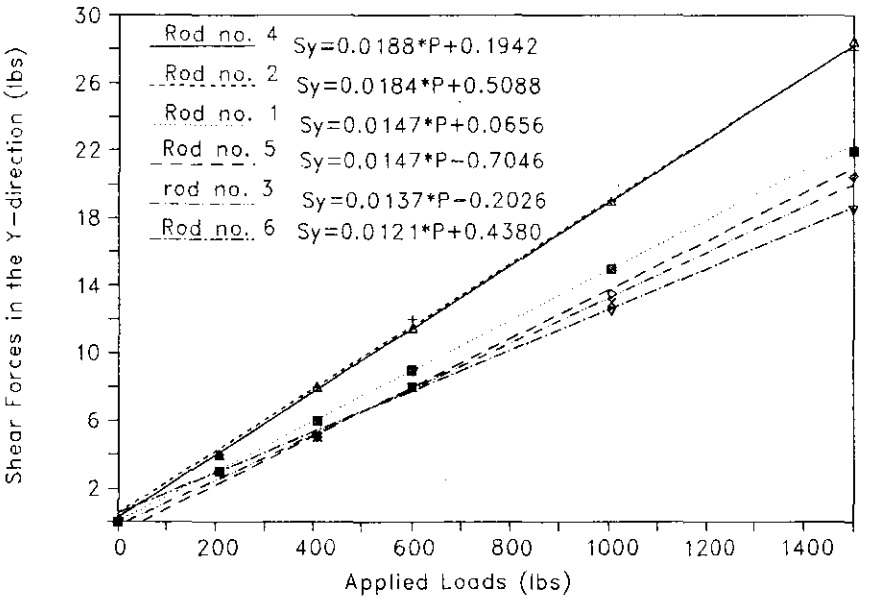

Figure C.58. Calibration curves for the positive Y-axis direction (with insulator)

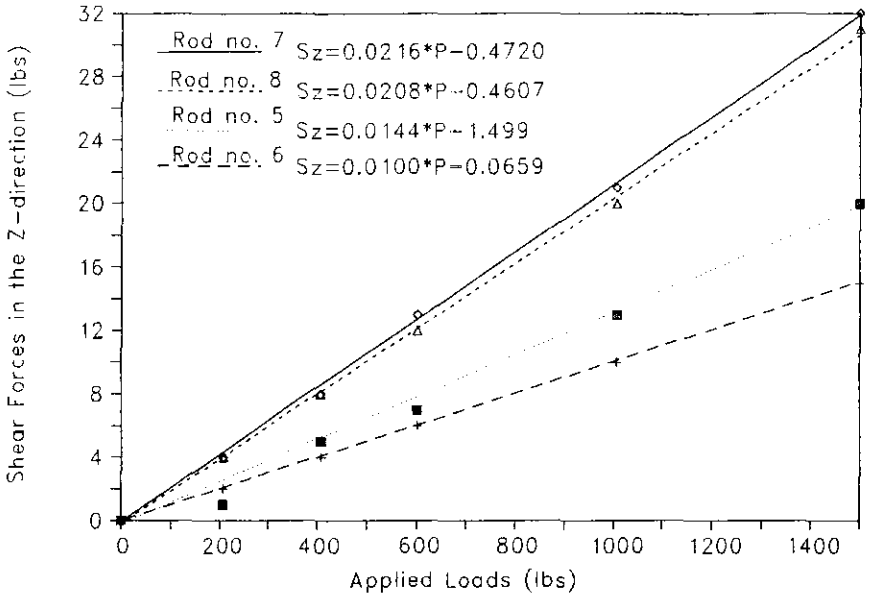

Figure C.59. Calibration curves for the positive Y-axis direction (with insulator)

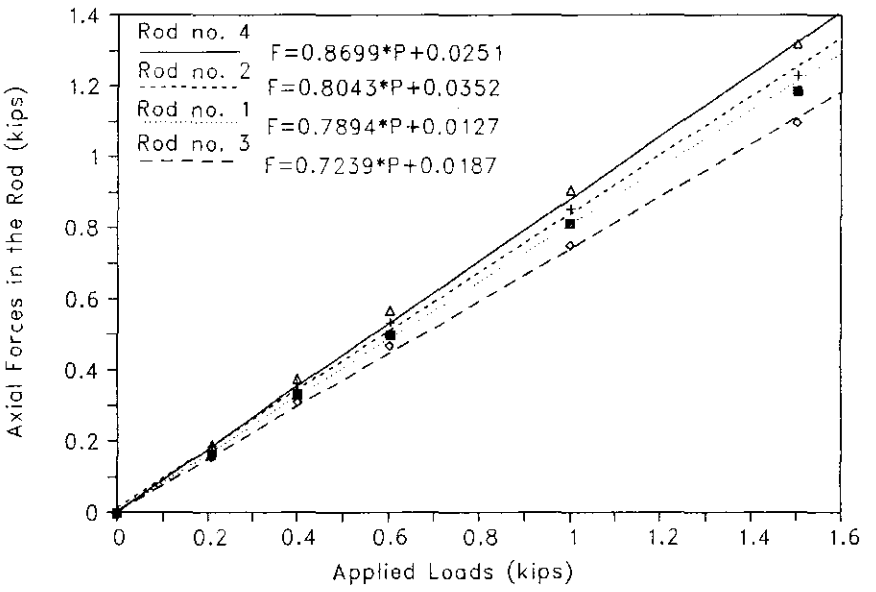

Figure C.60. Calibration curves for the negative Y-axis direction (with insulator)

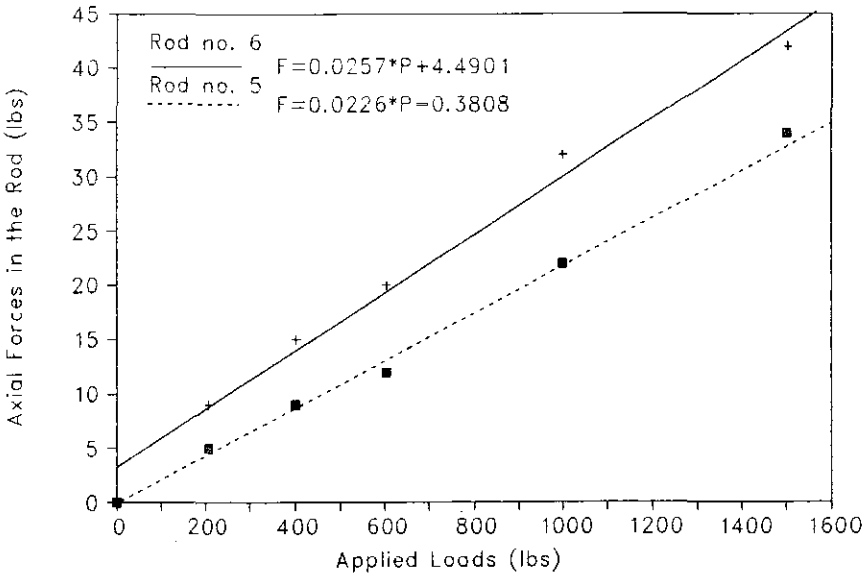

Figure C.61. Calibration curves for the negative Y-axis direction (with insulator)

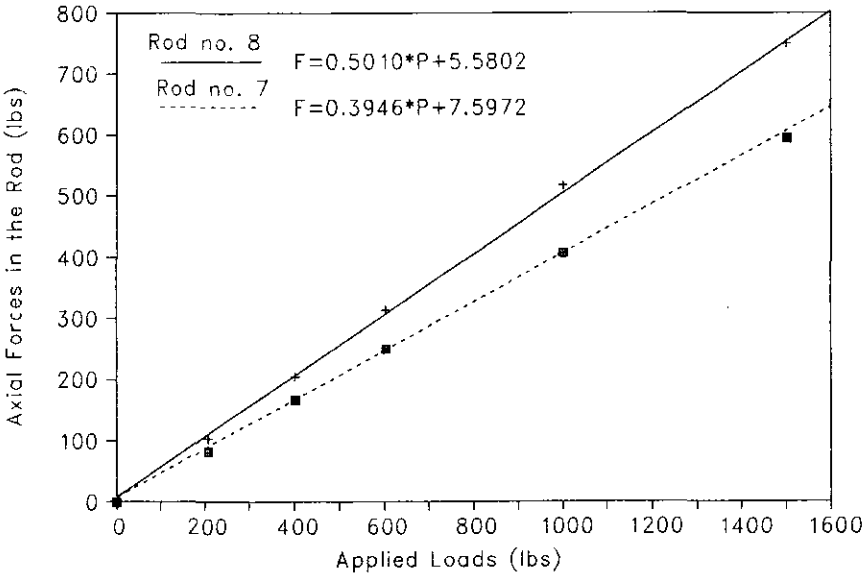

Figure D.62. Calibration curves for the negative Y-axis direction (with insulator)

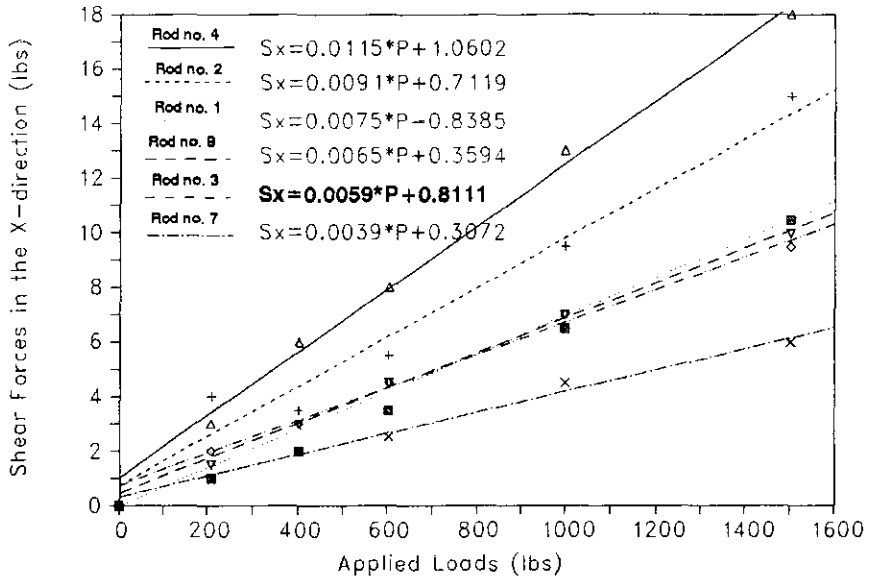

Figure C.63. Calibration curves for the negative Y-axis direction (with insulator)

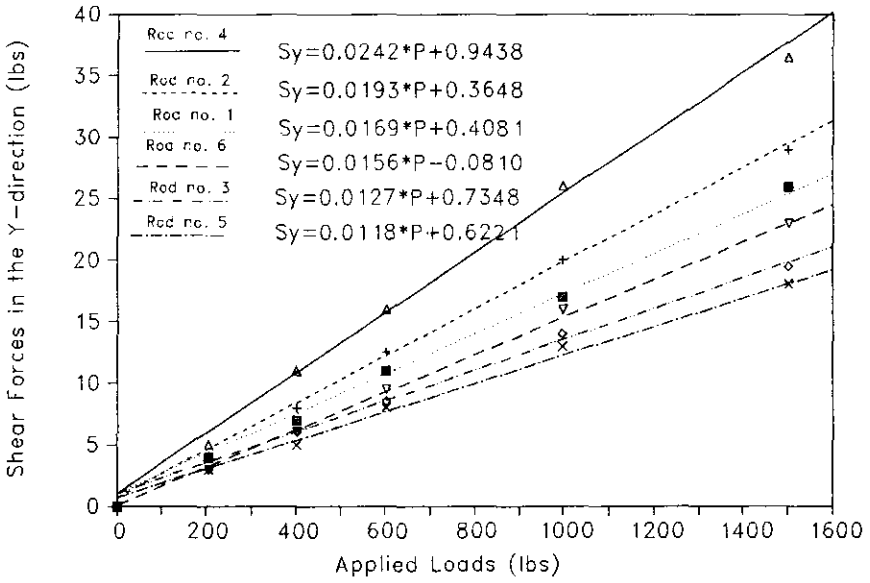

Figure C.64. Calibration curves for the negative Y-axis direction (with insulator)

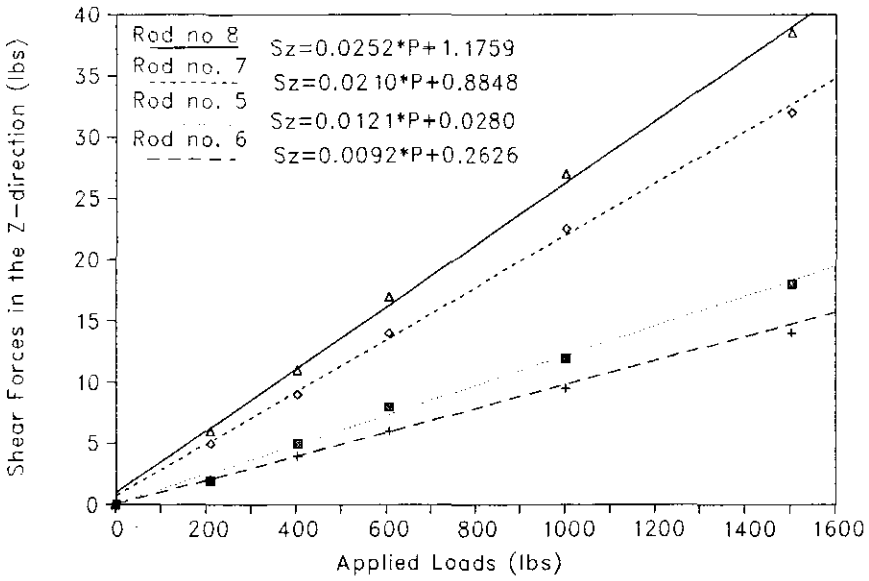

Figure C.65. Calibration curves for the negative Y-axis direction (with insulator)

APPENDIX D. RESULTS OF THE COMBINED LOADS TESTS

Table D.1. Comparison of loads measured by various methods in tests without insulator

Load / Approach	Px (lbs)	Py (lbs)	Pz (lbs)	Test
measurement	-527	0	530	1
$[A]_{8*3}$	-468(11.2%)	-6	582(9.8%)	
equilibrium	-491(6.8%)	-20	509(4.0%)	
measurement	-515	0	1039	2
$[A]_{8*3}$	-458(11.1%)	1	1085(4.4%)	
equilibrium	-476(7.6%)	-19	1021(1.7%)	
measurement	-505	0	2001	3
$[A]_{8*3}$	-462(8.5%)	16	2044(2.1%)	
equilibrium	-467(7.5%)	-29	2001 (0%)	
measurement	-500	0	3048	4
$[A]_{8*3}$	-484(3.2%)	16	3020(0.9%)	
equilibrium	-458(8.5%)	-12	3061(0.4%)	
measurement	-1038	0	577	5
$[A]_{8*3}$	-978(5.9%)	-29	633(9.7%)	
equilibrium	-1014(2.4%)	-35	551(4.5%)	
measurement	-2066	0	540	6
$[A]_{8*3}$	-2049(0.8%)	-43	629(16.5%)	
equilibrium	-2017(2.4%)	-27	533(1.4%)	

Table D.1. (continued)

Load / Approach	Px (lbs)	Py (lbs)	Pz (lbs)	Test
measurement	0	-480	507	7
$[A]_{8*3}$	3	-425(11.5%)	562(10.8%)	
equilibrium	-2	-474(1.3%)	497(2.0%)	
measurement	0	-458	1071	8
$[A]_{8*3}$	-6	-395(13.8%)	1123(4.9%)	
equilibrium	-2	-454(0.9%)	1067(0.4%)	
measurement	0	-444	2014	9
$[A]_{8*3}$	-19	-382(14.0%)	2066(2.6%)	
equilibrium	0	-451(1.6%)	2029(0.7%)	
measurement	0	-437	3057	10
$[A]_{8*3}$	-48	-388(11.2%)	3039(0.6%)	
equilibrium	-2	-456(4.2%)	3085(0.9%)	
measurement	0	-902	532	11
$[A]_{8*3}$	12	-849(5.9%)	592(11.3%)	
equilibrium	4	-900(0.2%)	529(0.7%)	
measurement	0	-1955	601	12
$[A]_{8*3}$	15	-1905(2.6%)	673(12.0%)	
equilibrium	8	-1983(1.4%)	612(1.7%)	

Table D.1. (continued)

Load / Approach	Px (lbs)	Py (lbs)	Pz (lbs)	Test
measurement	477	0	527	13
$[A]_{8*3}$	424(11.1%)	53	558(5.9%)	
equilibrium	458(4.0%)	15	504(4.4%)	
measurement	458	0	1031	14
$[A]_{8*3}$	397(13.3%)	49	1052(2.0%)	
equilibrium	439(4.1%)	6	1007(2.3%)	
measurement	447	0	20	15
$[A]_{8*3}$	389(13.0%)	36	2035(0.8%)	
equilibrium	439(1.8%)	-11	2010(0.4%)	
measurement	439	0	3037	16
$[A]_{8*3}$	374(14.6%)	10	2970(2.2%)	
equilibrium	444(1.0%)	-31	3039(0.1%)	
measurement	982	0	555	17
$[A]_{8*3}$	945(3.8%)	4	594(7.0%)	
equilibrium	998(1.6%)	11	557(0.4%)	
measurement	1993	0	517	18
$[A]_{8*3}$	1961(1.6%)	73	532(2.9%)	
equilibrium	2058(3.2%)	17	519(0.3%)	

Table D.1. (continued)

Load / Approach	Px (lbs)	Py (lbs)	Pz (lbs)	Test
measurement	0	533	530	19
$[A]_{8*3}$	1	498(6.6%)	578(9.0%)	
equilibrium	7	498(6.6%)	519(2.2%)	
measurement	0	512	1069	20
$[A]_{8*3}$	-3	475(7.2%)	1099(2.8%)	
equilibrium	9	470(8.2%)	1050(1.8%)	
measurement	0	495	2011	21
$[A]_{8*3}$	-4	467(15.7%)	2017(0.3%)	
equilibrium	12	453(8.6%)	1988(1.2%)	
measurement	0	487	3022	22
$[A]_{8*3}$	-18	442(9.2%)	2938(2.8%)	
equilibrium	17	436(10.6%)	2992(1.0%)	
measurement	0	1005	519	23
$[A]_{8*3}$	-6	972(3.3%)	587(13.1%)	
equilibrium	5	976(2.9%)	529(1.8%)	
measurement	0	1952	506	24
$[A]_{8*3}$	-14	1930(1.1%)	584(15.4%)	
equilibrium	25	1950(0.1%)	533(5.2%)	

Table D.2. Comparison of loads measured by various methods in tests with insulator

Load / Approach	Px (lbs)	Py (lbs)	Pz (lbs)	Test
measurement	-542	0	580	1
$[A]_{8*3}$	-578(6.6%)	-4	653(21.6%)	
equilibrium	-543(0.2%)	-12	607(4.7%)	
measurement	-556	0	1011	2
$[A]_{8*3}$	-588(5.8%)	-9	1072(6.0%)	
equilibrium	-547(1.6%)	-23	1036(2.5%)	
measurement	-508	0	2032	3
$[A]_{8*3}$	-659(29.7%)	-4	2107(3.7%)	
equilibrium	-567(11.6%)	-44	2096(3.1%)	
measurement	-581	0	3116	4
$[A]_{8*3}$	-761(31.0%)	9	3185(2.2%)	
equilibrium	-640(10.2%)	-50	3200(2.7%)	
measurement	-1146	0	610	5
$[A]_{8*3}$	-1264(10.3%)	10	674(10.5%)	
equilibrium	-1189(3.8%)	14	653(7.0%)	
measurement	-1561	0	547	6
$[A]_{8*3}$	-1710(9.5%)	26	606(10.8%)	
equilibrium	-1611(3.2%)	37	534(2.4%)	

Table D.2. (continued)

Load / Approach	Px (lbs)	Py (lbs)	Pz (lbs)	Test
measurement	-557	-236	534	7
$[A]_{8*3}$	-555(0.4%)	-208(11.9%)	579(8.4%)	
equilibrium	-516(7.4%)	-214(9.3%)	530(0.8%)	
measurement	-580	-246	1057	8
$[A]_{8*3}$	-569(1.9%)	-220(10.6%)	1101(4.2%)	
equilibrium	-524(9.7%)	-248(0.8%)	1066(0.9%)	
measurement	-604	-256	2054	9
$[A]_{8*3}$	-611(1.2%)	-236(7.8%)	2088(1.7%)	
equilibrium	-539(10.8%)	-284(10.9%)	2073(0.9%)	
measurement	-616	-261	3050	10
$[A]_{8*3}$	-661(7.3%)	-239(8.4%)	3083(1.1%)	
equilibrium	-559(9.3%)	-316(21.1%)	3089(1.3%)	
measurement	-1009	-428	691	11
$[A]_{8*3}$	-982(2.7%)	-396(7.5%)	736(6.5%)	
equilibrium	-921(8.7%)	-391(8.6%)	700(1.3%)	
measurement	-1408	-598	558	12
$[A]_{8*3}$	-1427(1.3%)	-559(6.5%)	588(5.0%)	
equilibrium	-1341(4.8%)	-533(10.9%)	561(0.5%)	

Table D.2. (continued)

Load / Approach	Px (lbs)	Py (lbs)	Pz (lbs)	Test
measurement	-402	-402	555	13
$[A]_{8*3}$	-432(7.5%)	-363(9.7%)	641(15.5%)	
equilibrium	-393(2.2%)	-360(10.4%)	584(5.2%)	
measurement	-403	-403	1085	14
$[A]_{8*3}$	-454(12.7%)	-358(11.2%)	1158(6.7%)	
equilibrium	-395(2.0%)	-364(9.7%)	1114(2.7%)	
measurement	-428	-428	2017	15
$[A]_{8*3}$	-513(19.9%)	-345(19.4%)	2090(3.6%)	
equilibrium	-418(2.3%)	-368(14.0%)	2067(2.5%)	
measurement	-457	-457	3098	16
$[A]_{8*3}$	-580(26.9%)	-326(28.7%)	3158(1.9%)	
equilibrium	-443(3.1%)	-371(18.8%)	3160(2.0%)	
measurement	-712	-712	502	17
$[A]_{8*3}$	-727(2.1%)	-691(2.9%)	571(13.7%)	
equilibrium	-681(4.4%)	-662(7.0%)	524(4.4%)	
measurement	-1052	-1052	514	18
$[A]_{8*3}$	-1079(2.6%)	-1013(3.7%)	559(8.8%)	
equilibrium	-1027(2.4%)	-961(8.7%)	497(3.3%)	

Table D.2. (continued)

Load / Approach	Px (lbs)	Py (lbs)	Pz (lbs)	Test
measurement	-191	-462	606	19
$[A]_{8*3}$	-253(32.5%)	-501(8.4%)	666(9.9%)	
equilibrium	-222(1.1%)	-480(3.9%)	599(1.2%)	
measurement	-191	-460	1072	20
$[A]_{8*3}$	-262(37.2%)	-510(10.9%)	1138(6.2%)	
equilibrium	-213(11.5%)	-494(7.4%)	1079(0.7%)	
measurement	-192	-465	2136	21
$[A]_{8*3}$	-283(47.4%)	-547(17.6%)	2192(2.6%)	
equilibrium	-199(3.6%)	-535(15.1%)	2154(10.8%)	
measurement	-199	-480	3113	22
$[A]_{8*3}$	-313(57.3%)	-577(20.2%)	3167(1.7%)	
equilibrium	-191(4.0%)	-574(19.6%)	3149(1.2%)	
measurement	-375	-905	550	23
$[A]_{8*3}$	-471(25.6%)	-979(8.2%)	617(12.2%)	
equilibrium	-439(17.1%)	-927(2.4%)	540(1.8%)	
measurement	-608	-1467	534	24
$[A]_{8*3}$	-719(18.3%)	-1496(2.0%)	599(12.2%)	
equilibrium	-681(12.0 %)	-1416(3.5%)	513(3.9%)	

Table D.2. (continued)

Load / Approach	Px (lbs)	Py (lbs)	Pz (lbs)	Test
measurement	0	-571	540	25
$[A]_{8*3}$	-6	-557(2.5%)	706(3.1%)	
equilibrium	5	-506(11.4%)	622(15.2%)	
measurement	0	-583	1097	26
$[A]_{8*3}$	-14	-570(2.2%)	1204(9.8%)	
equilibrium	16	-527(9.6%)	1133(3.3%)	
measurement	0	-606	2031	27
$[A]_{8*3}$	-42	-598(1.3%)	2180(7.3%)	
equilibrium	20	-533(12.0%)	2126(4.7%)	
measurement	0	-621	3040	28
$[A]_{8*3}$	-74	-640(3.1%)	3112(2.4%)	
equilibrium	34	-582(6.3%)	3083(1.4%)	
measurement	0	-997	608	29
$[A]_{8*3}$	3	-1084(8.7%)	724(19.1%)	
equilibrium	7	-999(0.2%)	623(2.5%)	
measurement	0	-1547	563	30
$[A]_{8*3}$	-18	-1594(3.0%)	685(21.7%)	
equilibrium	19	-1484(4.1%)	565(0.4%)	

Table D.2. (continued)

Load / Approach	Px (lbs)	Py (lbs)	Pz (lbs)	Test
measurement	433	-433	1018	31
$[A]_{8*3}$	417(3.7%)	-485(12.0%)	1076(5.7%)	
equilibrium	409(5.5%)	-437(0.9%)	985(3.2%)	
measurement	470	-470	1994	32
$[A]_{8*3}$	399(15.1%)	-543(15.5%)	2041(2.4%)	
equilibrium	411(12.6%)	-463(1.5%)	1970(1.2%)	
measurement	491	-491	3047	33
$[A]_{8*3}$	395(19.6%)	-598(21.8%)	3078(1.0%)	
equilibrium	425(13.4%)	-483(1.6%)	3025(0.7%)	
measurement	1129	-1129	547	34
$[A]_{8*3}$	1189(5.3%)	-1155(2.3%)	584(6.8%)	
equilibrium	1123(0.5%)	-1097(2.8%)	423(22.7%)	
measurement	812	-812	520	35
$[A]_{8*3}$	883(8.7%)	-862(6.2%)	564(8.5%)	
equilibrium	833(2.6%)	-815(0.4%)	428(17.7%)	
measurement	421	-421	558	36
$[A]_{8*3}$	424(0.7%)	-468(11.2%)	632(13.3%)	
equilibrium	417(1.0%)	-434(3.1%)	520(6.8%)	

Table D.2. (continued)

Load / Approach	Px (lbs)	Py (lbs)	Pz (lbs)	Test
measurement	0	517	504	37
$[A]_{8*3}$	21	578(11.8%)	556(10.3%)	
equilibrium	10	518(0.2%)	510(1.2%)	
measurement	0	515	1056	38
$[A]_{8*3}$	10	601(16.7%)	1108(4.9%)	
equilibrium	-12	524(1.7%)	1074(1.7%)	
measurement	0	507	2029	39
$[A]_{8*3}$	1	644(27%)	2074(2.2%)	
equilibrium	-38	536(5.7%)	2063(1.7%)	
measurement	0	508	3030	40
$[A]_{8*3}$	4	691(36%)	3068(1.3%)	
equilibrium	-56	552(8.7%)	2990(1.3%)	
measurement	0	1028	553	41
$[A]_{8*3}$	57	1137(10.6%)	622(12.5%)	
equilibrium	38	1041(1.3%)	536(3.1%)	
measurement	0	1578	570	42
$[A]_{8*3}$	-12	1656(4.9%)	619(8.6%)	
equilibrium	-23	1549(1.8%)	617(8.2%)	

Table D.2. (continued)

Load / Approach	Px (lbs)	Py (lbs)	Pz (lbs)	Test
measurement	403	403	506	43
$[A]_{8*3}$	400(0.7%)	407(1.0%)	566(11.9%)	
equilibrium	358(11.2%)	377(6.5%)	507(0.2%)	
measurement	416	416	1130	44
$[A]_{8*3}$	398(4.3%)	435(4.6%)	1180(4.4%)	
equilibrium	328(21.2%)	411(1.2%)	1136(0.5%)	
measurement	419	419	2077	45
$[A]_{8*3}$	416(0.7%)	474(13.1%)	2120(2.1%)	
equilibrium	324(22.7%)	458(9.3%)	2098(1.0%)	
measurement	416	416	3043	46
$[A]_{8*3}$	447(7.5%)	506(21.6%)	3091(1.6%)	
equilibrium	319(23.3%)	504(21.2%)	3091(1.6%)	
measurement	794	794	590	47
$[A]_{8*3}$	816(2.8%)	792(0.3%)	703(19.2%)	
equilibrium	754(5.0%)	752(5.3%)	648(9.8%)	
measurement	1107	1107	598	48
$[A]_{8*3}$	1231(11.2%)	1109(0.2%)	738(23.4%)	
equilibrium	1145(3.4%)	1059(4.3%)	675(12.9%)	

Table D.2. (continued)

Load / Approach	Px (lbs)	Py (lbs)	Pz (lbs)	Test
measurement	558	0	552	49
$[A]_{8*3}$	628(12.5%)	25	578(4.7%)	
equilibrium	589(5.6%)	23	491(11.0%)	
measurement	565	0	1006	50
$[A]_{8*3}$	639(13.1%)	46	1074(6.8%)	
equilibrium	596(5.5%)	54	997(0.9%)	
measurement	576	0	2007	51
$[A]_{8*3}$	677(17.5%)	59	2086(3.9%)	
equilibrium	627(8.9%)	101	2030(1.1%)	
measurement	593	0	3057	52
$[A]_{8*3}$	723(21.9%)	52	3101(1.4%)	
equilibrium	662(11.6%)	125	3068(0.4%)	
measurement	1076	0	659	53
$[A]_{8*3}$	1166(8.4%)	-41	752(14.1%)	
equilibrium	1102(2.4%)	-64	653(0.9%)	
measurement	1547	0	626	54
$[A]_{8*3}$	1654(6.9%)	-23	701(12.0%)	
equilibrium	1557(0.6%)	-20	570(8.9%)	

Table D.2. (continued)

Load / Approach	Px (lbs)	Py (lbs)	Pz (lbs)	Test
measurement	-391	391	633	55
$[A]_{8*3}$	-429(9.7%)	393(0.5%)	690(9.0%)	
equilibrium	-409(4.6%)	351(10.2%)	665(5.1%)	
measurement	-404	404	1077	56
$[A]_{8*3}$	-452(11.9%)	392(3.0%)	1119(3.9%)	
equilibrium	-432(6.9%)	341(15.6%)	1094(1.6%)	
measurement	-430	430	2022	57
$[A]_{8*3}$	-499(16.0%)	407(5.3%)	2046(1.2%)	
equilibrium	-485(12.8%)	333(22.6%)	2041(0.9%)	
measurement	-445	445	3017	58
$[A]_{8*3}$	-536(20.4%)	438(1.6%)	3016(0.03%)	
equilibrium	-528(18.7%)	332(25.4%)	3035(0.6%)	
measurement	-779	779	512	59
$[A]_{8*3}$	-814(4.5%)	787(1.0%)	563(10.0%)	
equilibrium	-771(1.0%)	733(5.9%)	552(7.8%)	
measurement	-1157	1157	618	60
$[A]_{8*3}$	-1186(2.5%)	1186(2.5%)	652(5.5%)	
equilibrium	-1128(2.5%)	1103(4.7%)	668(8.1%)	